INTERSTITIAL-IMPURITY TRAPPING IN Al-Fe AND Al-Zn

BY

KENNETH LOWELL HULTMAN

B.S., California Institute of Technology, 1970
M.S., University of Illinois, 1972

THESIS

Submitted in partial fulfillment of the requirements
for the degree of Doctor of Philosophy in Physics
in the Graduate College of the
University of Illinois at Urbana-Champaign, 1979

Urbana, Illinois

DISCLAIMER

INTERSTITIAL-IMPURITY TRAPPING IN Al-Fe AND Al-Zn

BY

KENNETH LOWELL HULTMAN

B.S., California Institute of Technology, 1970
M.S., University of Illinois, 1972

THESIS

Submitted in partial fulfillment of the requirements
for the degree of Doctor of Philosophy in Physics
in the Graduate College of the
University of Illinois at Urbana-Champaign, 1979

Urbana, Illinois

THIS PAGE

WAS INTENTIONALLY

LEFT BLANK

INTERSTITIAL-IMPURITY TRAPPING IN Al-Fe AND Al-Zn

Kenneth Lowell Hultman, Ph.D.
Department of Physics
University of Illinois at Urbana-Champaign, 1979

Ultrasonic attenuation and velocity measurements were made as a function of polarization, temperature, frequency and annealing before and after electron irradiation near 65K of Al-Fe and Al-Zn dilute alloys. Multiple relaxation processes were observed in both alloys. In the case of Al-Zn, the simultaneous annealing near 130K of resistivity, diaelastic modulus changes, and a paraelastic relaxation peak in C' allows for a characterization of the individual defects. The results provide strong evidence that below 130K, the <100>-mixed dumbbell is the predominant interstitial trapping configuration. The temperature dependence of the relaxation peak near 4.9K is not that expected for a thermally activated process, but provides instead evidence for defect tunneling. A second trapping configuration present in low concentration anneals out near 100K, and probably arises from <111>-mixed defects.

In Al-Fe, the observation of the diaelastic effect and a peak in the C' mode not previously seen in earlier internal friction measurements, together with an identification of this peak with the major defect species resolves the apparent contradiction between the internal friction and channelling symmetry evidence. This also allows for an interpretation in terms of a <100>-mixed dumbbell which is consistent with previous theory and channelling and Mössbauer measurements.

The results for Al-Fe differ greatly from those obtained earlier for Al-Mn, suggesting that current theories based only on size differences require extension.

ACKNOWLEDGEMENTS

The author sincerely thanks his advisor, Professor A. V. Granato, for his encouragement, advice, and guidance.

He also thanks Drs. G. G. Setser and D. L. Johnson for initial guidance in the techniques that they developed. He thanks Professor Jon T. Holder for advice and assistance in interpreting the results.

He expresses his appreciation to Mr. H. Wong and Mr. P. Wallace for their many long hours of help in preparing samples and operating the equipment.

The support of the United States Department of Energy under contract EY-76-C-02-1198 is gratefully acknowledged.

TABLE OF CONTENTS

LIST OF FIGURES

Figure Page

Figure

Page

LIST OF TABLES

I. BACKGROUND

A. Introduction

The dynamical properties of radiation-induced point defects in metals have been investigated for more than two decades for reasons of both scientific interest and technological consequence. Although the techniques that have been employed measure defect concentrations and annealing kinetics, most are insensitive to defect configurations. Only recently have methods evolved for probing the geometrical configurations of defects, and of these the ultrasonic technique developed and demonstrated by D. Johnson[1/] seems to offer the most sensitive and complete set of measurements. The present study further develops the ultrasonic technique and applies the procedure to a study of aluminum alloys with iron and zinc. An attempt is made to interpret the results with the aid of existing models for the trapping of interstitials at impurities. However, it is found that considerable extensions of existing models are required.

This paper is divided into four parts. In the first part, sufficient background material is presented to define the problems to be investigated. Also, refinements to the experimental apparatus and procedures developed by Johnson are discussed. In the second part experimental results are presented for three alloys: (1) the Al-Mn results for a C_{44} mode which largely confirm Johnson's results, (2) the Al-Fe results which add new data to existing internal friction

measurements for the C_{44} mode, and (3) a detailed new set of measurement for two different concentrations of the Al-Zn alloy. In the third part present theory for paraelastic relaxation processes is summarized and predictions for diaelastic modulus changes are discussed. Also included is a calculation for diaelastic and paraelastic effects expected for simple two-state and four-state defect models that include tunneling effects. The fourth part includes interpretations of the effects observed in Al-Zn and Al-Fe.

The interpretation[2,3,4] of radiation damage experiments is based largely on extensive measurements of radiation-induced changes in resistivity in various F.C.C. metals and alloys. Irradiation with neutrons, gamma rays, or high energy electrons or other particles is known to cause displacement of atoms from the crystal lattice creating Frenkel pairs (F.P.) of vacancies and interstitials that are separated by distances on the order of a few interatomic spacings. Defects so introduced act as scattering centers for electronic conduction so that resistivity change is a measure of the total concentration of Frenkel pairs. Following low temperature irradiation, typically three distinct stages of annealing behavior are observed, called stages I, II, and III. Stage I, near 35K in Al, corresponds to annealing effects resulting from the migration of interstitials, while stage III, near 200K in Al, corresponds to vacancy motion. For very pure materials, there is a more or less structureless annealing which occurs over a wide range between stages I and III known as stage II. For other than very pure materials, stage II is found to have distinct substages which depend upon the

impurity type and content. Most F.C.C. metals exhibit five substages during stage I annealing. Kinetic analysis of the annealing process indicates that the first three substages result from the recombination of close Frenkel pairs.[5] The fourth substage results from the correlated recombination of more distantly separated pairs, while the final substage represents the free migration of interstials and their random recombination with vacancies.[6]

While the basic structure of stage I seems to be material independent, stage II exhibits a wide variety of annealing stages that seem to characterize material composition. Damage that survives stage I annealing arises from immobilized interstitials (and their vacancies) that were captured during free migration at trapping sites that are mainly impurity atoms in impure materials and interstitial clusters in pure materials. Stage II annealing results from the release or reconfiguration of trapped interstitials. Strongly bound interstitials may survive through stage II annealing also. Then, in stage III, vacancies are activated and migrate until they recombine with the trapped interstitials.

A complete understanding of any radiation damage process must include knowledge of the geometrical configurations of both isolated and trapped interstitials. Early attempts by Huntington and Seitz[7] to calculate isolated interstial configurations from known lattice parameters were frustrated by the strong sensitivity of the results to the choice of the interatomic potential. In later more refined calculations by Gibson, et al,[8] and by R. A. Johnson[9] and others, the

<100> split dumbell was usually found to be the configuration of highest stability. Experimental measurements of the isolated interstitial configuration have only recently been attempted. Holder, Granato, and Rehn,[10] using an ultrasonic technique, measured diaelastic modulus changes in pure copper for Id defects. The large and anisotropic relative modulus changes observed were in good agreement with estimates made by Dederichs[11] for the <100> split configuration. Using an elastic-after-effect technique, Spirić, et al.[12] have observed a relaxation process in aluminum attributed to the anelastic relaxation of single self-interstitial atoms. The crystal orientation dependence of the process is consistent with that expected for a <100>-split configuration. Additional experimental evidence for the <100> split configuration has been obtained from small angle x-ray scattering measurements.[13]

The configuration of interstitials trapped near impurity atoms in F.C.C. metals was considered by Dederichs.[14] He developed a simple model amenable to numerical calculation in which impurities are characterized solely by their fractional misfit in size to the host lattice. In this model, a slightly undersized impurity atom will trap an interstitial atom forming a tightly bound "mixed dumbbell" defect with <100> symmetry. Only small energy barriers separate the six equivalent <100> sites surrounding the impurity. The interstitial is thus confined to a "cage" centered on the impurity, but may undergo relaxations among the six sites. Furthermore, this model predicts that oversized impurities would only weakly bind interstitials and would not form the mixed-dumbbell configuration.

Experimental results obtained so far provide some support for the trapping configurations of this model, but they also conflict with it in some aspects. Evidence for caging near impurities was provided by the Mössbauer experiments of Vogl and Mansel.[15] Their measurements of Al-^{57}Co(^{57}Fe) indicate that interstitials are trapped near iron following irradiation. Their observation of a rapid decrease of the Debye-Waller factor in a narrow temperature interval near 20K indicates the onset of large amplitude displacements which can be interpreted as a thermally activated caging motion. Their measurements[16] using a silver host lattice display similar behavior. However, the large difference in activation energies between the two systems cannot be accounted for in the Dederichs model by the known small difference in lattice volumes of aluminum and silver.

Swanson et al.[17] have tried to deduce trapping configurations in several dilute aluminum alloys using channeling measurements. Their technique involves measuring the backscattering of He^+ ions from displaced impurity atoms. From analysis of the crystal orientation dependence of the backscattering, they were able to show that for Mn, Fe, Zn, and Ag impurities in Al, the trapping configuration was the <100>-mixed dumbbell. Also, in agreement with Dederichs' size rule, the oversized impurity Sn was found not to form mixed dumbbells. The channeling measurements generally support Dederichs trapping model; however, the limited sensitivity of the technique requires the use of very high radiation doses so that defect interactions may complicate the interpretation of the results. Also, the technique cannot separate the effects when multiple defect species are present.

There appears to be some conflict between Swanson's interpretation of the channelling results, and Wollenberger's[18] interpretation of his resistivity measurements. Wollenberger concludes that there must be a series of traps in general, with only a relatively small concentration of interstitials in the deepest traps which correspond to mixed dumbbells.

Rehn, Robrock, and Jacques[19] using a torsion pendulum technique have observed multiple strong relaxation processes in irradiated Al - Fe. One strong low temperature peak may possibly be associated with the large drop in the Debye-Waller factor of the Mössbauer experiments. However, although they were unable to measure the C' mode effects directly, their measurements on polycrystalline and C_{44}-oriented single crystals indicated that the observed peaks, in contrast to the channeling results, derived from defects that did not have the symmetry of <100> mixed dumbbells.

Recent ultrasonic measurements by D. Johnson[1] on the Al-Mn alloy are in striking contrast to the Al-Fe internal friction measurements. This is a surprising result since the trapping model prediction is that similarly sized impurities, such as Mn and Fe, should exhibit similar trapping characteristics. Johnson observed a number of relaxation peaks in the ultrasonic attenuation spectrum that could be distinguished through their annealing behavior as arising from distinct defects. None, however, could be identified as arising from the <100> mixed-dumbbell.

In summary, although further measurements are required, a consistent picture has emerged for the configuration and dynamics of self-interstitial

atoms in F.C.C. metals. The situation for trapped interstitials, however, is not so clear. A major problem is the dilemma posed by the channeling experiments that indicate the formation of <100> mixed-dumbbell trapping configurations and the internal friction and ultrasonic measurements that indicate the absence of defects of <100> symmetry. A second problem is the observation that similarly sized impurities can have greatly different trapping properties.

Of the available means for probing interstitial trapping properties, the ultrasonic technique developed by Johnson seems to be the most promising. The high sensitivity of the method allows measurements on defects present in concentrations at the part-per-million level. Compared to the channeling technique, the ultrasonic technique allows measurement not only of the trapping configuration but also of the reorientation energy even in the presence of multiple defect species. Ultrasonic measurements are also preferred over lower frequency, internal friction measurements. The ultrasonic technique allows measurements for each of the symmetry modes of the crystal, whereas, the torsion pendulum technique can directly measure only the C_{44} mode. Also, the ultrasonic technique needs the preparation of only a single sample for all of the measurements. Finally, another attractive feature of the ultrasonic technique is that it allows, for various excitation frequencies, the simultaneous measurement of both diaelastic and paraelastic modulus changes and paraelastic attenuation effects.

The present work attacks the trapping problem in two ways. First, an attempt is made to resolve or more clearly define the conflict

between the Al-Fe internal friction results and the channeling results. Secondly, in a search for the general trapping properties of undersized impurities, the survey of trapping configurations is extended to another aluminum alloy, Al-Zn.

There are many choices for systems that might be the next logical candidate for study. The Al-Zn system seemed particularly attractive for several reasons. First, several investigators[20,21,22] have studied the alloy with resistivity annealing experiments, and they have demonstrated the existence of Zn trapping sites and detrapping during stage II. Sosin and Rachal[23] have shown that the recovery near 200K follows second order kinetics as expected for stage III, and that a major annealing substage near 130K proceeds by first order kinetics. Also, Swanson included measurements on the alloy in his channeling experiments that indicated that <100> mixed-dumbbells were formed at lower temperatures, but that near 130K some type of reconfiguration occurs that removes the mixed-dumbbell defects. In several aspects, the Al-Zn system seemed preferable to the Al-Fe and Al-Mn systems for comparison with trapping model predictions. Zinc is readily soluble in the alumninum host and thus avoids the possible complications with impurity precipitates of other alloys. Also the solubility allows for the study of possible impurity concentration effects over a wide range of alloy concentration. The filled d-shell structure of the zinc impurity avoids possible electronic effects that may contribute to the Al-Fe and Al-Mn systems. Finally, compared with Mn and Fe, Zn is only a very slightly undersized misfit impurity in the Al host. It is possible, therefore, that Al-Zn

system measurements will make better contact to the Dederichs trapping model which was developed as a perturbation of the model for isolated interstitials. Also, for small misfit impurities, the interstitial-impurity binding energy is expected to be small, so that a detailed study of thermally activated detrapping becomes a possibility.

The Al-Fe system was studied in some detail. The first measurements of C' mode paraelastic attenuation effects are presented. Also, C' and C_{44} mode diaelastic modulus changes are measured. The simultaneous combination of diaelastic and paraelastic measurements provides more complete and useful data than either or both measurements taken separately. A comparison of the annealing behavior of the paraelastic and diaelastic data leads to a possible resolution to the seeming contradiction between the internal friction results and the channeling results. A thorough investigation of the Al-Zn system is carried out for two alloy concentrations. Diaelastic and paraelastic effects are separated out, and their annealing behavior is correlated with simultaneously measured resistivity changes. Multiple trapping processes are observed, but the predominant defect species is interpreted as a <100> mixed-dumbbell in agreement with the channeling results.

B. Experimental Technique

The ultrasonic technique employed in this study has been described in some detail by D. Johnson.[1/] In this section, a brief description of the techniques is presented along with details of apparatus and procedures that have been modified.

1. Apparatus

The ultrasonic samples were cut from boules of single crystal Al-Fe and Al-Zn grown by Monocrystals (Cleveland, Ohio). The samples were oriented using the x-ray scattering technique developed by Ochs.[24] A wire acid saw was used to cut approximately cubic samples of one centimeter dimensions with two (100) faces and four (110) faces. One pair of (110) faces was polished flat and parallel to optical tolerances using an electrochemical crystal facing machine. The remaining (110) pair was also polished to provide good thermal contact to the sample holder. Wet chemical and spectrographic analyses were performed on small pieces cut from the same boules to verify sample purity and alloy concentration.

Figure 1, given by Johnson, shows the placement of the sample in the sample holder and the physical arrangement for 2.5 MeV electron irradiation. A focused electron beam supplied by the Van de Graaff facility in the Materials Research Laboratory strikes a thin aluminum scattering foil, C. Water cooled collimating appertures, D and E, pass approximately 10% of the incident beam, which then strikes the sample as a one centimeter diameter beam of fairly uniform (±5%) intensity. A motor driven flap containing a BeO disc, B, and a closed circuit television system aid in initial alignment of the beam, while the motor driven current flap, F, can be periodically lowered to sample the beam current.

The sample temperature is measured with a platinum thermometer and an AC current bridge similar to that described by Kirby.[25] The low temperature range of the thermometer (5K - 40K) was first calibrated

Figure 1. Cross section of cryostat, sample holder, and electron beam interface.
(A) e^- beam entry port
(B) BeO disc beam alignment flap
(C) scattering foil
(D) first apperture
(E) second apperture
(F) current monitor flap
(G) gate valve
(H) LN_2 shield
(I) sample chamber window
(J) cooling coils
(K) bypass valve
(L) viewing port

[after Johnson[1/]]

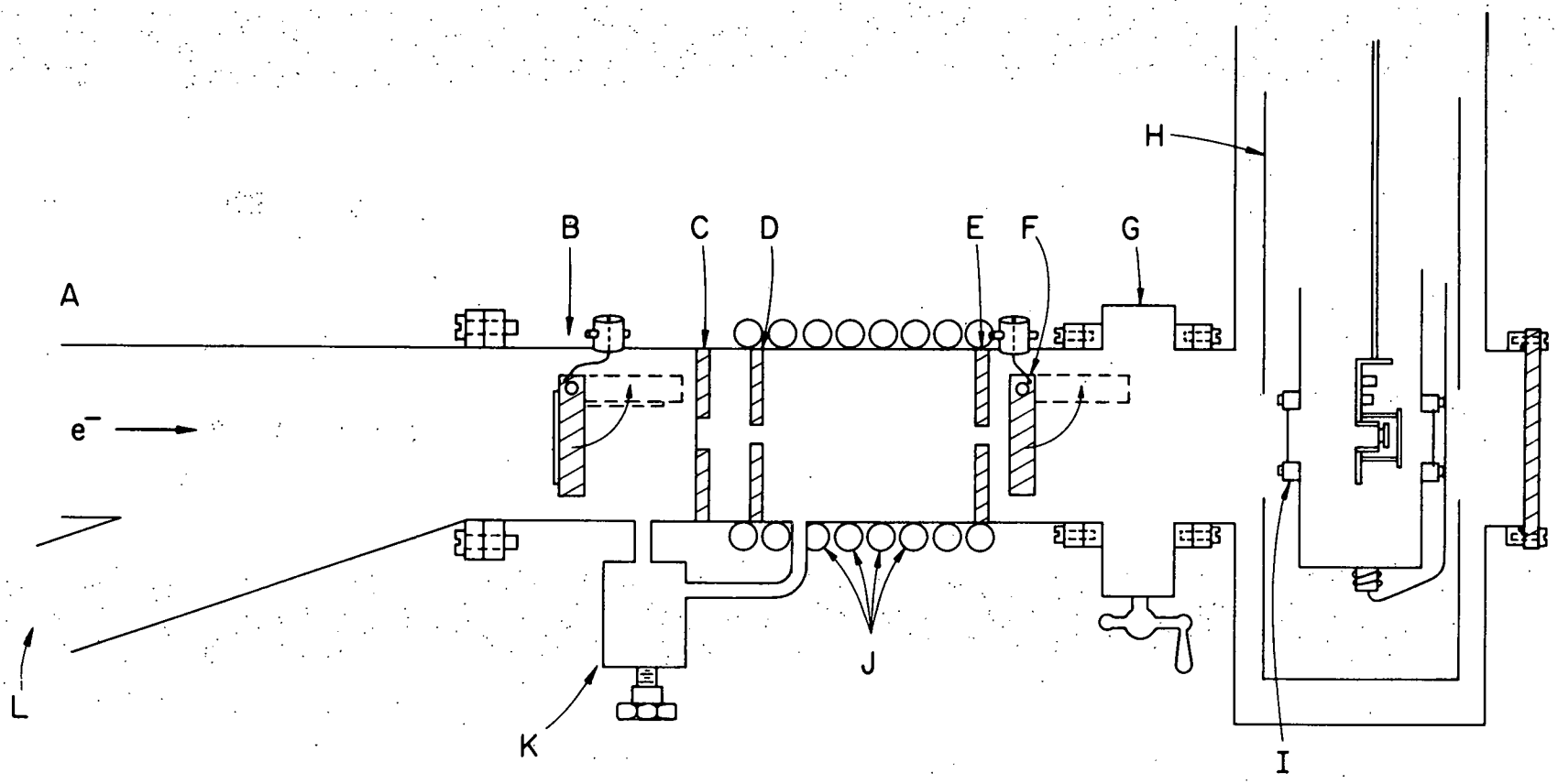
A
B
C
D
E
F
G
H
e⁻
L
K
J
I

against a commercial germanium standard thermometer with an accuracy of about 10 mK. The lowest temperatures, 2K - 10K, were measured with a carbon resistance thermometer that was calibrated against the germanium thermometer and corrected on each run by comparison with the platinum thermometer. The precision in this temperature range, however, is estimated to be only about 100 mK.

A schematic diagram of the temperature measurement and control system is shown in figure 2a. The control loop is fairly conventional consisting of a thermometer bridge detailed in Fig. 2b and an integrating/differentiating temperature controller detailed in Fig. 2c. An offsetting digital ramp votage may be injected into the temperature error control signal so that, for small temperature ranges, nearly linear temperature ramps can be generated. Provision is made for breaking the control loop and rapidly resetting the bridge and the ramp generator so that long temperature ramps can be generated. However, it is estimated that temperature drift during the turn-around at the end of each of the short ramps is one of the major sources of temperature error.

Unplated quartz shear transducers purchased from Valpey-Fisher (Hopkinton, MA.) are used for the ultrasonic measurements. For the C' mode runs, the propagation direction was <110> and the polarization was $<1\bar{1}0>$. The C_{44} mode runs were done using either a <110> propagation direction and <001> polarization or a <100> propagation direction with random polarization. The bonding technique has proved to be very successful. First, the bonding surface is prepared to a mirror-quality finish by electrochemical polishing. Then, a small quantity of the

Figure 2. Temperature control system.

A. (top) control loop schematic.

B. (lower left) platinum thermometer bridge schematic.

C. (lower right) integrating/differentiating controller schematic.

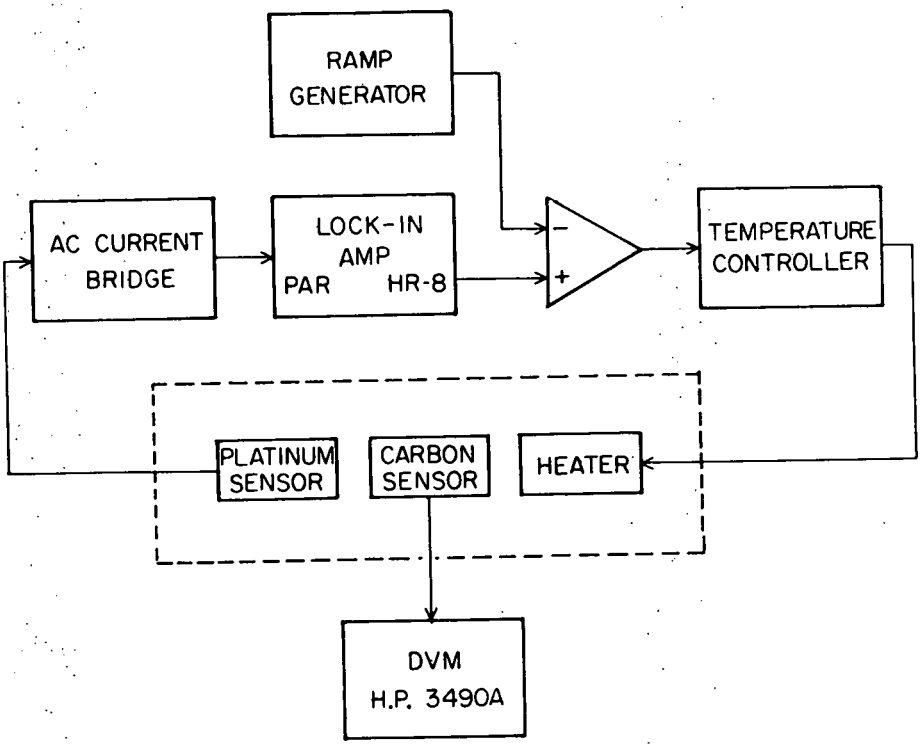

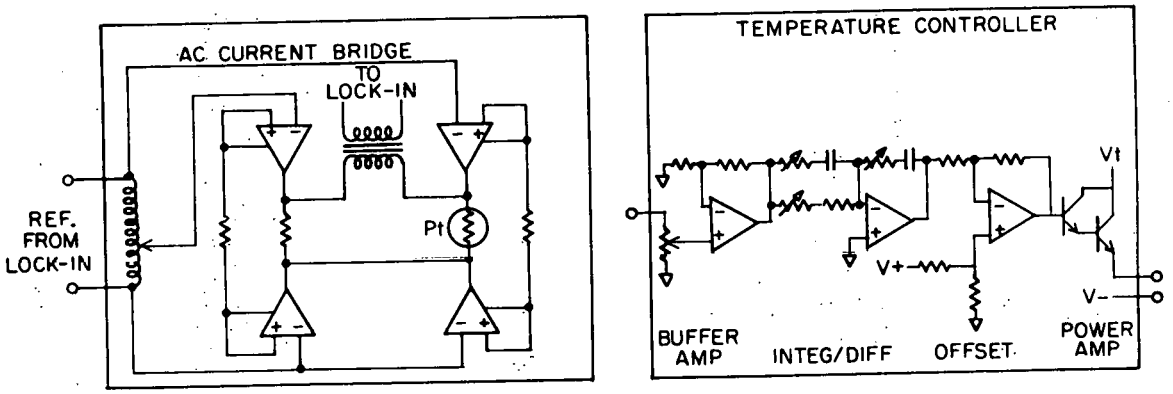

TEMPERATURE CONTROL SYSTEM

bonding agent, Nonaq stopcock grease, is outgassed by gently heating in a rough vacuum for a few minutes. The sample surface and the transducer are cleaned and dried and then heated to about 40 C. A minimum amount of grease is then applied to the sample, and the transducer is gently pressed into place. The quality of the bond can be judged visually through the unplated transducer and tested at room temperature with a pulse-echo system. Small diameter transducers, 1/4 in., are used to minimize the shear strain produced by the differential thermal expansion of quartz and aluminum. Even so, curious small jumps of undetermined origin were sometimes observed in the attenuation during temperature ramping and immediately following the initial freezing of the bonds around 200K. The jumps were again occasionally observed during ramping in the latter stages of the annealing program. Since the sample is thicker than the penetration depth of 2.5 MeV electrons, the transducer and bond are protected from damage by irradiating the opposite face of the crystal.

Attenuation measurements were initially made using conventional pulse-echo and attenuation recording equipment purchased from Matec, Inc. (Warwick, R.I.). Measurements were recorded at one frequency, 10 MHz, over some temperature interval. Then, the system was retuned for a second frequency, 30 MHz, and the same temperature interval was scanned. It soon became clear that there were a number of advantages to be gained by developing a system for simultaneously recording the attenuation at both frequencies. First, the possible savings of time is obvious. For any one run, the savings, which might total in the

many ten's of hours, would both reduce operators time and produce a considerable savings of liquid lrelium. Another advantage is that data for both frequencies can be collected even for attenuation peaks that anneal out while they are being measured. The simultaneously recorded attenuations are taken at identical temperatures so that their relative behavior is precise even when the absolute temperature error is fairly large. This observation was particularly important at the lowest temperatures where the system was allowed to slowly drift in temperature while the attenuations were recorded. Also, the task of initially locating those peaks that are near the system noise level is aided greatly by the ability to observe the relative behavior of the two attenuations. Finally, the pulse generators and receivers are finely tuned amplifiers. Simultaneous operation eliminates the difficult and imprecise chore of frequently retuning all the tuned circuits.

A schematic diagram of the attenuation system is shown in Fig. 3. Two commercial pulse-echo and recorder systems are utilized that are externally triggered on alternate phases of a 200 Hz square wave. The r.f. signals from the two pulse generators are mixed at the transducer following individual matching networks. It was found that there was a large interaction between the two tuning networks that considerably broadened the tuning of each and hence the transmitted amplitudes. However, the echo patterns as observed on the oscilloscope and the recorded attenuations did not appear to be affected.

The velocity system is shown in schematic form in Fig. 4. The sampled-continuous-wave technique is employed. The excitation frequency

Figure 3. Attenuation system schematic diagram.

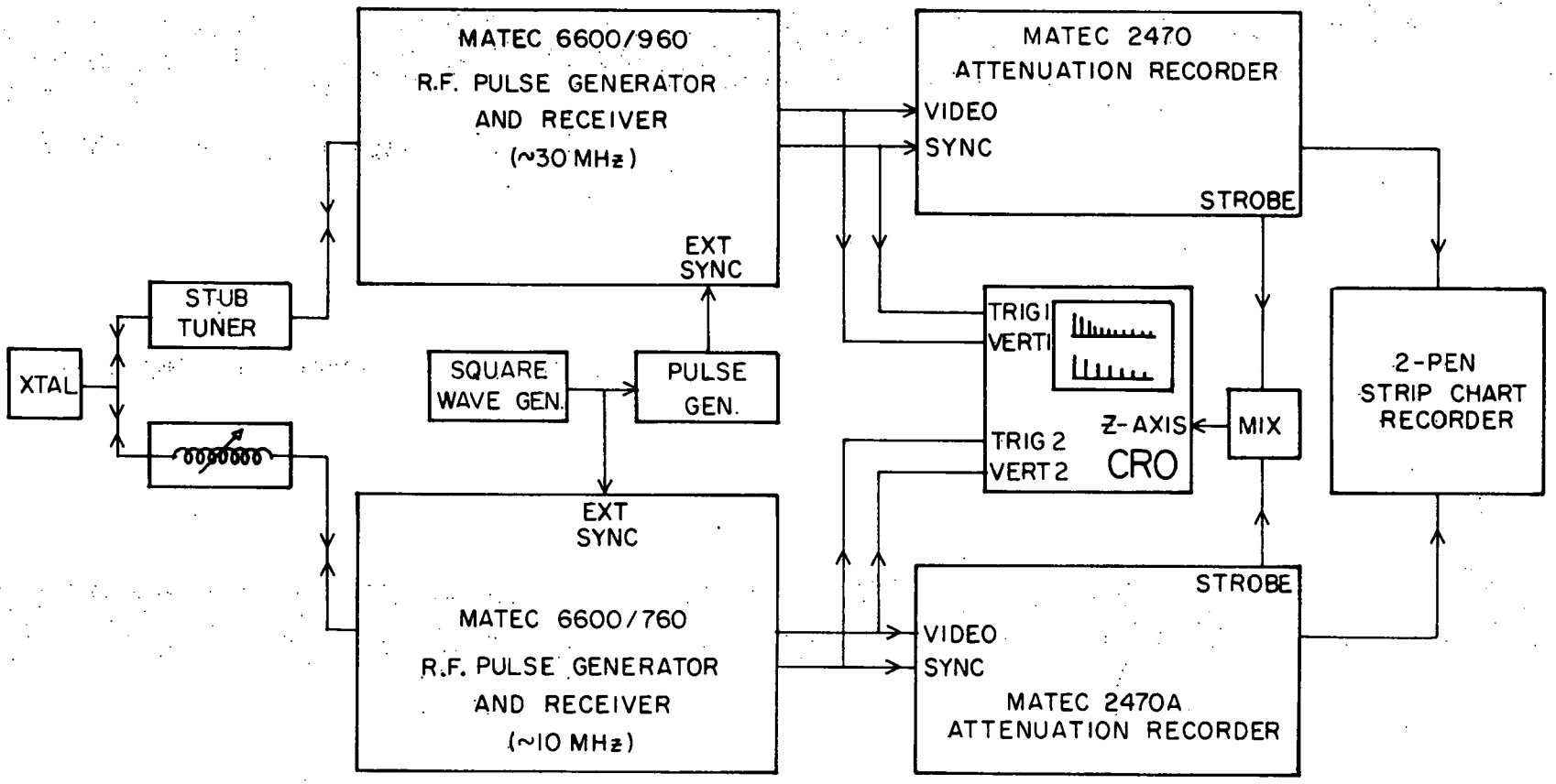

Attenuation System

Figure 4. Velocity system schematic diagram.

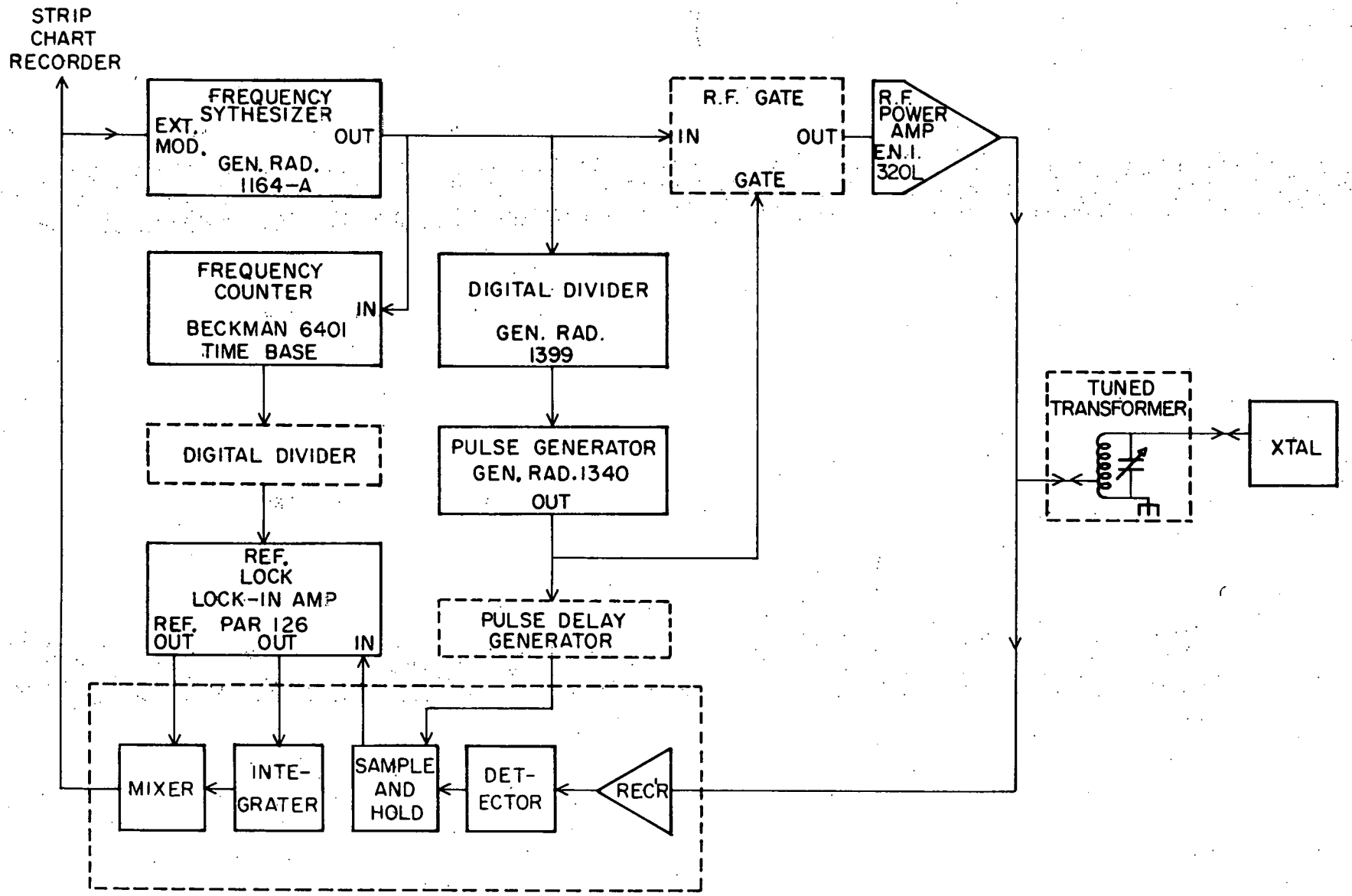

Velocity System

is slowly dithered around an odd harmonic of the sample resonant frequency. (The sample harmonics are approximately 100 kHz apart and it is fairly easy to find one near the broad 10 MHz transducer resonant frequency.) The driving power amplifier is periodically gated off and the amplitude of the sample strain is measured. The strain amplitude signal is synchronously detected with the dithering frequency, and a feedback signal is derived to maintain maximum amplitude. The digital counter then displays the frequency of the chosen harmonic of the sample resonant frequency. An analog signal proportional to the deviation of the resonant frequency is provided for continuous recording during temperature ramping. Finally, the resonant frequency, f, is given by

$$f = n\, v/2L \tag{1}$$

where v is the sound velocity, L is the sample length, and n is an odd integer. Since v is given by $\sqrt{C/\rho}$ where C is the elastic modulus and ρ is the density, one obtains

$$2\Delta f/f = \Delta C/C + \Delta L/L. \tag{2}$$

The relative modulus change is then twice the relative frequency change when length changes can be neglected.

Resistivity measurements were made for three reasons. First, the concentration of impurities that had gone into solution during the preparation of the alloys could be estimated from the known values of resistivity per substitutional defect as tabulated by Fickett[26] and the measured values of residual resistivity ratio, RRR. It was found that,

for the Al-Zn alloys, the concentrations so obtained agreed very well with the results of chemical analysis. However, for the Al-Fe alloy, the measured RRR indicated that the substitutional concentration was only about 40% of that indicated by chemical analysis. The rest of the iron is present probably in the form of precipitate particles. Second, using the fairly well determined value for pure Al of 4 μΩ-cm per at.% of Frenkel pairs as reported by Schilling[27], the resistivity change upon irradiation can be used to estimate the total damage produced. The F.P. concentration in the ultrasonic sample can then be estimated using the averaging procedure outlined by Johnson. Third, resistivity annealing data can be collected and correlated with the annealing of the paraelastic and diaelastic effects.

It was found that resistivity samples placed alongside the ultrasonic sample could accurately measure the irradiation flux only if precision alignment with the beam could be maintained. This restriction could be eased by enlarging the beam, but that would lead to increased liquid helium consumption. It was decided to use thin wire-shaped samples placed across the beam directly in front of the ultrasonic sample. The samples were prepared by electrochemically polishing discs to a thickness of about 10 mil and then slicing the discs into 10 mil wide strips using a spark cutter. The small dimensions of the samples ensured minimal disturbance of the irradiation of the ultrasonic samples. The annealing behavior of the resistivity samples indicated that the temperature rise during irradiation could not have exceeded 10K.

Electrical lead attachment posed a particularly difficult problem. The first few runs were done with copper leads that were spot-welded to

the aluminum sample. However, it was found that the welds would fail after a few thermal cycles at the early part of the runs. Soldering was then attempted using special aluminum solder and flux purchased from Indium Corp. of America (Utica, NY). However, it was found that well-separated and good solder joints could not be formed in the small space available. Finally, it was found that stable and reliable measurements could be made using four discrete pressure contacts to the sample. The phosphor bronze contacts were gold plated and spring loaded. The resistance measurements were found to agree with calculations based on the sample dimensions and known resistivities.

The system for measuring resistances is schematically diagramed in Fig. 5. Geometrical factors necessary for calculating resistivity were obtained from room temperature resistance measurements and known values (see Fickett) of room temperature resistivity. The system is a modification of the AC current bridge described by Kirby[25] and has been discussed in some detail by Johnson.

2. Experimental Procedures

Since the energy loss mechanisms that cause ultrasonic attenuation are additive processes, the effects due to irradiation induced defects can be obtained by subtracting off a pre-irradiation, or background, attenuation as a function of temperature. Background runs were done on the initial cooling from room temperature down to 5K. A steep drop in attenuation was always observed in the range from room temperature down to about 240K probably because of the gradual freezing of the grease bond. From 240K down to about 100K the background is fairly flat or

Figure 5. Resistivity system schematic diagram.

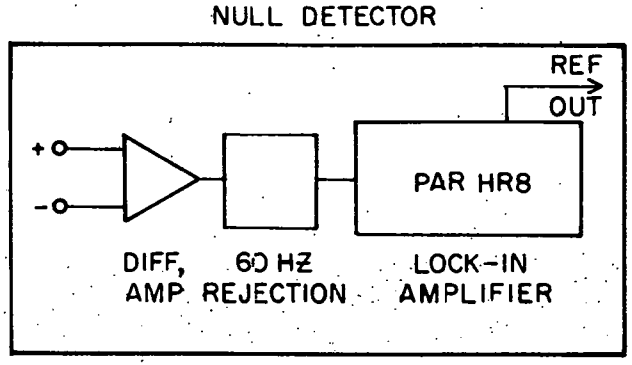

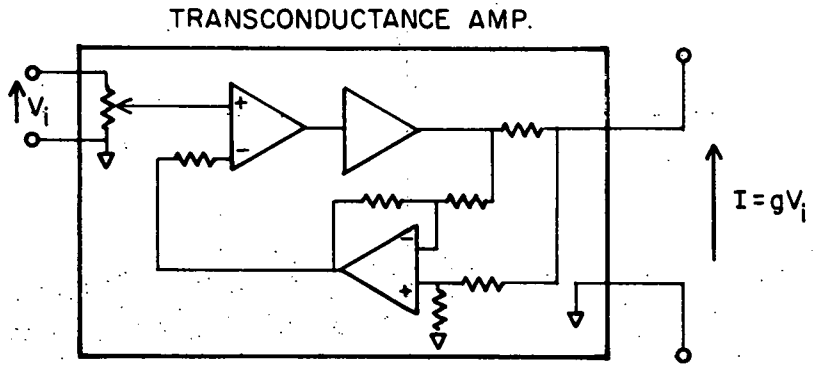

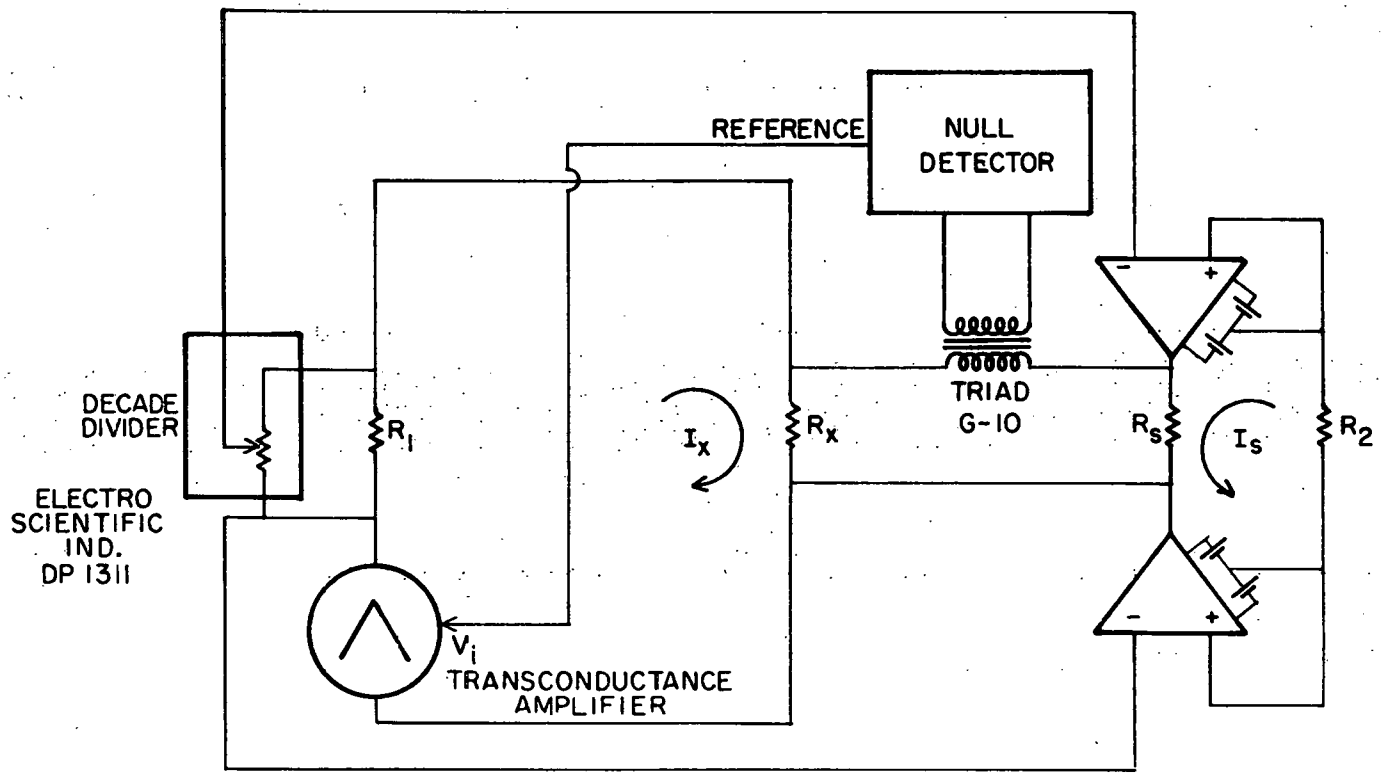

Resistivity System

slightly sloping downward possibly because of reduced thermal phonon losses at lower temperatures. Sometimes, particularly in the 30 MHz background, a number of small, ill-defined oscillations of the attenuation as a function of temperature were observed. Their origin was undetermined. From 100K down to about 15K, the attenuation was observed to rise again. This energy loss was determined to be of electronic origin and provided valuable alloy concentration and damage production rate information to be described below. The region from 15K down to 2K was found to be fairly flat because of the slow temperature dependence of the electronic losses in this region. The 10 MHz and 30 MHz backgrounds were fairly similar, except for the expected larger value of the electronic losses at the higher frequency. Background measurements were also taken of the resomant frequency in the range from 2K up to about 40K. Up to about 20K, the background is fairly flat. The upper limit is determined by the temperature stability and the rather precipitous drop of the modulus (roughly T^4 dependence) above 35K. Pre-irradiation values are also recorded for resistivity at 5K and 10K.

The temperature control was set for 65K during irradiation. The actual sample temperature was estimated to be 5K to 10K warmer by measuring the change in attenuation due to heating when the beam was turned on. Later irradiations of Al-Zn were carried out at a reduced temperature, 50K, in a search for annealing effects related to a resistivity annealing peak observed near 70K. Irradiation with 2.5 MeV electrons at a total beam current of about 4μA continued for several days

in order to produce a volume averaged F.P. concentration of about 5 ppm. Between each day of irradiation and after the last day, the temperature was ramped down to 5K while measuring attenuation. The resonant frequency and resistivity were recorded. No evidence was seen of damage saturation effects in the resistivity increment, the diaelastic modulus changes, or in any of the paraelastic attenuation peaks that were observed.

The annealing program consisted of a series of linear temperature ramps from 5K up to a chosen anneal point followed by a 10 minute anneal and a linear ramp back to 5K. After each anneal point, the resonant frequency and resistivity were measured at 5K and 10K. For the Al-Zn alloys, attenuation and frequency measurements were made while drifting up in temperature following a pump-down to 2K. The choice of annealing points had to be made fairly carefully since each point, particularly those near stage III, represented many hours of ramping. When accurate measurements were required, the ramping speed was limited to 0.5 to 1.0 degrees/minute in order to maintain temperature errors under .5K at high temperature and .1K at low temperature. When larger temperature errors could be tolerated, ramping speeds of 2 to 3 deg./min. were used. When possible, annealing points were chosen with the guidance of resistivity annealing data. Points were chosen to crudely approximate constant heating rates in order to aid analysis. It was found that the frequency annealing measurements were good only up to about 200K, since large background shifts occured as the bond was beginning to soften. On the other hand, data for the annealing of peaks in the attenuation could be

recorded even following a 240K anneal since shifts in the attenuation background are relatively small and only weakly temperature dependent.

One component of the attenuation has been found to be proportional to the electrical conductivity of the specimen. This component is easily identified by its temperature and frequency dependence. Since impurity and defect concentrations are normally determined by electrical resistivity measurements, one has here the possibility of measuring defect densities ultrasonically without the need of separate electrical resistivity measurements. In fact, there are several advantages to the ultrasonic measurement. In addition to the possibility of eliminating the resistivity sample altogether, the technique has the advantage of yielding a bulk measurement of resistivity. For small radiation-induced resistivity changes compared to the sample resistivity, the ultrasonic attenuation directly measures a volume-averaged resistivity in the same way that paraelastic and diaelastic effects result from a volume-averaged damage concentration. Also, the technique eliminates possible errors from beam inhomogeneity. Corrections for both average irradiation flux and sample thickness must be made when a separate sample is used for resistivity measurement.

The present understanding of ultrasonic attenuation is normal metals has been reviewed by Rayne.[28] The attenuation of sound waves by interaction with conduction electrons was first reported by Bömmel.[29] Soon after, Mason[30] presented a theory for the effect in which the viscoity of the metal is related to the electrical conductivity by the use of kinetic theory applied to a free electron gas. The attenuation arises

when, because of the viscosity, momentum is transferred from the ultrasonic wave to the electron gas. The calculated attenuation is proportional to the electrical conductivity and to the square of the frequency. The theory breaks down when the electron mean free path, ℓ, becomes comparable to the ultrasonic wavelength, λ. At room temperature and for an ultrasonic frequency of 30 MHz, the condition $\ell << \lambda$ is well met. However, at low temperatures and in very pure metals, ℓ becomes larger than λ. A more general theory[31,32] has been developed that is valid over the entire range of mean free paths and which is capable of dealing with non-spherical Fermi surfaces. For $\ell << \lambda$, the attenuation becomes independent of conductivity and proportional to only the first power of frequency. A simple estimate of ℓ for the Al-Fe and Al-Zn alloys can be made using free electron gas formulas. First, the electron collision time, τ, is related to the electrical conductivity, σ, by

$$\tau = m\sigma/Ne^2 \tag{3}$$

where N is the number per unit volume of electrons of charge e and mass m. Then, $\ell = v_F\tau$ where v_F is the Fermi velocity given by

$$v_F = (\hbar/m)(3\pi^2N)^{1/3}. \tag{4}$$

Using 3 electrons per aluminum atom, N can be calculated. The worst case or largest value of ℓ can be calculated using the conductivity of the Al-Fe alloy at 5K and the resistivity-per-impurity atom tables of Fickett.[26] For an alloy concentration of 60 ppm, $\ell = 10^{-4}$cm. For comparison, $\lambda = v/f$ where v is the shear wave velocity. For Al at 30 MHz, $\lambda = 10^{-2}$cm. So,

the condition $\ell << \lambda$ should be well satisfied for all of the present ultrasonic measurements, and the low frequency limiting form for attenuation should apply.

In the low frequency limit, the shear wave attenuation, A is given by

$$A = (2\pi^2 f^2/\rho v^3)(3\pi^2 N)^{2/3} (\hbar^2 \sigma/5e^2) \qquad (5)$$

where ρ is the sample density. The ultrasonic attenuation from 5K to 80K at 30 MHz for Al - .1% Zn was found to vary linearly with calculated conductivity. Also, using the 10 MHz and 30 MHz data, the distinctive f^2 dependence was observed in each alloy. However, using the Al-Zn background attenuation curves from 5K to 80K and calculated conductivities, it was found that the measured attenuation was larger than that predicted by Eq. 5 by a factor of 1.2 for the C_{44} measurements and a factor of 1.8 for the C' measurements. The discrepency is large and remains unexplained. A similar result, however, was obtained by Lax.[33] His attenuation measurements on high purity polycrystalline Al at 20 - 100 KHz when compared with simultaneously measured conductivities revealed a similar discrepency of a factor of 1.52. He pointed out, however, that the discrepency may be traced to the assumption that the mean free path is the same for the acoustic process and the electrical conductivity. Steinberg[34] has calculated for shear waves an acoustic mean free path only one third that for electrical conductivity. The factors of 1.2 and 1.8 obtained from Al - .1% Zn background runs at 30 MHz were used for all other conductivity calculations based on attenuation.

II. EXPERIMENTAL RESULTS

A. Scope of the Measurements

Ultrasonic attenuation and velocity were measured before and after electron irradiation of Al-Mn, Al-Fe, and Al-Zn alloys. In addition to the electrical conductivity-dependent attenuation discussed earlier, two distinct types of effects were observed. By analogy with related magnetic effects, the elastic effects are described as diaelastic and paraelastic phenomena.

In general, an externally applied strain field will induce a polarization of crystal defects. The response is described by the diaelastic polarizability of the defects. For a large crystal with many defects, the polarization response leads to a reduction of the elastic constants. The effect is characterized by temperature and frequency independence in the range of these measurements.

In addition, a low symmetry defect will give rise to a permanent elastic dipole moment. In an unstrained crystal, the elastic dipole may be oriented along any of the equivalent crystal directions. In an externally applied strain field, some of the orientations may become energetically favored over the others. Then, through thermal excitation, the dipoles will tend to make transitions to the favored directions. For a large crystal with many defects, the response again leads to a reduction of the elastic constants. This paraelastic process also gives rise to an attenuation. The temperature and frequency dependence of

the modulus and attenuation are given by the well-known Debye equations:

$$\frac{\Delta C}{C} = \frac{R}{\pi} \frac{1}{1 + \omega^2\tau^2} \tag{6}$$

$$\Delta = R\frac{\omega\tau}{1 + \omega^2\tau^2} \tag{7}$$

where C is the elastic constant, Δ is the logarithmic decrement, R/π is the relaxation strength, ω is the frequency, and τ is the relaxation time constant. The decrement is related to the experimentally measured attenuation, α, by the standard relation[35]

$$\Delta = 0.115\ \alpha/f \tag{8}$$

where f is the frequency in MHz and α is measured in dB/μsec. The measured change in the resonant frequency, Δf, is related to the modulus change by Eq. 2, and, since f is given by Eq. 1, it is also related to the change in sound velocity, Δv, by

$$\Delta f/f = \Delta v/v - \Delta L/L. \tag{9}$$

For a thermally activated relaxation, τ is given by

$$\tau^{-1} = \nu_0 e^{-H/kT} \tag{10}$$

where ν_0 is a frequency factor and H is the activation enthalpy for the reorientation process. The relaxation strength can be expressed[36] as

$$R = \pi\beta c C^2 v_0 (\delta\lambda)^2/kT \qquad (11)$$

where β is a numerical factor of the order of unity, c is the atom fraction of defects, C is the appropriate elastic constant, v_0 is the atomic volume, and $\delta\lambda$ is the difference of some principal values of the λ-tensor which describes the strain produced by the defect.

Paraelastic effects, therefore, give rise to peaks in the attenuation as a function of temperature and to dispersions in the modulus as a function of temperature. Diaelastic effects also give rise to modulus changes. However, they are easily distinguished by their behavior as a function of temperature. Further details and estimates of the magnitude of both the diaelastic polarizability and paraelastic relaxation strengths for various defect configurations and ultrasonic propagation modes are presented in part III.

Table I is a list of the runs that were done in the order in which they were performed. The first line on the table is from Johnson[1/] and is included for comparison. The total dose is given as the integral of the beam current that was measured at the current flap. This number is presented as an accurate measure of the relative dose between the various runs and is not intended to be an absolute measure of dose. The concentration of defects is determined by other means, to be described later.

In Table II, the results of four methods of determining the alloy concentrations are presented. The results for the Al-Zn alloys are in good agreement with each other. For the Al-Mn alloy, chemical analysis

Table I. Summary of irradiation runs

RUN	Ultrasonic Sample	Propagation Mode	Ultrasonic Sample Length (cm)	Total Dose (μA-hr)	Resistivity Sample
---	Mn	C'	1.20	71.4	Mn
I	Fe	C_{44}	1.35	54.4	Mn
II	Mn	C_{44}	1.40	68.9	Mn
III	Fe	C'	1.30	67.1	Mn
IV	.1% Zn	C_{44}	1.15	56.9	Mn
V	Mn	C_{44}	1.36	93.8	Fe
VI	.1% Zn	C'	1.26	88.3	Fe
VII	.5% Zn	C'	1.08	112.0	.5% Zn
VIII	.5% Zn	C_{44}	1.10	77.6	.5% Zn

Table II. Alloy concentration measurements (at. ppm)

Sample	Chem. Analysis	Resistivity Sample	C_{44} Attenuation	C' Attenuation
Al-.1% Zn	920	---	1100	900
Al-.5% Zn	4800	4100	4700	4730
Al-Fe	150	80	42	44
Al-Mn	800	650	810	570

of a number of samples cut from the original boule revealed a considerable variation in concentration over the length of the crystal. All four reported values are for different Al-Mn specimens, and the variation may represent real concentration differences. For the Al-Fe samples, however, the discrepency between the chemical determination and the resistance determinations indicates that only 1/3 to 1/2 of the iron is in solution. The agreement between the two ultrasonic determinations (both using the same sample) is good. Concentration variations may again account for the difference between the ultrasonic and resistivity sample determinations.

Many possible models for defect configurations can be excluded by symmetry arguments based on the observed crystal orientation dependence of the paraelastic and diaelastic effects. However, a detailed comparison with specific defect models requires a measurement of the magnitude-per-defect of the radiation-induced elastic effects. For this reason, the total damage concentration was monitored using the standard technique of measuring changes in electrical resistivity. This technique relies on the assumption that each F.P. defect increases the resistivity by a fixed amount. This assumption has some theoretical[37] and some experimental[27] basis. However, there is reason to believe that trapped interstitials affect the resistivity differently than isolated interstitials. Takai, et al.[38] have calculated, that the resistivity contribution of various configurations of self-interstials, even, can vary by about a factor of two. Experimental measurements in this area are lacking. Dworschak, Monsau, and Wollenberger[18] recently discussed the

problem and came to the conclusion that the use of the standard value for pure aluminum, 4 μΩ-cm per at. % F.P., should lead to a systematic error for defect concentration no larger than 25%. For these reasons, the standard value was used to measure defect concentrations throughout the present work.

Damage rates were determined from radiation-induced resisitivity changes. Fair agreement was obtained between ultrasonic and electrical resistivity measurements. In Table III, the results are presented.

Table III. Damage rate measurements (F.P. ppm/μA-hr)

Sample	Resistivity Change	C_{44} Attenuation	C' Attenuation
Al-.1% Zn	---	.23	.31
Al-.5% Zn	.34	.37	.20
Al-Fe	.12	---	.14
Al-Mn	.11	---	---

The high resistivity of the Al-Mn samples precluded an ultrasonic determination for those samples. The numbers quoted are corrected for the thickness of the ultrasonic samples and are normalized to the total integrated beam current. Agreement with published[20] damage rate measurements for Al-Zn is good when the rates are normalized to flux by dividing by an incident beam area of about 1.3 cm^2.

The difference between the damage rates found in the Al-Zn alloys and those found in Al-Fe and Al-Mn is striking. The average value for

Al-Zn is 2.3 times larger than that for Al-Fe or Al-Mn. The difference is probably due to the high concentration of the zinc alloys. The iron impurities, in much lower concentration than the zinc, will trap only those interstitials which escape recombination with their own vacancies and freely migrate in stage Ie. The zinc impurities, on the other hand, are present in such high concentration that they may trap additional interstitials that would otherwise recombine with their own vacancies in stage Id. Evidence for this interpretation is provided by the stage I resistivity annealing measurements of Snead and Shearin[21] which show a reduction of the stage Id annealing peak at high impurity concentration. The reason for a difference in the damage rate for Al-Mn and Al-Zn for the same concentrations is not known. However, similar differences were observed in resistivity studies[39] of neutron damage in Al-Mn and Al-Zn.

B. Al-Mn Results

Because the attenuation peaks observed by Johnson in the C_{44} mode in Al-Mn are small and near the system noise level, it was decided to repeat the C_{44} measurements. The 10 MHz C_{44} results with background affects subtracted are shown in Fig. 6 along with Johnson's C' results for comparison. (The defect concentration has been normalized to 5 ppm F.P.) Basically, the C_{44} results are in agreement with Johnson. However, improved measurements were made of the activation energy and frequency factor for peak 4 (168K at 10 MHz). Also, the annealing behavior of peak 4 was more carefully measured. The results are shown

Figure 6. Ultrasonic decrement at 10 MHz for C' and C_{44} modes with background subtracted. The dotted line is a correction for annealing. [C' measurements from Johnson[1]]

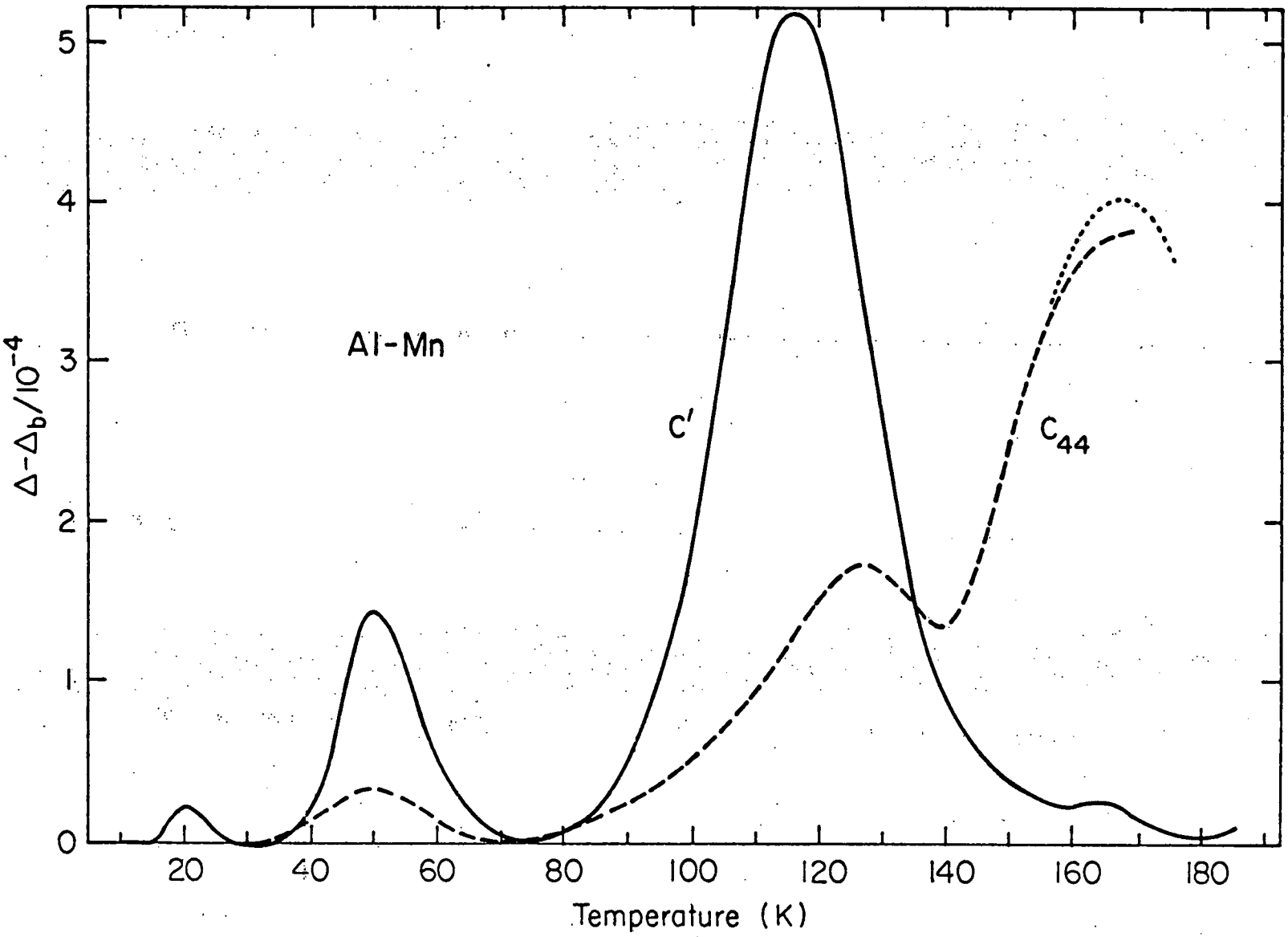
Al-Mn
C'
C_{44}
$\Delta-\Delta_b/10^{-4}$
Temperature (K)
0
1
2
3
4
5
20
40
60
80
100
120
140
160
180

in Fig. 7, and are also included in Fig. 8, which is a summary of the annealing of the resistivity and of the C' peaks given by Johnson.

The measurements on a simultaneously irradiated resistivity sample allowed for an improved determination of damage concentration. The revised characteristics of the attenuation peaks are summarized in Table IV where H and ν_0 are determined from an analysis of the temperature shift of the attenuation peak with ultrasonic frequency. From the

Table IV. Characteristics of attenuation peaks in Al-Mn

Peak Number	T_m (10 MHz)	H (meV)	ν_0 (sec^{-1})	$\Delta_{m/C}$	RT_m (10^3K)
1	21K	20.6±2.5	$10^{12.0\pm.6}$	4.0	0.17
2	51.7K	73±5	$10^{14.1\pm.5}$	30	3.10
3	118.5K	138±2	$10^{12.9\pm.1}$	102	24.2
4	168K	164±10	$10^{11.9\pm.3}$	76	25.5

Debye equations, one notes that an attenuation peak occurs when $\omega\tau = 1$. For a thermally activated process, then, the shift in peak temperature is given by

$$T_1^{-1} - T_2^{-1} = (k/H)\ln(\omega_2/\omega_1) \qquad (12)$$

where H is the activation enthalpy and $T_1(T_2)$ is the peak position for an ultrasonic frequency of $\omega_1(\omega_2)$. Then, ν_0 can be calculated using Eq. 10.

Figure 7. The decrement for the C_{44} mode at 10 MHz with the background subtracted following 10 min. anneals at the indicated temperatures.

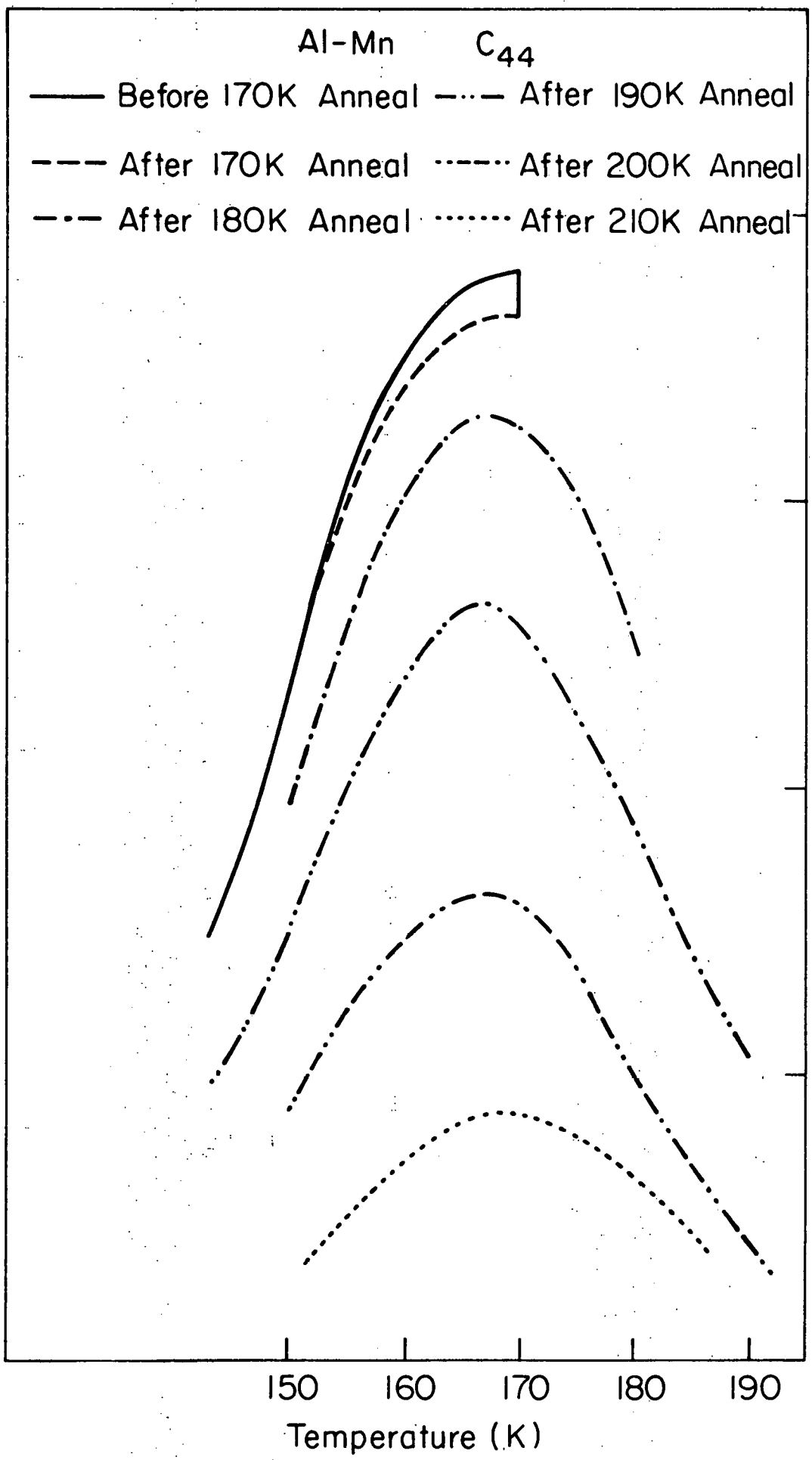
Al-Mn C_{44}
Before 170K Anneal
After 170K Anneal
After 180K Anneal
After 190K Anneal
After 200K Anneal
After 210K Anneal
4
3
2
1
$\Delta-\Delta_b/10^{-4}$
150
160
170
180
190
Temperature (K)

Figure 8. Annealing of Al-Mn peaks and resistivity. Each point is plotted relative to its post-irradiation value. [except for peak 4, data from Johnson[1]]

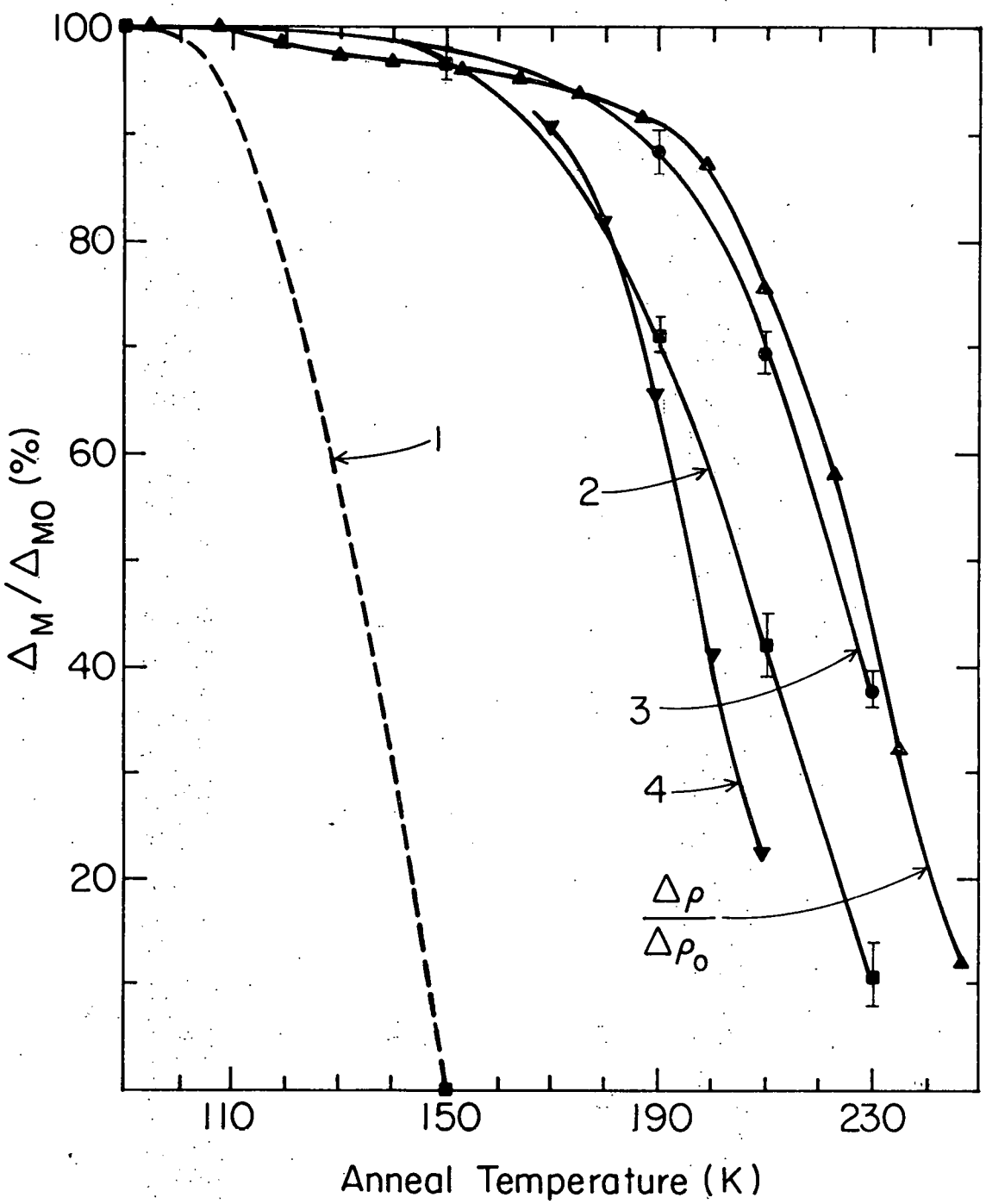
100
80
60
40
20
Δ_M / Δ_{MO} (%)
1
2
3
4
$\frac{\Delta\rho}{\Delta\rho_o}$
110
150
190
230
Anneal Temperature (K)

Also in Table IV, values are reported for Δ_m/C, the relaxation peak maxima per unit concentration of F.P., and for RT_m, the temperature compensated relaxation strength.

Resistivity sample annealing data were recorded and are presented along with data from Ceresara, et al.[39] in Fig. 9. Also reported in Fig. 9 are measurements of the normalized relative diaelastic modulus changes in the C_{44} mode following annealing at successively higher temperatures. For completeness, Johnson's diaelastic measurements were adjusted somewhat for damage concentration and also plotted in the figure.

In summary, the additional results have allowed some refinements to be made on the values reported by Johnson, but the essential problem of identifying the defect configurations that give rise to the paraelastic and diaelastic effects in Al-Mn still remains.

C. Al-Fe Results

Measurements of the logarithmic decrement before and after irradiation, for 10 MHz and 30 MHz, and for both the C' and C_{44} acoustic modes are presented in Fig. 10. No corrections for damage concentration or background shifts have been applied. The steeply sloping background from 10K to 60K provides a sensitive measure of the sample conductivity. After irradiation, the change in the background due to the reduction in conductivity by the radiation-induced defects is evident especially at the lowest temperatures. The steeply sloping background, however, made it difficult to extract the decrement for relaxation peaks between

Figure 9. Annealing of Al-Mn resistivity and relative diaelastic modulus change per unit concentration F.P. [C', C_{11}, B data from Johnson[1/]]

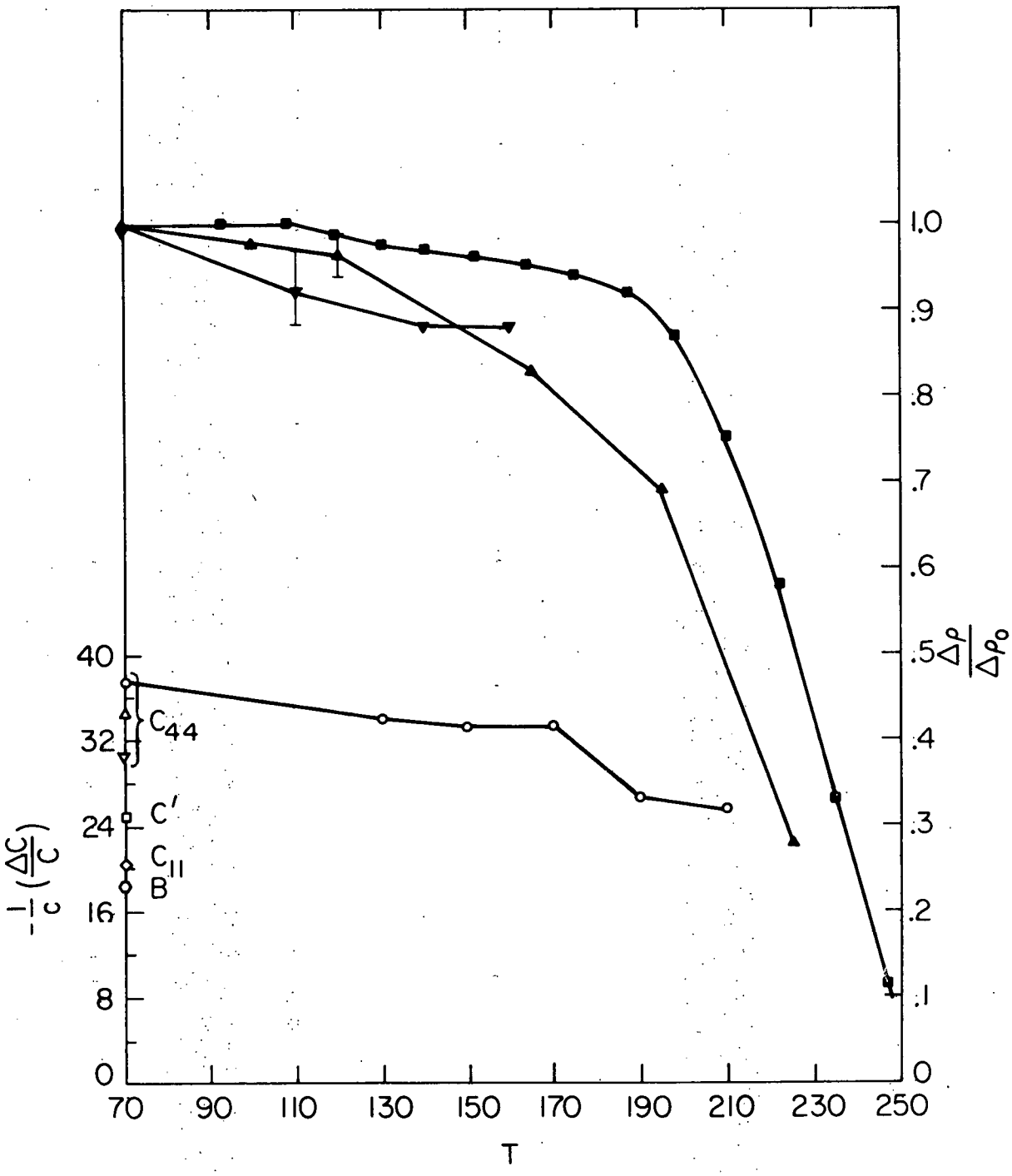
40
32
24
16
8
0
C_{44}
C′
C_{11}
B
$-\frac{1}{c}\left(\frac{\Delta c}{c}\right)$
1.0
.9
.8
.7
.6
.5
.4
.3
.2
.1
0
$\frac{\Delta\rho}{\Delta\rho_0}$
70
90
110
130
150
170
190
210
230
250
T

Figure 10. The measured decrement for Al-Fe at 10 and 30 MHz for the C_{44} and C' modes. Dashed line is before irradiation; solid line, after.

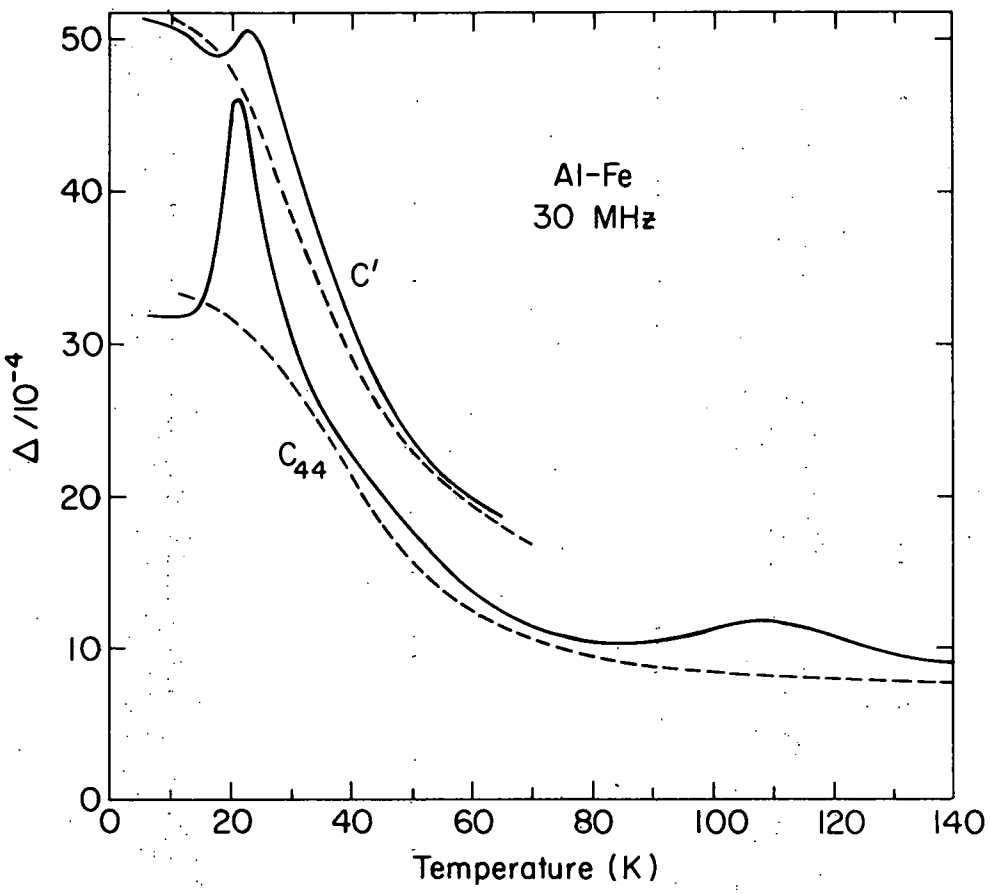
Al-Fe
30 MHz
C′
C44
Δ/10-4
Temperature (K)
0
10
20
30
40
50
0
20
40
60
80
100
120
140

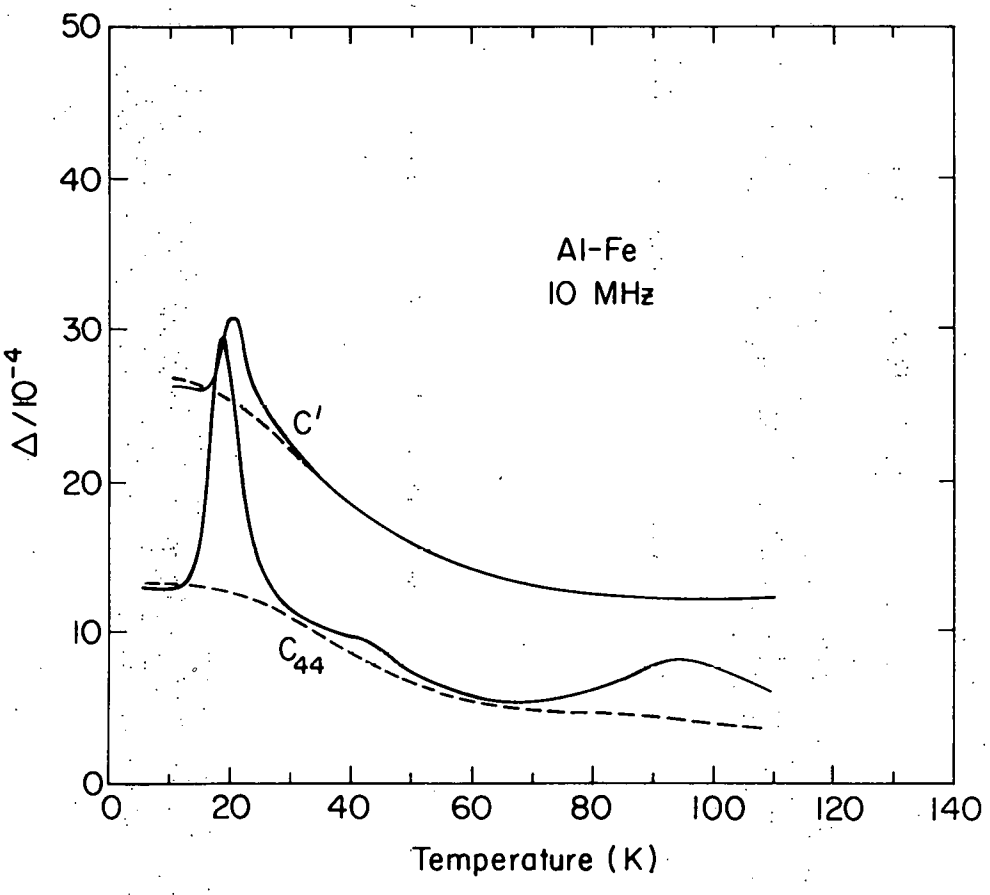
Al-Fe
10 MHz
C′
C44
Δ/10-4
Temperature (K)
0
10
20
30
40
50
0
20
40
60
80
100
120
140

20K and 60K. Three peaks are clearly discernable in the C_{44} mode near 19K, 42K, and 95K at 10 MHz. One peak appears in the C' mode near 21K at 10 MHz.

In Fig. 11, the background decrement has been subtracted off and the damage concentration has been normalized to 5 ppm F.P. In the figure, decrement peaks observed in the present work are shown along with the C_{44} mode results of Rehn, et al.[19] The peaks observed in the present work are labeled 1a, 1b, 1c, 2, and 4 as in the figure and in accordance with the labeling scheme of Rehn, et al. The C' peak, 1c, was not discernable in the torsion pendulum measurements. Also, peak 1a, which was first observed in the C_{44} mode after 170K annealing, was not detected by Rehn, et al. Peaks 3 and 5 reported by Rehn, et al. were not detected in the ultrasonic measurements.

In Table V, the Al-Fe peak characteristics obtained from 10 MHz ultrasonic measurements and from Rehn et al. are summarized.

The large temperature shift between corresponding attenuation peaks observed by the two techniques arises from the large difference in excitation frequencies. Using Eq. 10 and Eq. 12 and the peak temperatures from the torsion pendulum and ultrasonic measurement, accurate values of activation energy and frequency factor can be determined. Also, the same parameters can be evaluated using temperature shift data from 10 MHz and 30 MHz attenuation. In Figs. 12, 13, and 14, the attenuation data are replotted in a form suggested by Nowick and Berry[40] that allows for an accurate determination of the temperature shift. In Table VI, the results are listed for three

Figure 11. The decrement in Al-Fe for the C' and C_{44} modes. The background has been subtracted and the damage concentration has been normalized to 5 ppm F.P.

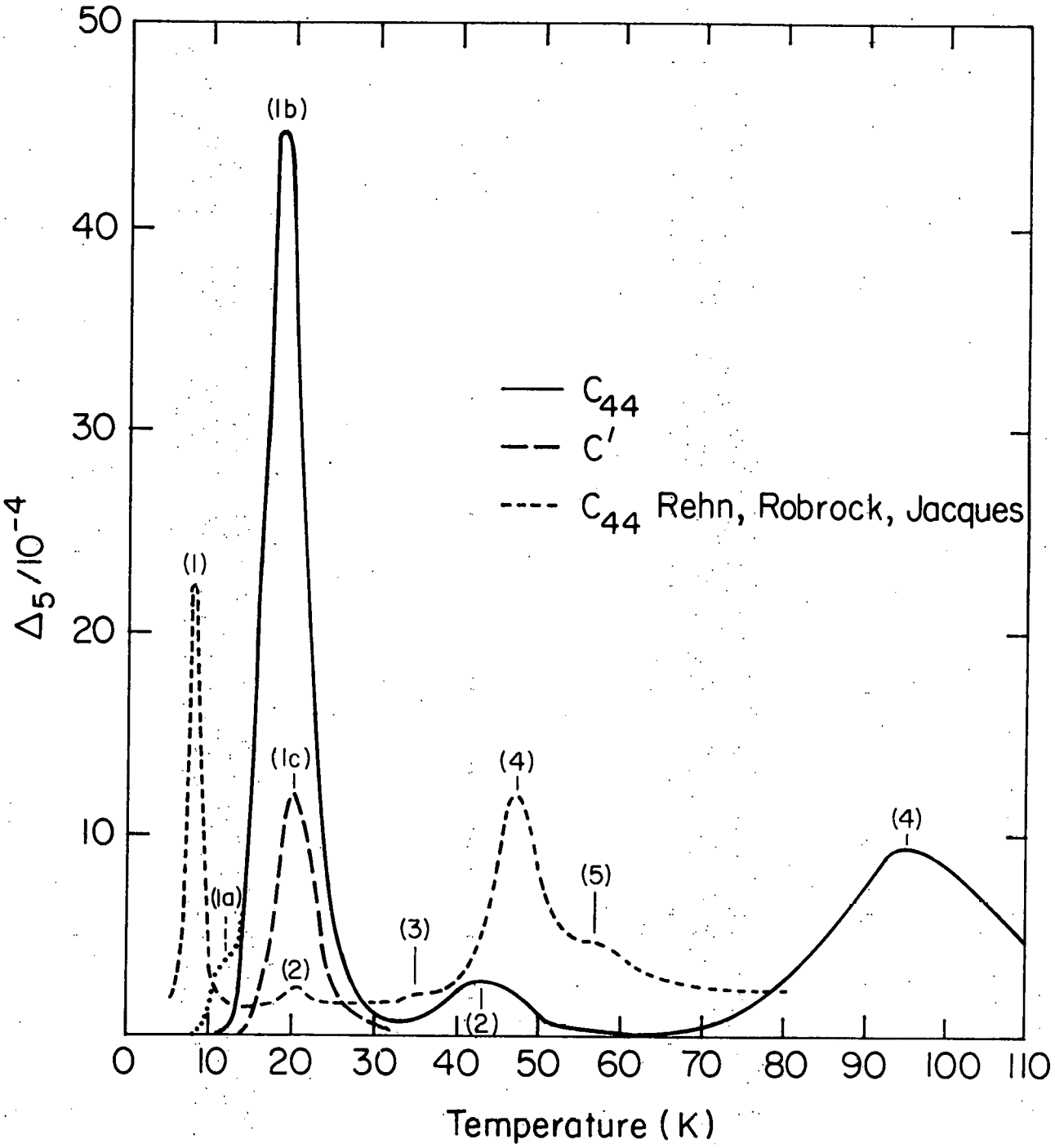
50
40
30
20
10
$\Delta_5/10^{-4}$
(1b)
(1)
(1a)
(1c)
(2)
(3)
(4)
(2)
(5)
(4)
C_{44}
C'
C_{44} Rehn, Robrock, Jacques
0
10
20
30
40
50
60
70
80
90
100
110
Temperature (K)

Figure 12. Al-Fe peak 1b shift with frequency. The decrement with background subtracted is normalized to 5 ppm F.P. and multiplied by temperature.

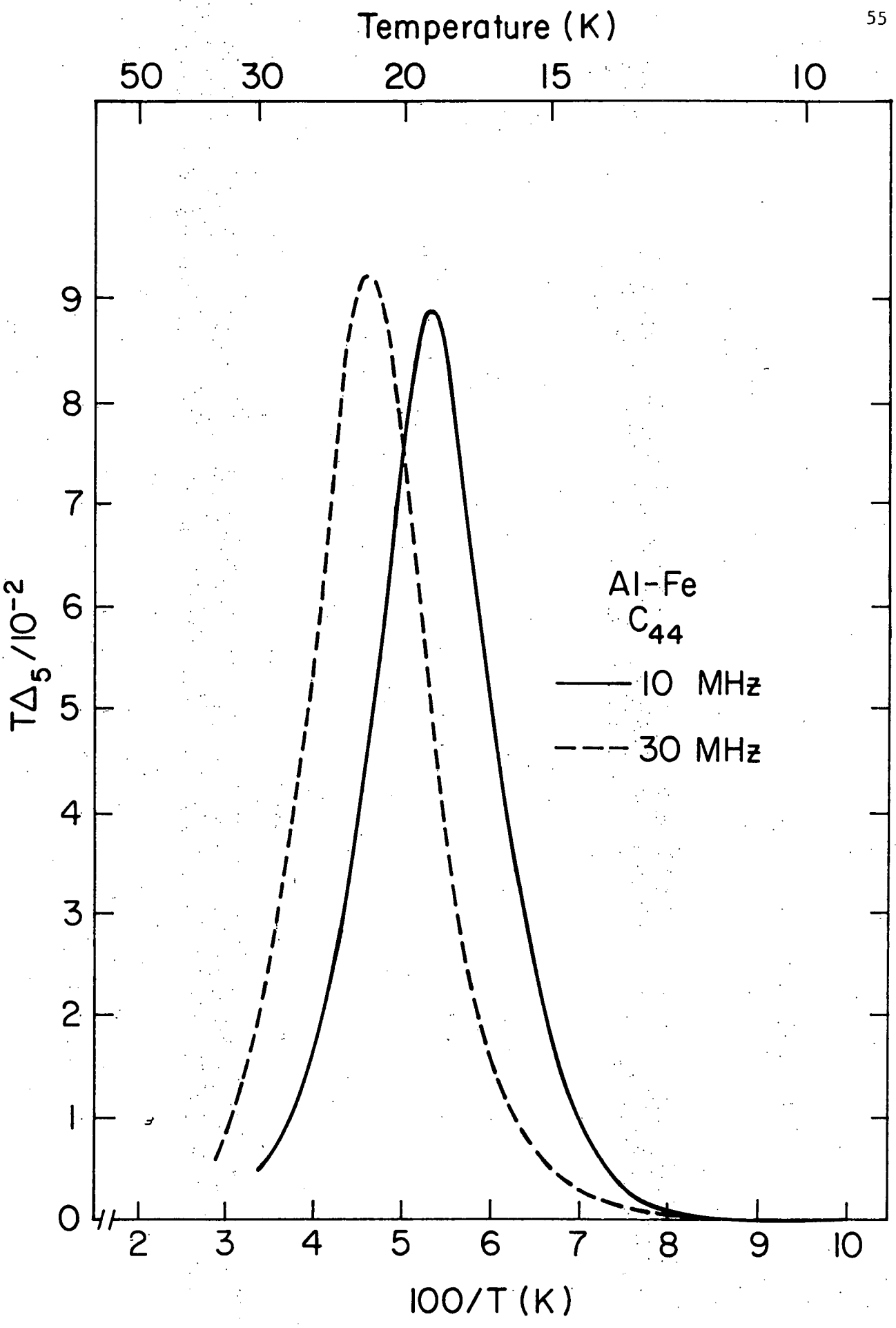
Temperature (K)
50
30
20
15
10
9
8
7
6
5
4
3
2
1
0
$T\Delta_5/10^{-2}$
Al-Fe
C_{44}
10 MHz
30 MHz
2
3
4
5
6
7
8
9
10
100/T (K)

Figure 13. Al-Fe peak 4 shift with frequency. The decrement with background subtracted is normalized to 5 ppm F.P. and multiplied by temperature.

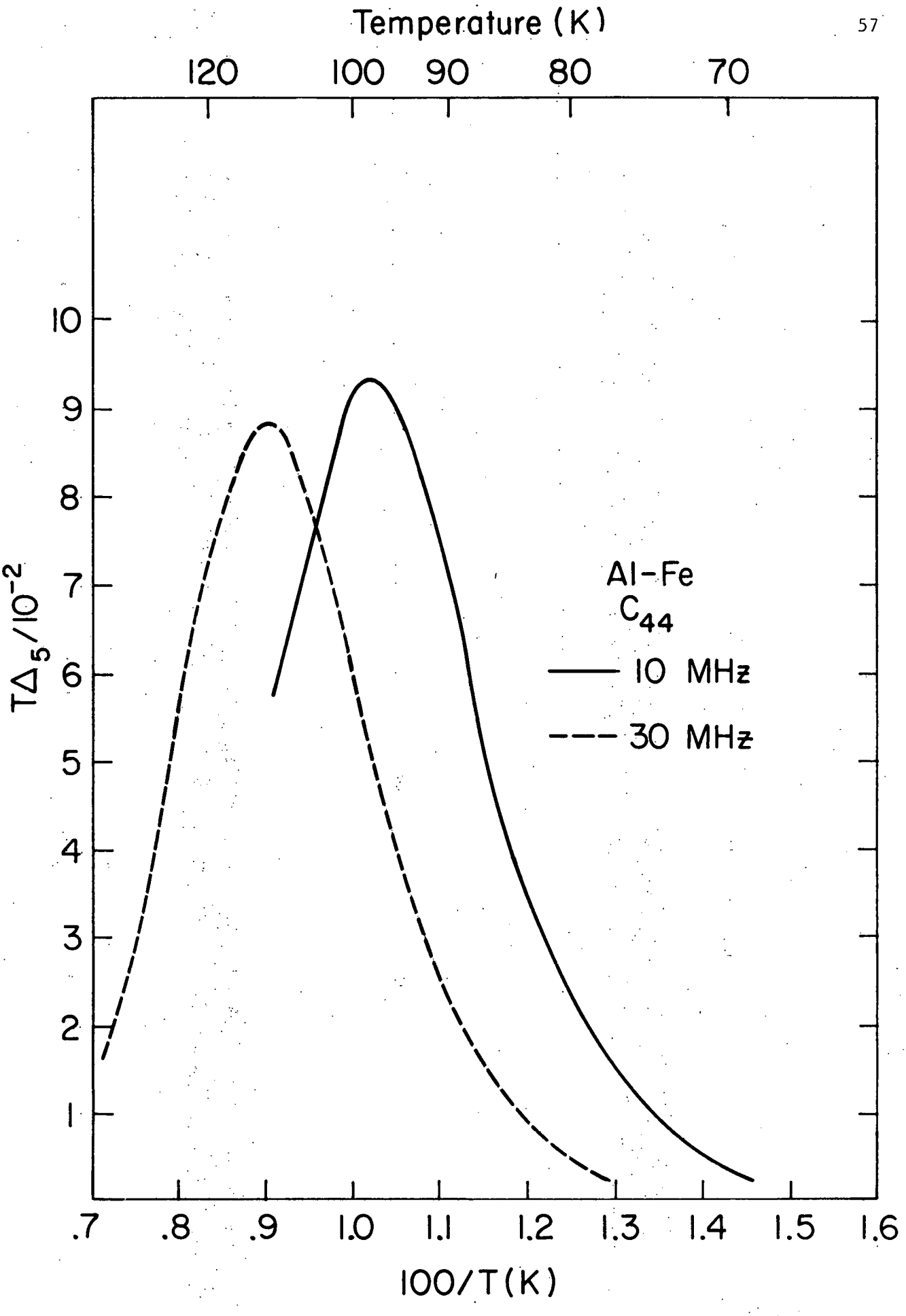
Temperature (K)
120
100
90
80
70
10
9
8
7
6
5
4
3
2
1
$T\Delta_5/10^{-2}$
Al-Fe
C_{44}
10 MHz
30 MHz
.7
.8
.9
1.0
1.1
1.2
1.3
1.4
1.5
1.6
100/T(K)

Figure 14. Al-Fe peak 1c shift with frequency. The decrement with background subtracted is normalized to 5 ppm F.P. and multiplied by temperature.

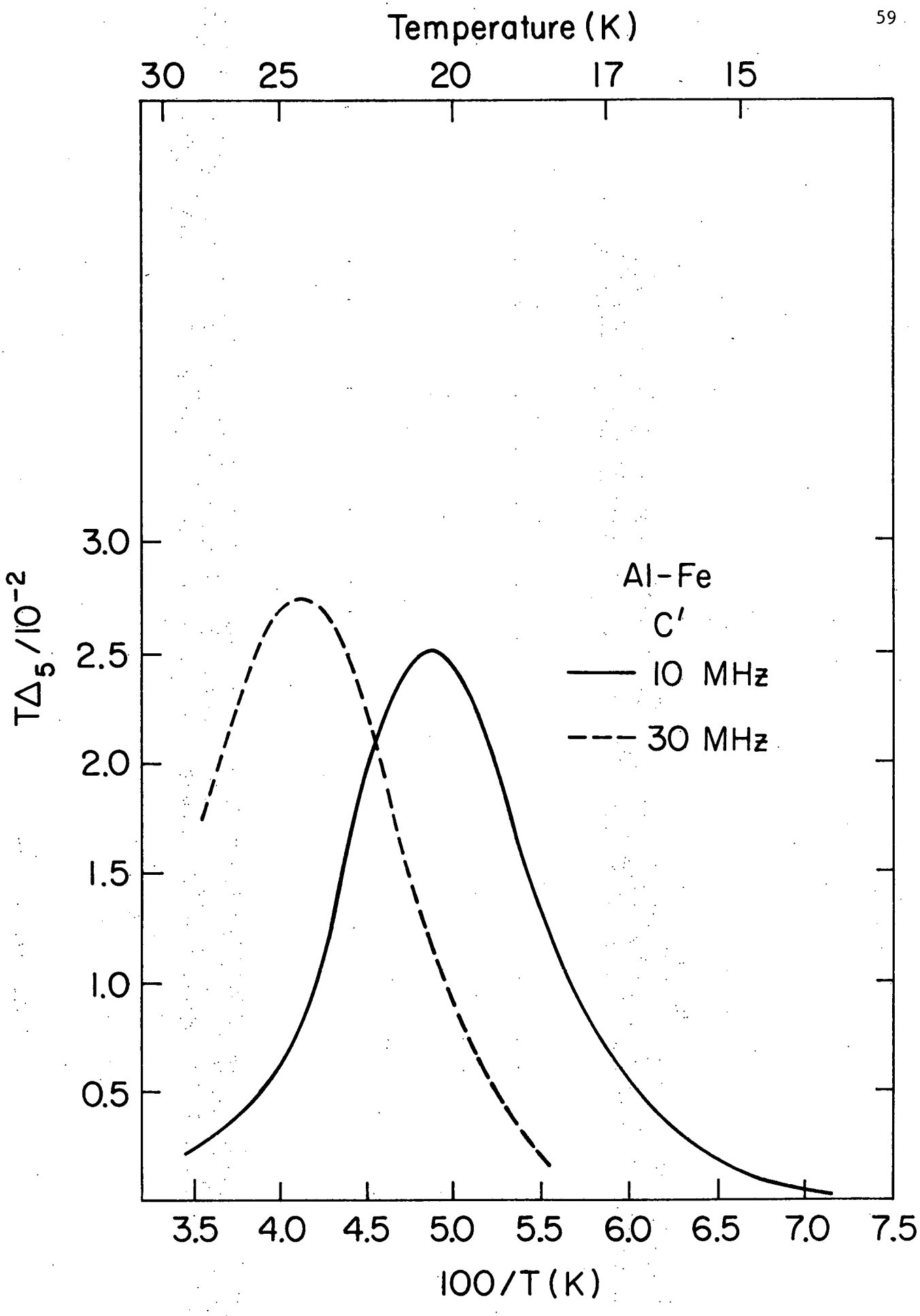
Temperature (K)
30
25
20
17
15
3.0
2.5
2.0
1.5
1.0
0.5
$T\Delta_5/10^{-2}$
Al-Fe
C′
10 MHz
30 MHz
3.5
4.0
4.5
5.0
5.5
6.0
6.5
7.0
7.5
100/T (K)

Table V. Al-Fe peak characteristics

Peak Number	T_m (25.2 Hz)	T_m (10 MHz)	Δ_m/C (25.2 Hz)	Δ_m/C (10 MHz)	$RT_m x10^{-3}$ (25.2 Hz)	$RT_m x10^{-3}$ (10 MHz)
1a	--	12K	--	71	--	1.7
1b	8.0K	18.7K	390	924	3.12	34.6
1c	--	20.5K	--	258	--	10.6
2	19.5K	43.5K	23	66	0.45	5.7
3	32.0K	--	45	--	1.4	--
4	42.5K	97.4K	190	200	8.08	39.0

Table VI. Al-Fe activation energies and frequency factors

Number	H(meV) (25.2 Hz - 87.7 Hz)	$\nu_0(S^{-1})$	H(meV) (10 MHz - 30 MHz)	$\nu_0(S^{-1})$	H(meV) (25.2 Hz - 10 MHz)	$\nu_0(S^{-1})$
1b	13 ± 4	$5x10^{10\pm3}$	13 ± 2	$10^{11.3\pm.5}$	15.5 ± 1.5	$10^{12.0\pm.4}$
1c	---	---	13.5 ± 4	$10^{11.1\pm1}$	---	---
2	29 ± 6	$1x10^{10\pm2}$	---	---	39 ± 2	$10^{12.3\pm.3}$
3	59 ± 12	$1x10^{11\pm2}$	---	---	---	---
4	82 ± 12	$1x10^{12\pm2}$	80 ± 3	$10^{11.9\pm.2}$	84 ± 2	$10^{12.1\pm.1}$

determinations of the peak activation parameters. The low frequency data are from Rehn, et al.

An examination of the errors reported in Table VI clearly shows that the ultrasonic data provide a superior measure of the frequency

factors. The improvement is inherent with measurements that are made at frequencies closer to ν_0. Some improvement is also reported in the ultrasonic determinations of H. That improvement results mainly from better measurements of the temperature shifts of the peaks with frequency.

The annealing of peaks 1a and 1b is shown in Fig. 15. The increase in the electrical conductivity background attenuation as the defects anneal out is evident at low temperature. The sudden appearance of peak 1a after the 180K anneal point is interesting. However, the growth of the peak could not be correlated with the disappearance of any other peak or with any changes in the electrical resistivity.

Fig. 16 shows the annealing of peaks 2 and 4 with the steeply sloping background subtracted off. Peak 1c annealing data is presented in Fig. 17. The pre-irradiation background, again, has been subtracted off, but no correction was made for the change in the conductivity with irradiation.

The annealing data for all of the peaks observed ultrasonically and for an electrical resistivity sample are summarized in Fig. 18. The curves show the normalized magnitude of each peak after a 10 min. anneal at the indicated temperatures. The significance of the difference in annealing of the various peaks near 220K is in doubt. Due to the large heat capacity of the sample holder and cryostat, systematic temperature errors of about 3K resulted from differential heating. Therefore, the annealing behavior can be summarized by saying that all of the relaxation peaks anneal out in stage III, and probably simultaneously. No changes

Figure 15. Annealing of Al-Fe peaks 1a and 1b.

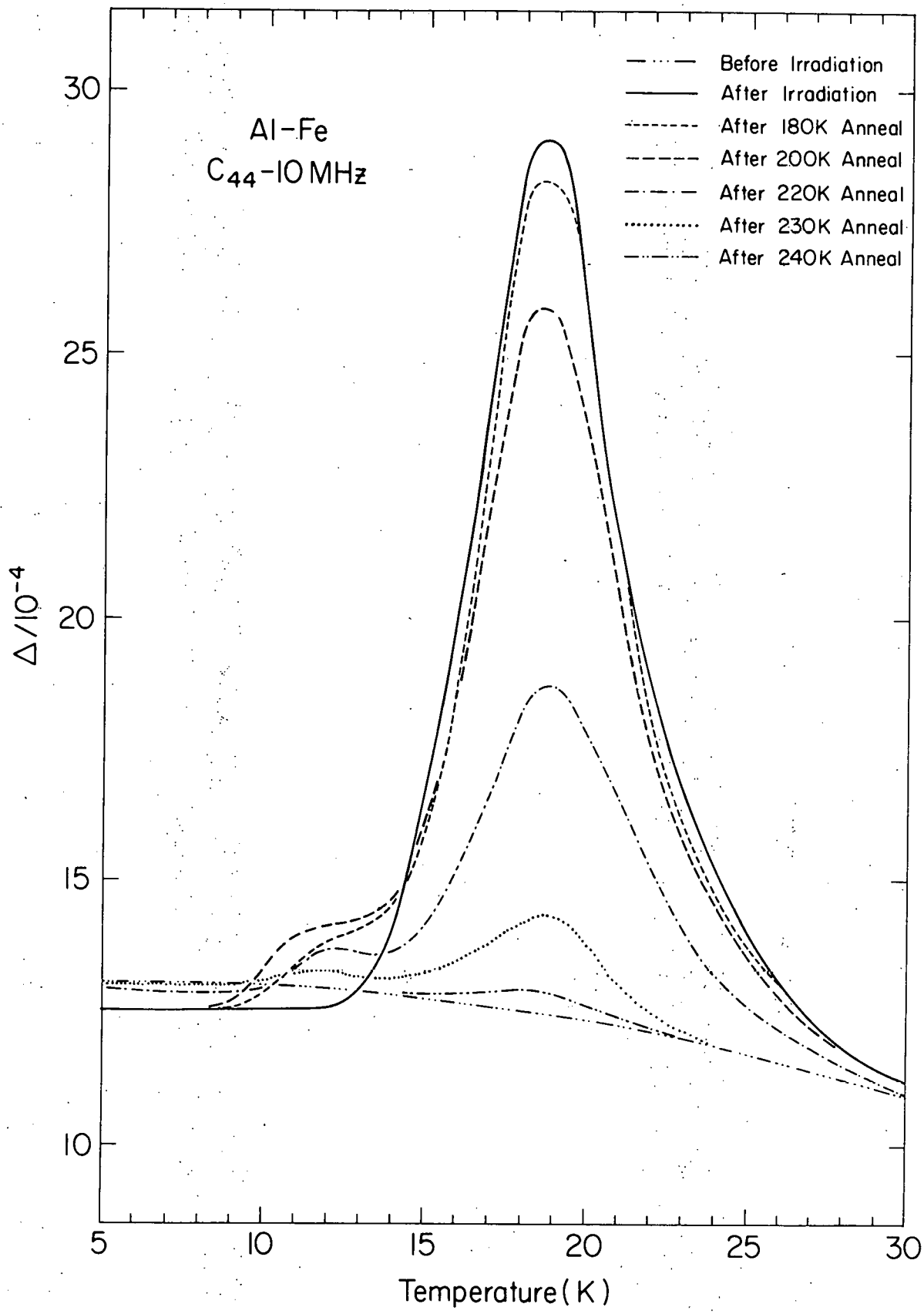
Al-Fe
C_{44}-10 MHz
Before Irradiation
After Irradiation
After 180K Anneal
After 200K Anneal
After 220K Anneal
After 230K Anneal
After 240K Anneal
Δ/10⁻⁴
30
25
20
15
10
5
10
15
20
25
30
Temperature (K)

Figure 16. The annealing of Al-Fe peaks 2 and 4. The background has been subtracted.

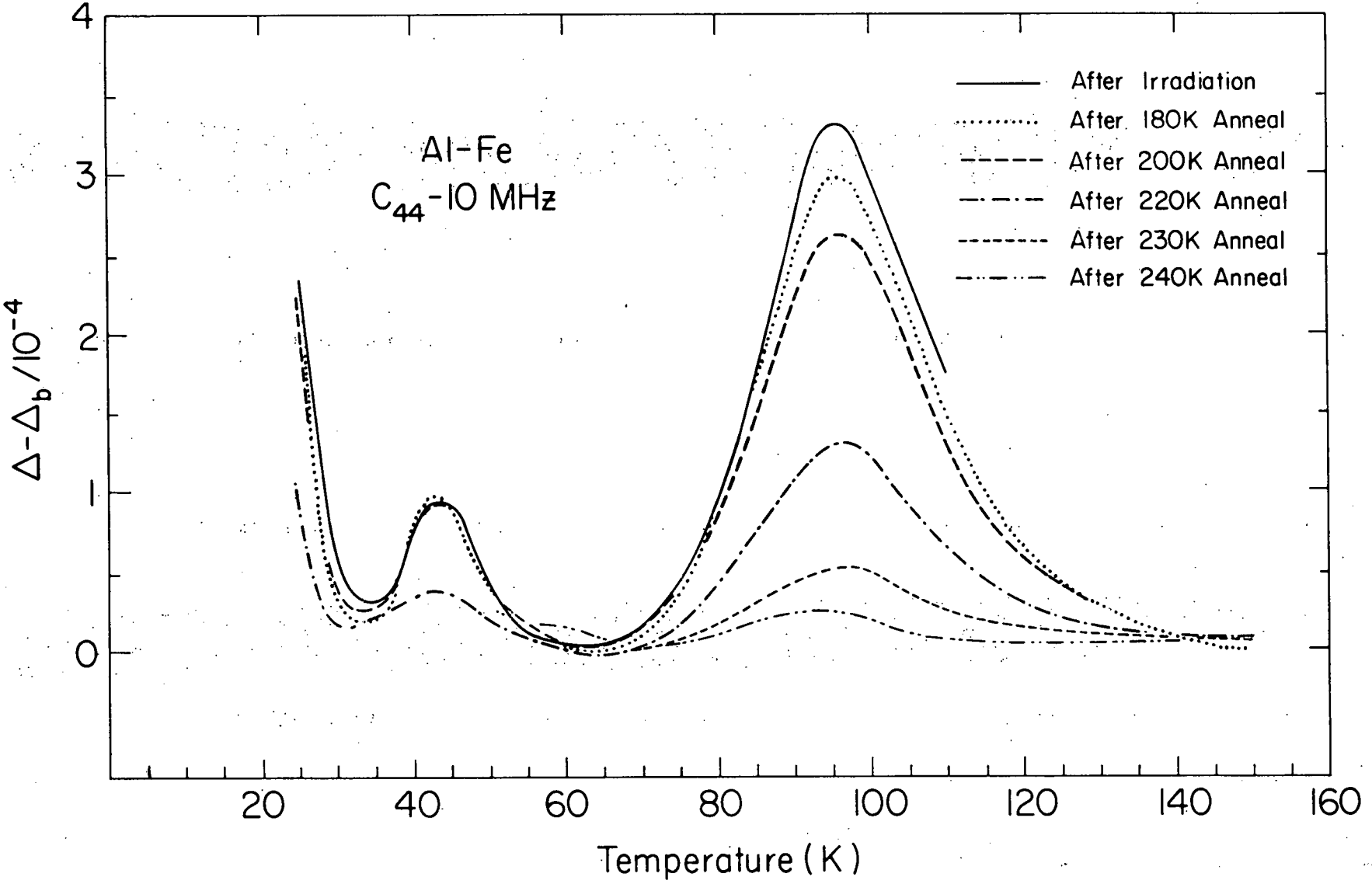
Al-Fe
C_{44}-10 MHz
After Irradiation
After 180K Anneal
After 200K Anneal
After 220K Anneal
After 230K Anneal
After 240K Anneal
$\Delta-\Delta_b/10^{-4}$
Temperature (K)
0
1
2
3
4
20
40
60
80
100
120
140
160

Figure 17. Annealing of Al-Fe peak 1c. The background has been subtracted.

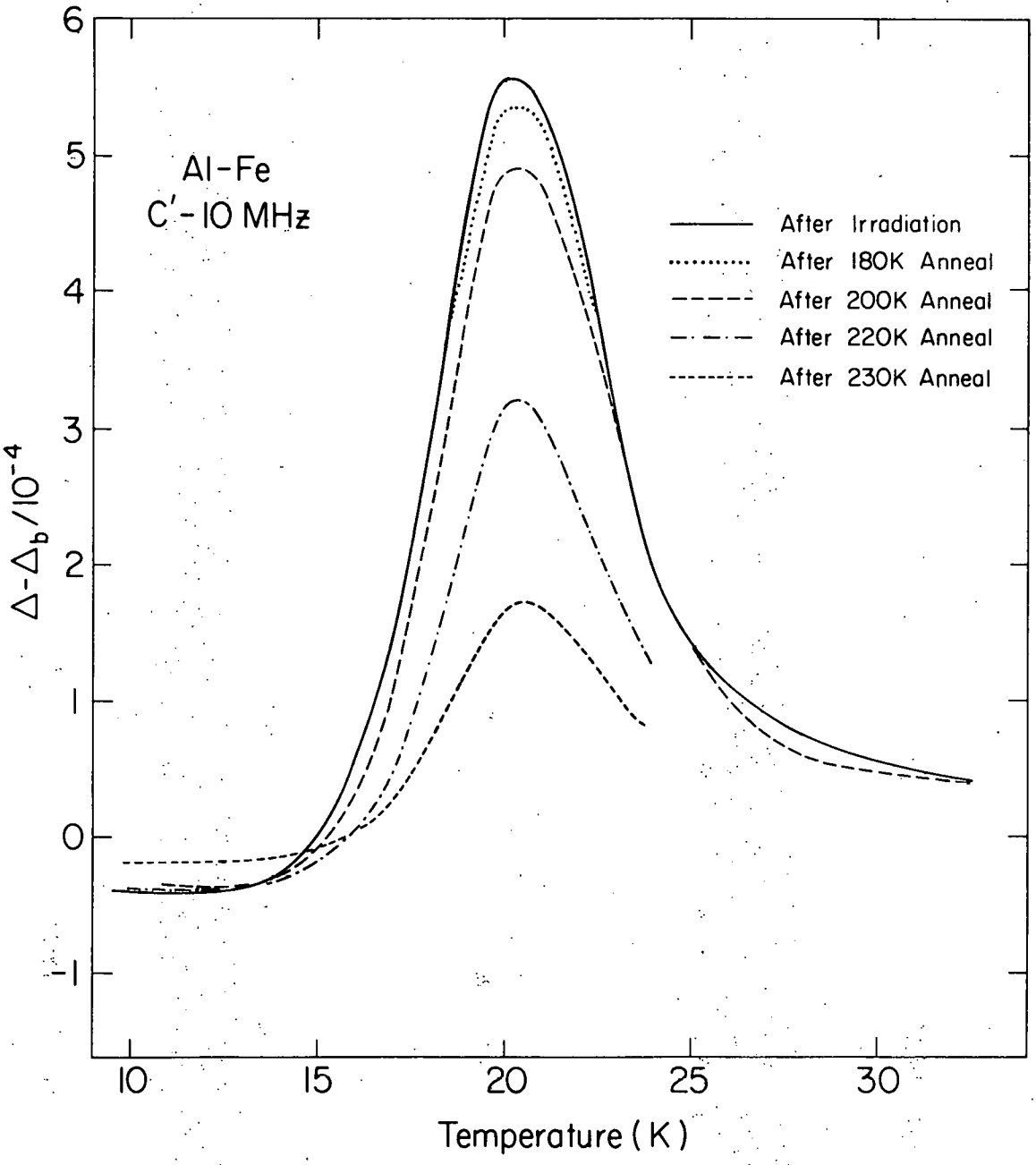
Al-Fe
C'-10 MHz
After Irradiation
After 180K Anneal
After 200K Anneal
After 220K Anneal
After 230K Anneal
Δ-Δb/10-4
Temperature (K)
6
5
4
3
2
1
0
-1
10
15
20
25
30

Figure 18. Al-Fe annealing summary. R is the relative value of each quantity to its post-irradiation value.

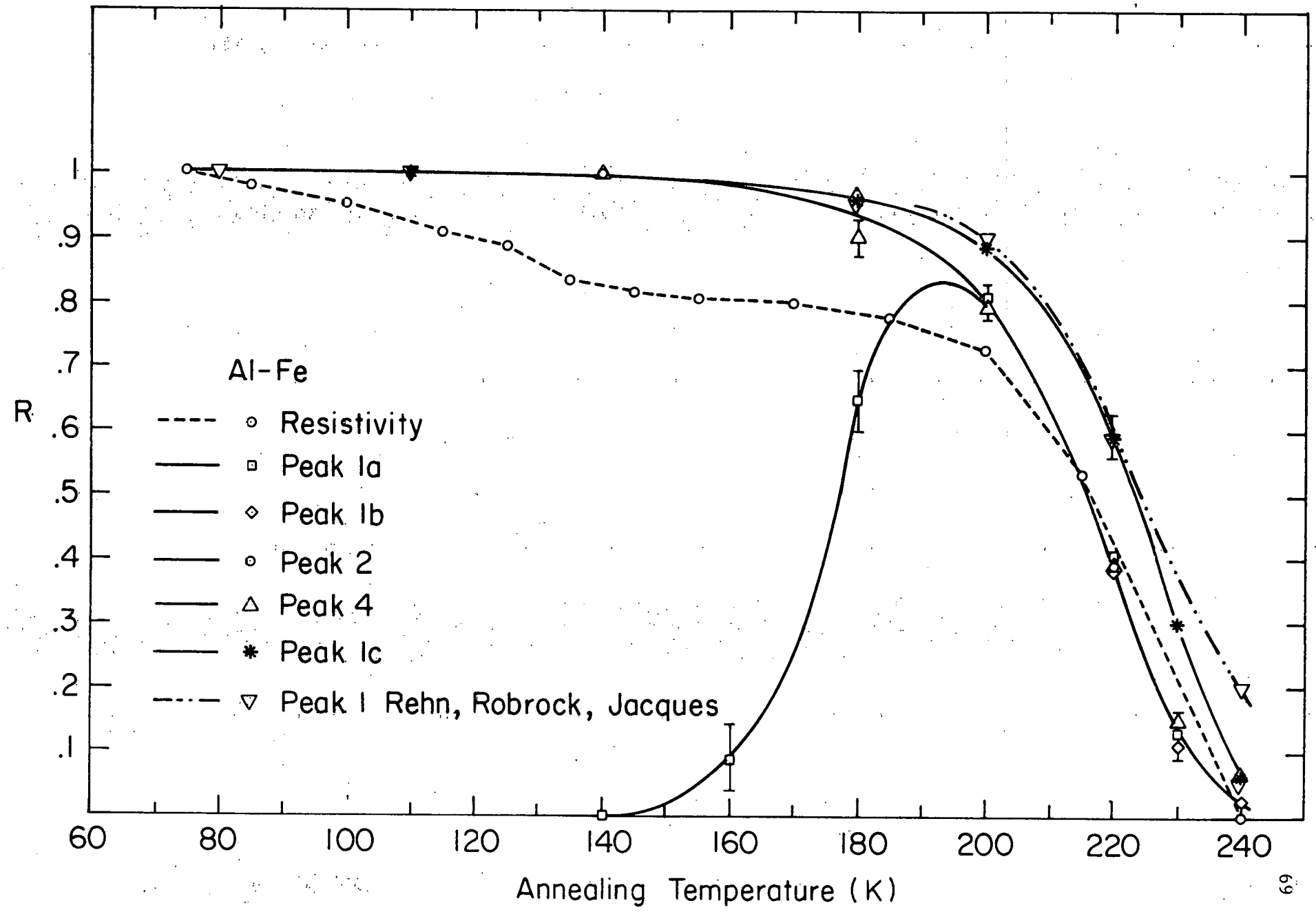
Al-Fe
Resistivity
Peak Ia
Peak Ib
Peak 2
Peak 4
Peak Ic
Peak I Rehn, Robrock, Jacques
R
1
.9
.8
.7
.6
.5
.4
.3
.2
.1
60
80
100
120
140
160
180
200
220
240
Annealing Temperature (K)

in the relaxation peaks were found to be associated with the significant resistivity annealing between 70K and 130K.

As indicated by the equations for a Debye relaxation, a paraelastic attenuation peak is accompanied by a dispersion in the elastic modulus. The frequency data in Fig. 19 clearly show the expected step-like behavior of the resonant frequency. The pre-irradiation background shown the normal temperature dependence of the modulus above 25K. After irradiation and in addition to the velocity dispersion, a large temperature-independent frequency drop is observed at low temperature that can be identified as the diaelastic effect.

In Fig. 20, the paraelastic frequency change has been obtained by subtracting off the pre-irradiation temperature-dependent background and the temperature-independent diaelastic frequency change evaluated at 5K. The resulting frequency change and attenuation peak fit the Debye form with a relaxation strength that varies inversely with temperature.

Finally, diaelastic resonant frequency change measurements are shown in Fig. 21 as a function of annealing temperature. The temperature independence of the frequency change is demonstrated by 5K and 10K measurements and shows that there are no relaxation peaks below 5K that were not detected in the attenuation measurements. The large effect observed in the C_{44} mode offers a clue to a possible understanding of the peaks in Al-Fe. Further discussion is deferred until part IV.

Figure 19. The measured resonant frequency of Al-Fe before and after irradiation. (f_0 = 11,000,000 Hz).

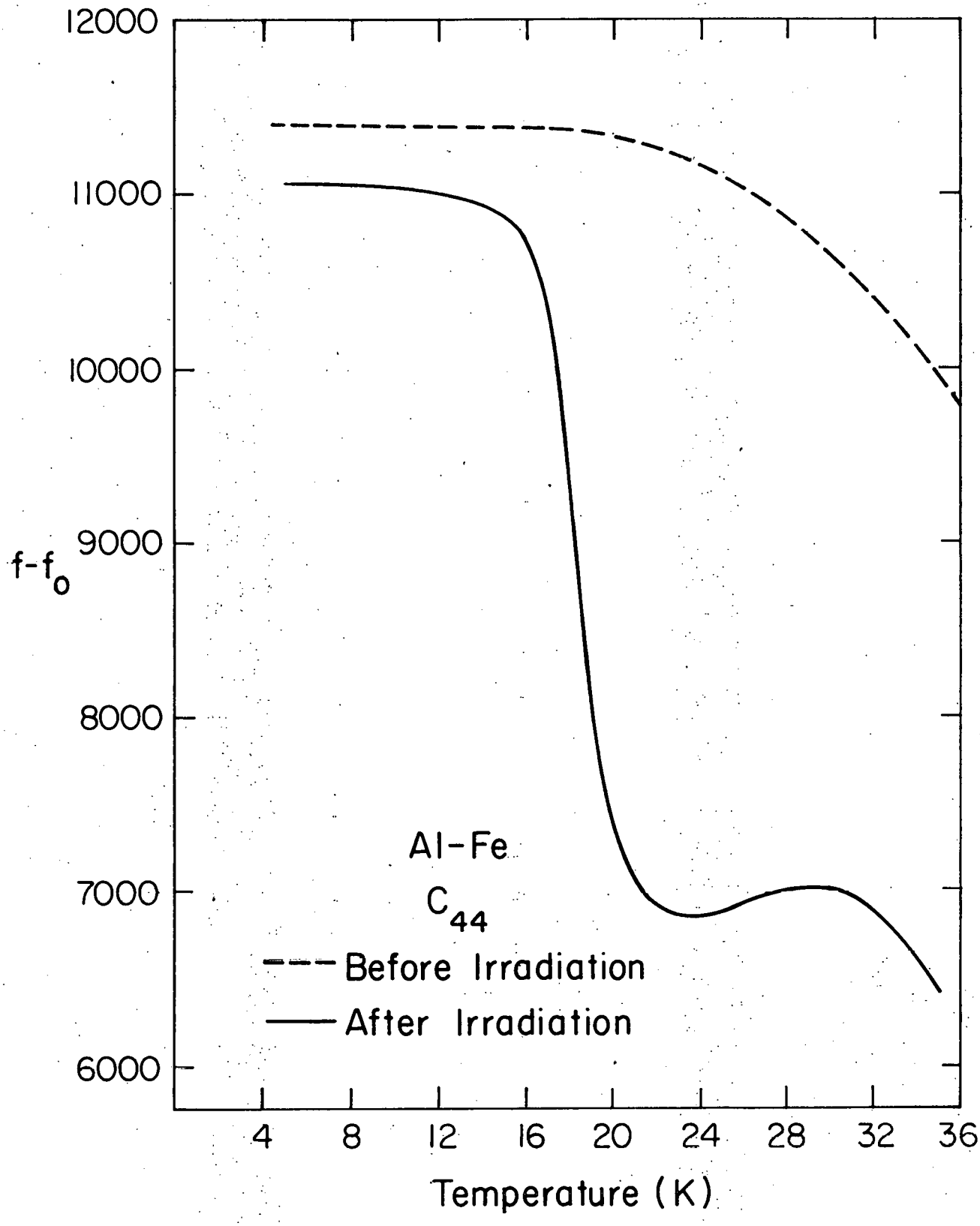
12000
11000
10000
9000
8000
7000
6000
f-f0
Al-Fe
C44
Before Irradiation
After Irradiation
4
8
12
16
20
24
28
32
36
Temperature (K)

Figure 20. Al-Fe peak 1b decrement with background subtracted (solid line) and the relative frequency change (dashed line).

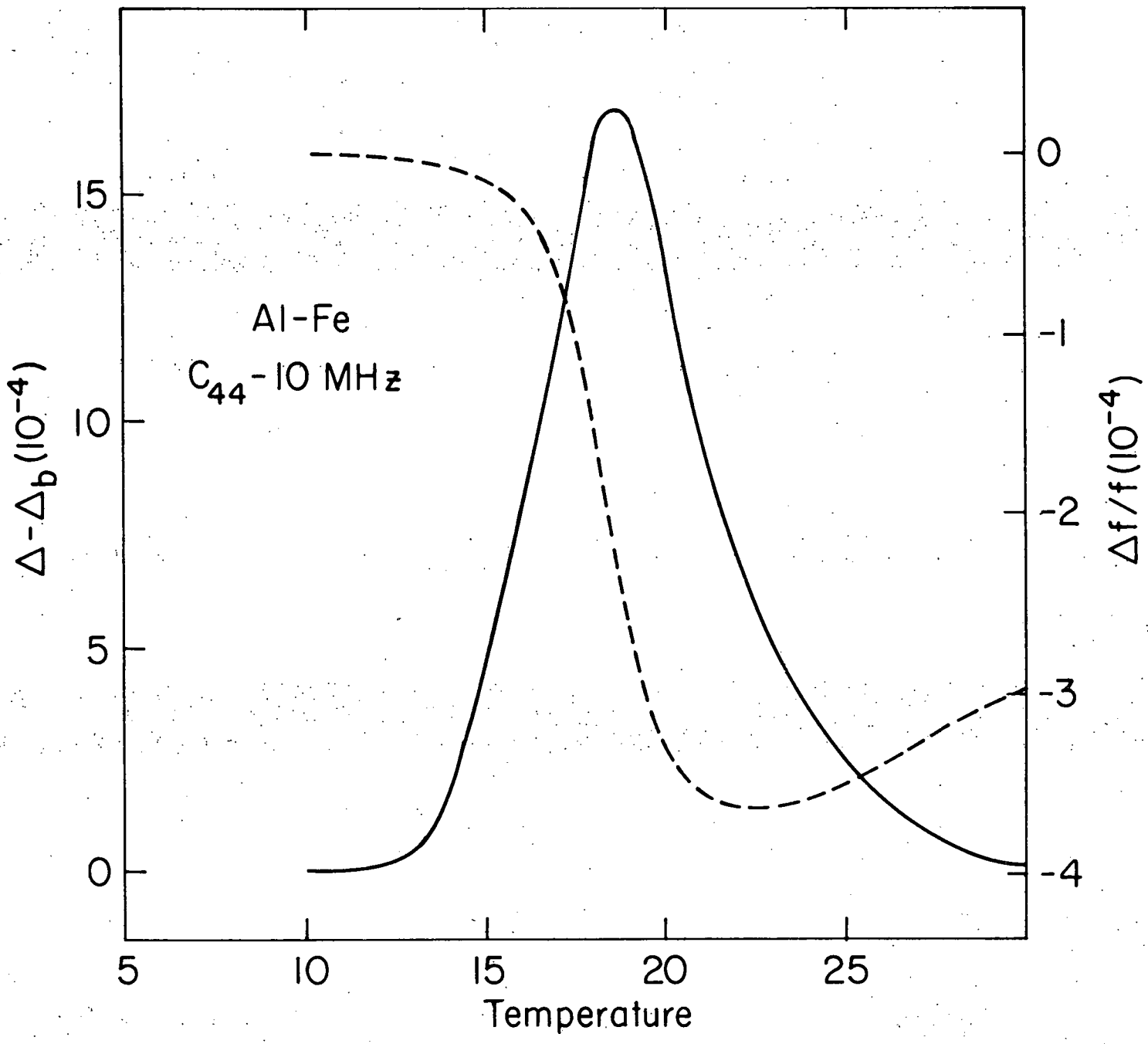
Al-Fe
C_{44} - 10 MHz
$\Delta - \Delta_b (10^{-4})$
$\Delta f/f (10^{-4})$
Temperature
0
5
10
15
-4
-3
-2
-1
0
5
10
15
20
25

Figure 21. Annealing of the Al-Fe frequency change for C' and C_{44} modes. f_b is the pre-irradiation resonsant frequency. Data taken at 5K and 10K.

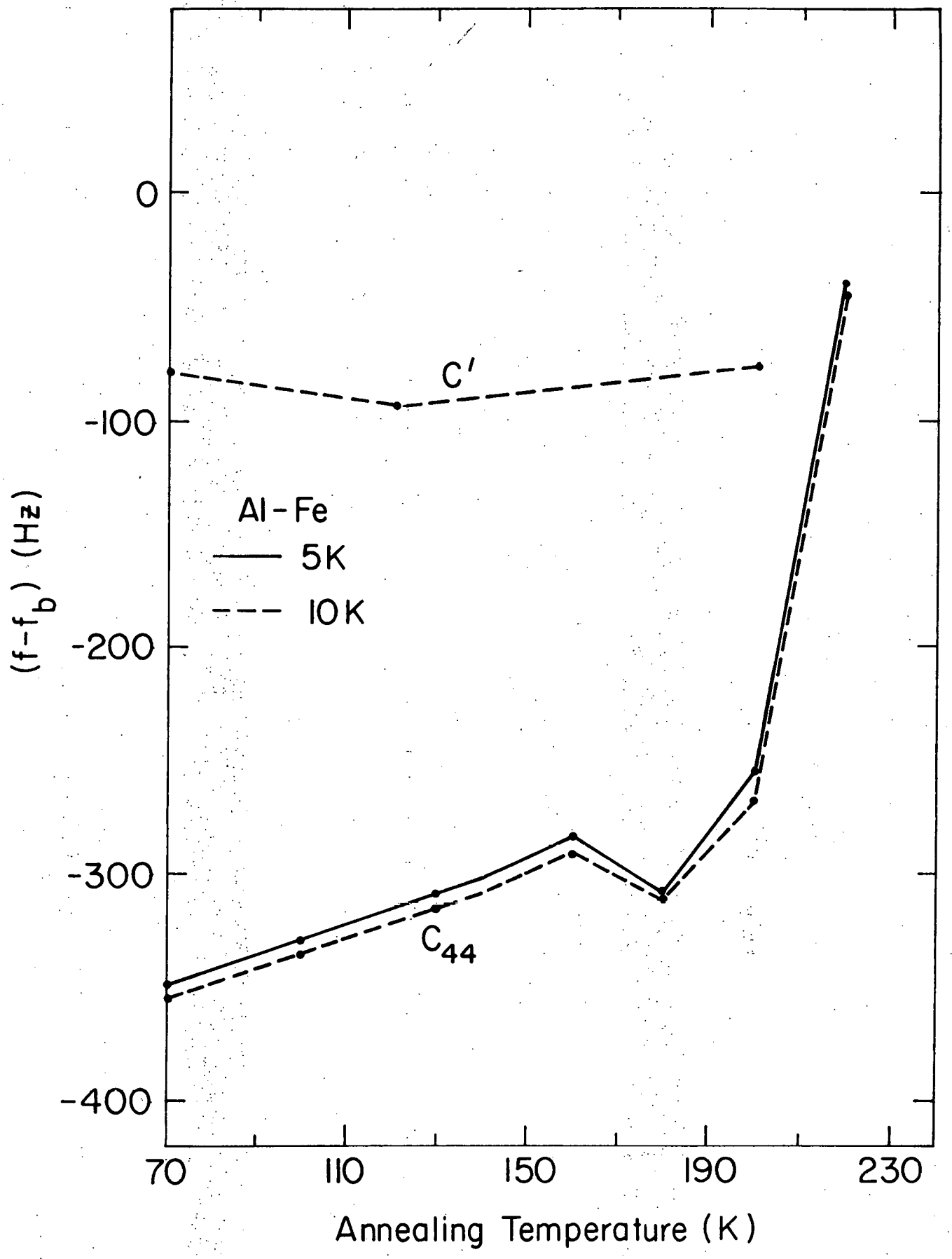
0
-100
-200
-300
-400
$(f-f_b)$ (Hz)
Al-Fe
5K
10K
C′
C_{44}
70
110
150
190
230
Annealing Temperature (K)

D. Al-Zn Results

Radiation-induced changes in ultrasonic velocity and attenuation were measured in two Al-Zn alloys. The attenuation data for a nominally .1 at. % alloy is shown in Fig. 22 for both the C_{44} and C' acoustic modes and for both 10 MHz and 30 MHz excitation frequencies. The large values of electronic attenuation observed in the background curves at 30 MHz were used to calibrate the acoustic method of determining conductivity. The large changes in the electronic attenuation following irradiation are especially evident here because the radiation-induced resistivity change is a large fraction of the total resistivity.

Two peaks in the attenuation are clearly discernable. One peak, near 5K at 10 MHz, appears in the C' mode and a second peak, near 100K at 10 MHz, appears in the C_{44} mode.

The same two peaks also appear in the measurements for a nominally .5 at. % alloy shown in Fig. 23. The irradiation temperature, however, had been reduced to about 55K for these measurements compared to about 70K for all of the earlier measurements. In these measurements a third attenuation peak is observed that disappears following a 75K anneal. The peak is characterized by a broad but very small attenuation from about 5K to about 40K.

Fig. 24 shows the large, non-classically shaped C' peak in Al-.1% Zn following successive 10 min. anneals at the indicated temperatures. A prominent feature is the unusual increase of attenuation at low temperatures. A superposition of two Debye peaks fails to fit the observed attenuation and, also, fails to predict the change in the

Figure 22. The measured decrement before (dashed line) and after (solid line) irradiation of Al-.1% Zn at 10 and 30 MHz for C' and C_{44} modes.

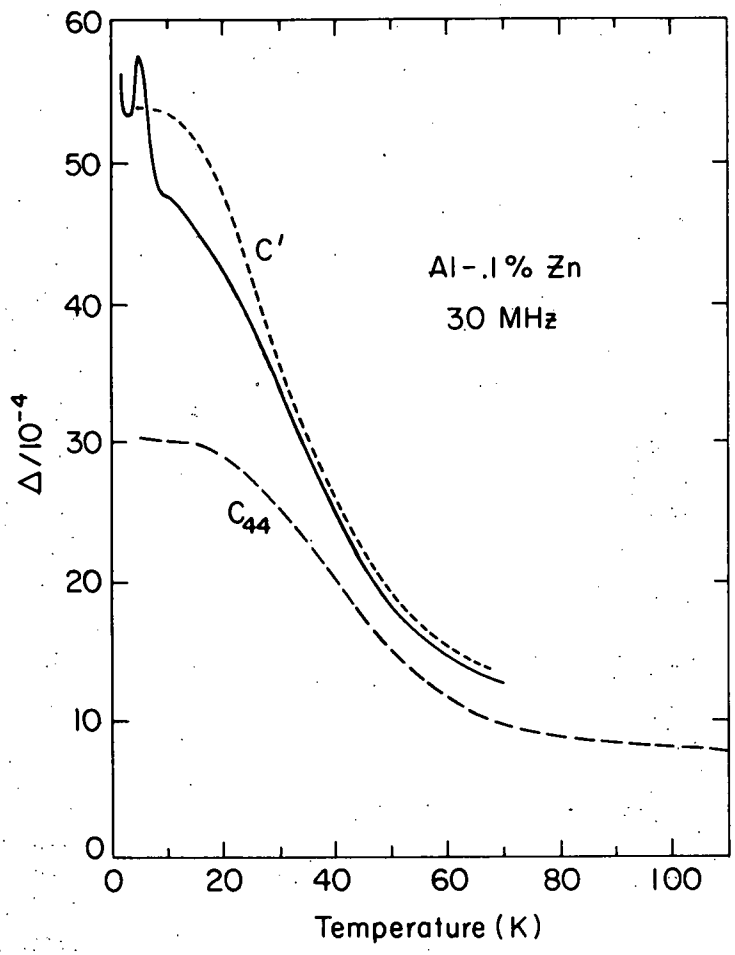
60
50
40
30
20
10
0
Δ/10⁻⁴
C′
C44
Al-.1% Zn
30 MHz
0
20
40
60
80
100
Temperature (K)

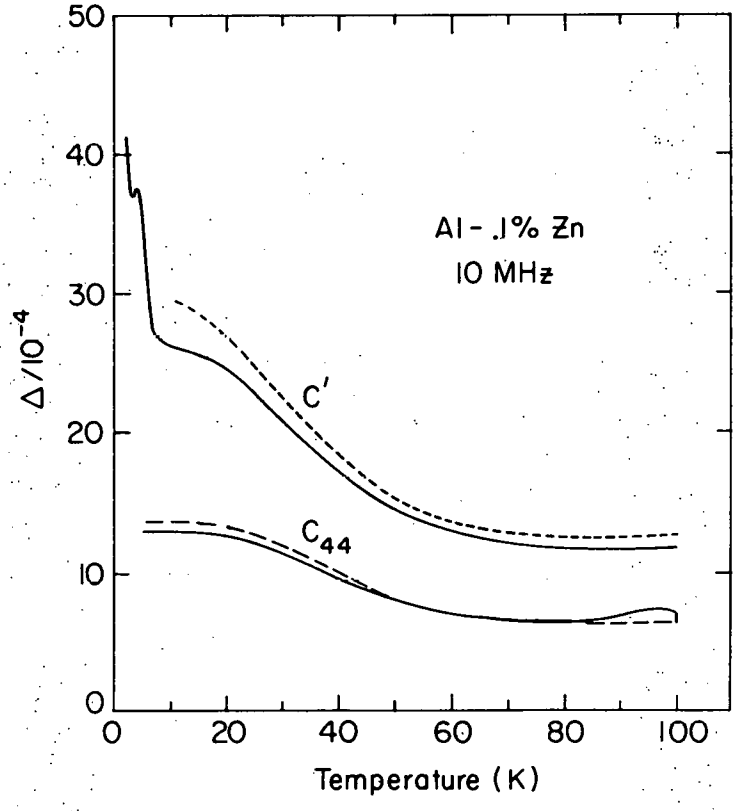
50
40
30
20
10
0
Δ/10⁻⁴
C′
C44
Al-.1% Zn
10 MHz
0
20
40
60
80
100
Temperature (K)

Figure 23. The measured decrement before (dashed line) and after (solid line) irradiation of Al-.5% Zn at 10 and 30 MHz for C' and C_{44} modes.

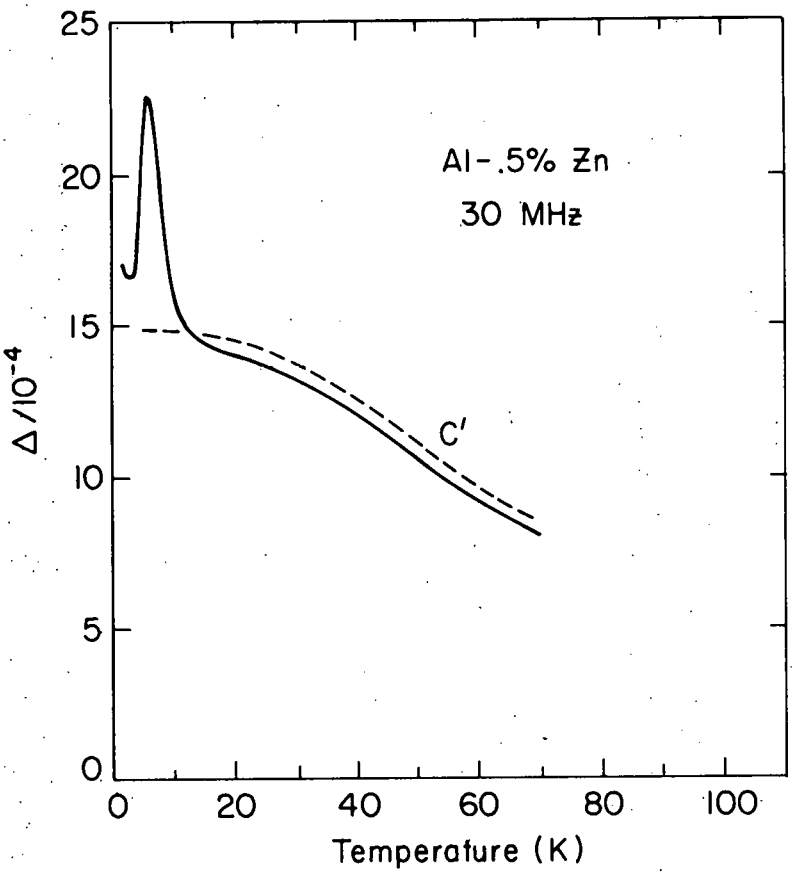
Al-.5% Zn
30 MHz
C′
Δ/10⁻⁴
Temperature (K)
0
5
10
15
20
25
0
20
40
60
80
100

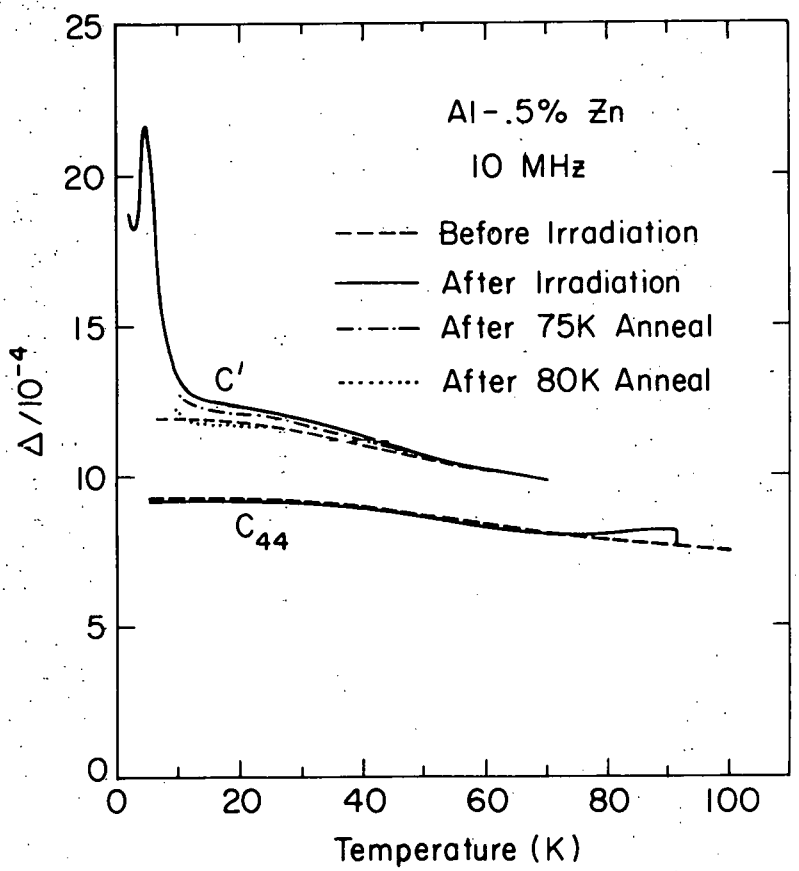
Al-.5% Zn
10 MHz
Before Irradiation
After Irradiation
After 75K Anneal
After 80K Anneal
C′
C44
Δ/10⁻⁴
Temperature (K)
0
5
10
15
20
25
0
20
40
60
80
100

Figure 24. Annealing of Al-.1% Zn peak 1.

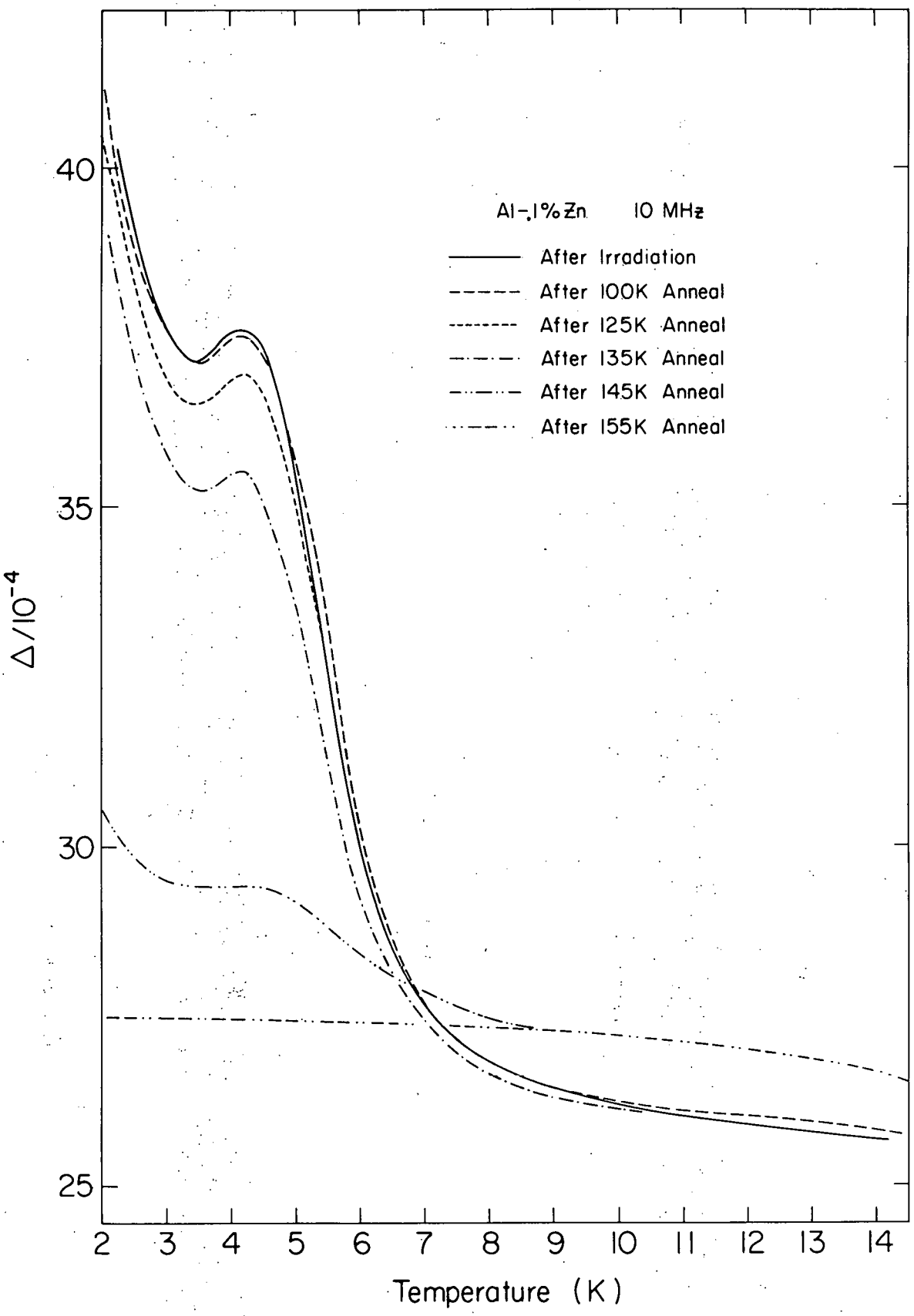
Al-.1%Zn 10 MHz
After Irradiation
After 100K Anneal
After 125K Anneal
After 135K Anneal
After 145K Anneal
After 155K Anneal
Δ/10⁻⁴
40
35
30
25
2
3
4
5
6
7
8
9
10
11
12
13
14
Temperature (K)

shape of the peak as observed at 30 MHz. The entire attenuation peak is observed to anneal out together indicating that a single defect species is involved. The corresponding data for Al-.5% Zn appear in Fig. 25. The distinct difference in the shape of the peak below 4K for the two alloys is interesting and will be discussed in detail later. The more complete annealing program results in Fig. 25 reveal a small new peak near 3K that grows in following a 140K anneal and that disappears in stage III.

The peak in C_{44} was observed to anneal out as it was being measured. Therefore, it was possible to perform isothermal annealing measurements. The results are shown in Figs. 26 and 27. In Fig. 26a, a pre-irradiation background curve is shown for Al-.1% Zn. The curve marked with arrows shows the attenuation that was measured while ramping up in temperature at 1 deg./min. immediately following irradiation. At 100K, the temperature ramp was halted, and the attenuation was observed to decrease almost to the background level during a 10-minute anneal. The time dependence of the drop toward the background value is presented on a semilog. plot in Fig. 27. The straight line fit indicates the process to be nearly exponential. Similar data is presented for the .5% alloy. In this case, an attempt was made to measure the binding energy and frequency factor by performing isothermal annealling measurements at three different temperatures. The time dependence of the three annealing curves is also shown in Fig. 27. Fig. 26b shows the attenuation measured in each alloy after irradiation and during the initial scan at 1 deg./min. over the peak. The background has been subtracted and the damage concentration has been normalized to 5 ppm F.P.

Figure 25. Annealing of Al-.5% Zn peak 1.

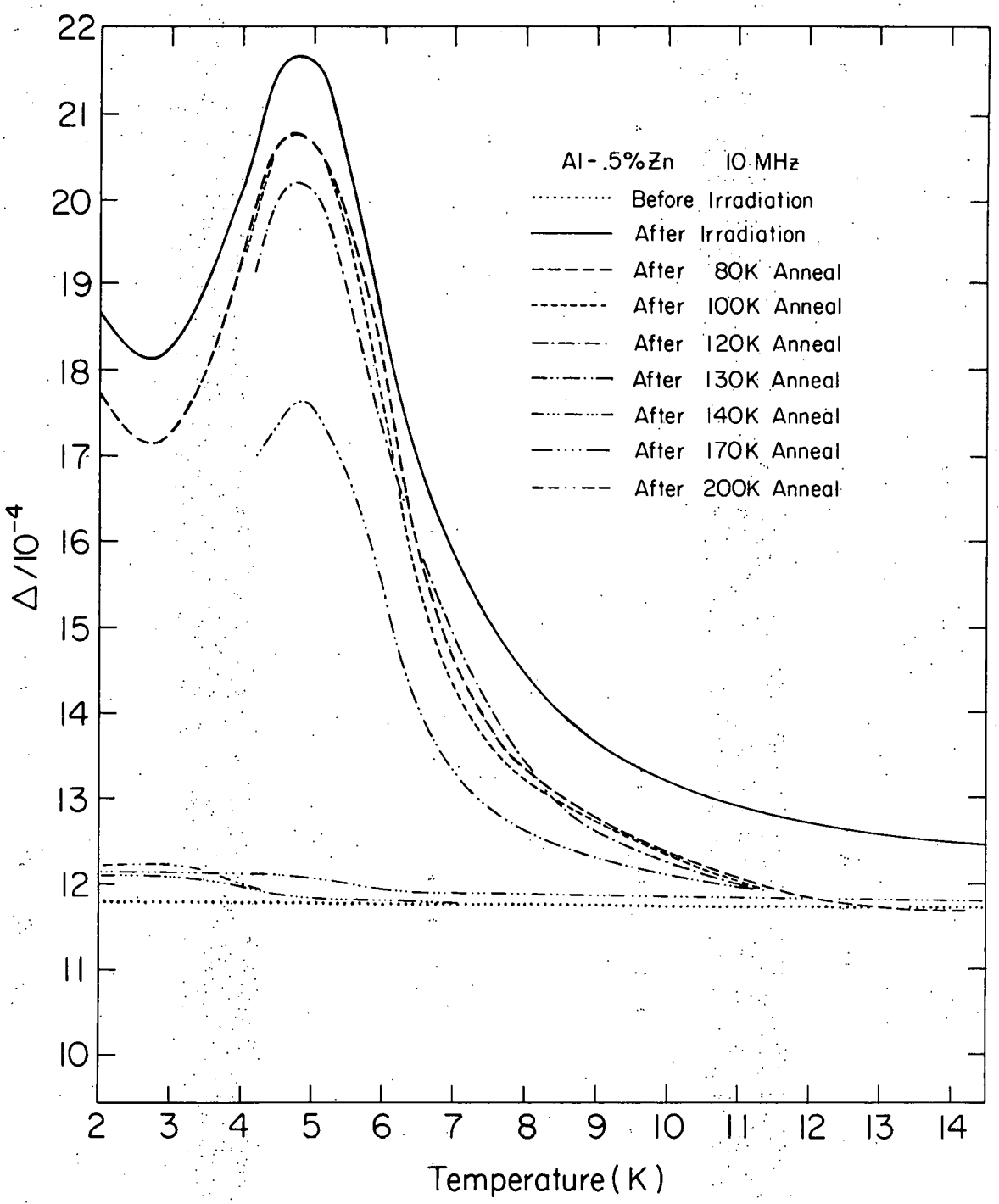
Al - .5% Zn 10 MHz
Before Irradiation
After Irradiation
After 80K Anneal
After 100K Anneal
After 120K Anneal
After 130K Anneal
After 140K Anneal
After 170K Anneal
After 200K Anneal
Δ/10⁻⁴
Temperature (K)
22
21
20
19
18
17
16
15
14
13
12
11
10
2
3
4
5
6
7
8
9
10
11
12
13
14

Figure 26. Al-Zn C_{44} decrement.

A. (top) Background decrement and decrement on first ramp up in temperature at 1 deg./min.

B. (bottom) Same with background subtracted and re-normalized to 5 ppm F.P.

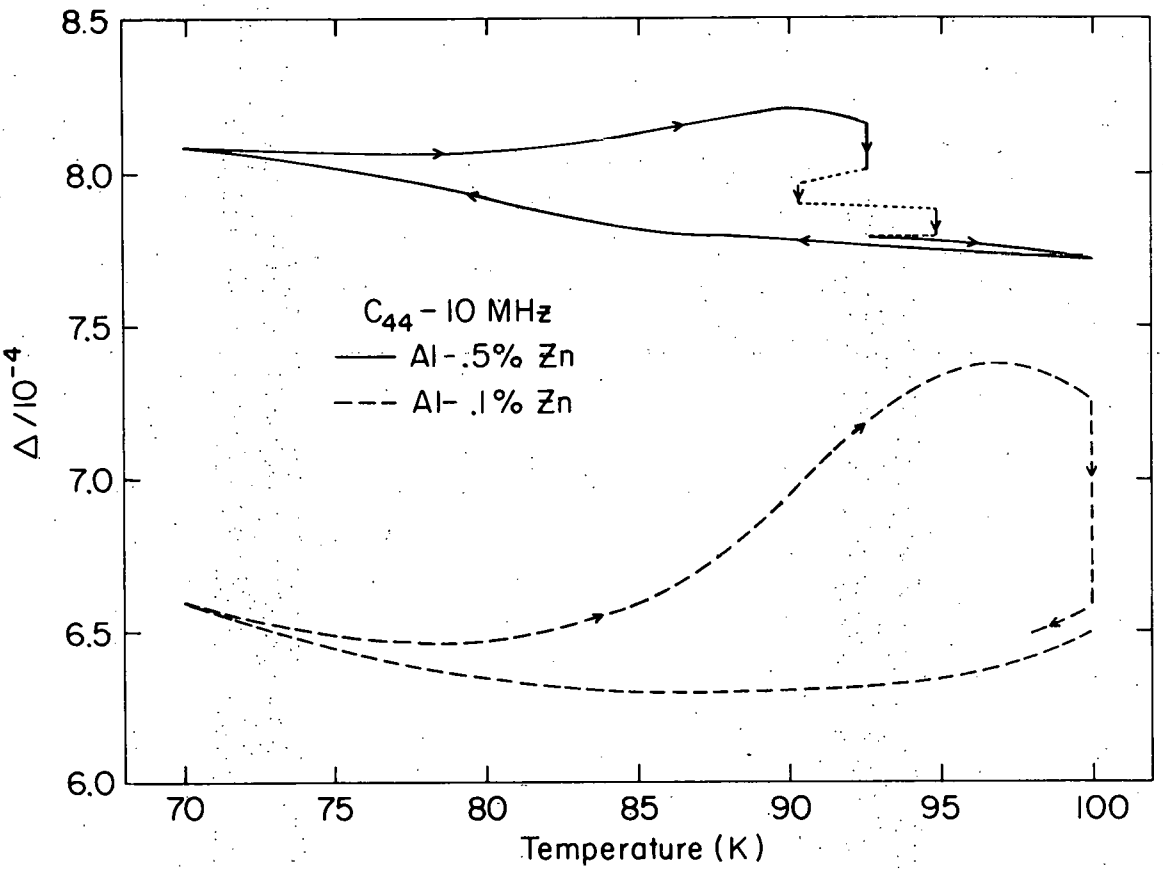
8.5
8.0
7.5
7.0
6.5
6.0
Δ /10⁻⁴
C44 – 10 MHz
Al-.5% Zn
Al-.1% Zn
70
75
80
85
90
95
100
Temperature (K)

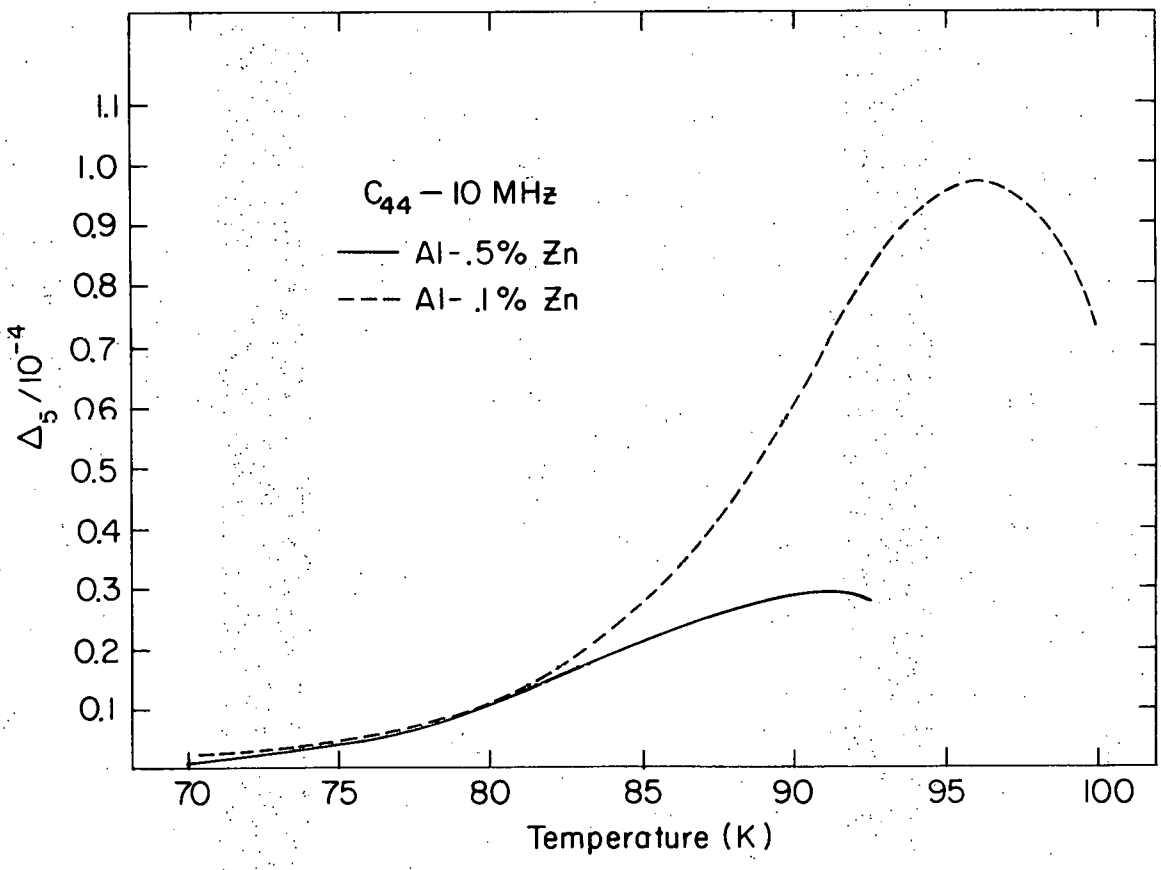
1.1
1.0
0.9
0.8
0.7
0.6
0.5
0.4
0.3
0.2
0.1
Δs /10⁻⁴
C44 – 10 MHz
Al-.5% Zn
Al-.1% Zn
70
75
80
85
90
95
100
Temperature (K)

Figure 27. Time dependence of isothermal annealing of Al-Zn C_{44} decrement.

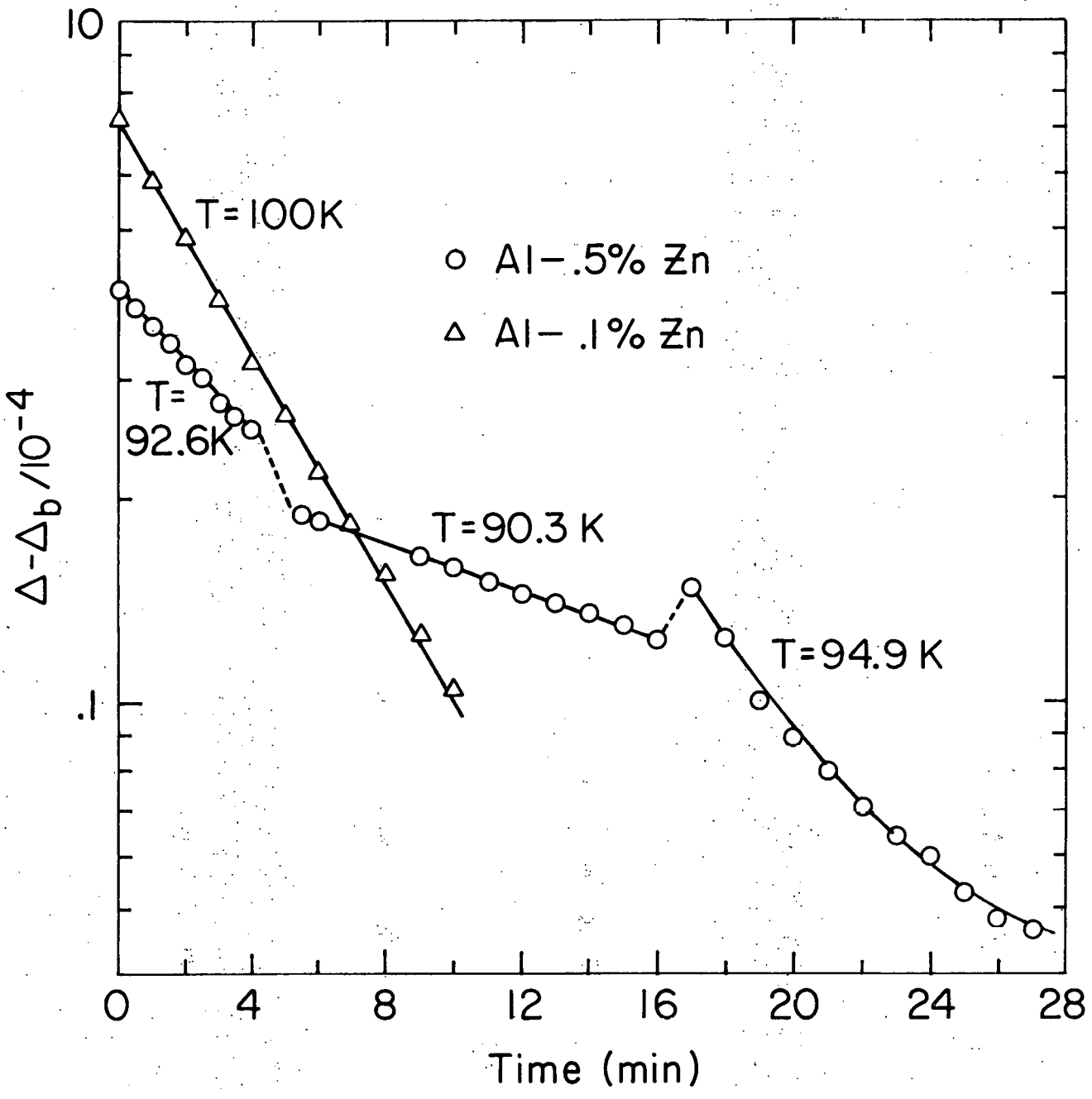
10
.1
$\Delta-\Delta_b/10^{-4}$
T=100K
○ Al-.5% Zn
△ Al-.1% Zn
T=
92.6K
T=90.3 K
T=94.9 K
0
4
8
12
16
20
24
28
Time (min)

In Table VII, the characteristics of the Al-Zn peaks are summarized. Peak 3 has been extracted from the measurements by assuming a Debye form and correcting for annealing.

Table VII. Characteristics of Al-Zn peaks

Peak Number	T_m (10 MHz)	$\Delta m/C$	RT_m (10^3K)
0	2.5K	2	.01
1	4.9K	67	.66
2	30K	3.6	.2
3	103K	26	5.4

Velocity changes were measured from 2K to 30K at 10 MHz for both alloy concentrations. The resonant frequency measurements for the 0.5% alloy are shown in Fig. 28 for both before and after irradiation. Following irradiation, two effects are clearly visible. First, a large and temperature-independent reduction in frequency is easily discernable. Secondly, a large paraelastic dispersion associated with attenuation peak 1 is evident. The two effects can be separated fairly easily by extrapolating the T^{-1} dependence of the paraelastic frequency dispersion. The process is simplified by replotting the frequency change as a function of T^{-1} as shown in Fig. 29. The temperature independent part of the frequency change, then, can be used to calculate the diaelastic modulus change using Eq. 2. (Here, no corrections have been applied for radiation-induced length changes which contribute about 5% of the

Figure 28. Resonant frequency of Al-.5% Zn before and after irradiation. (f_0 = 10,800,000 Hz).

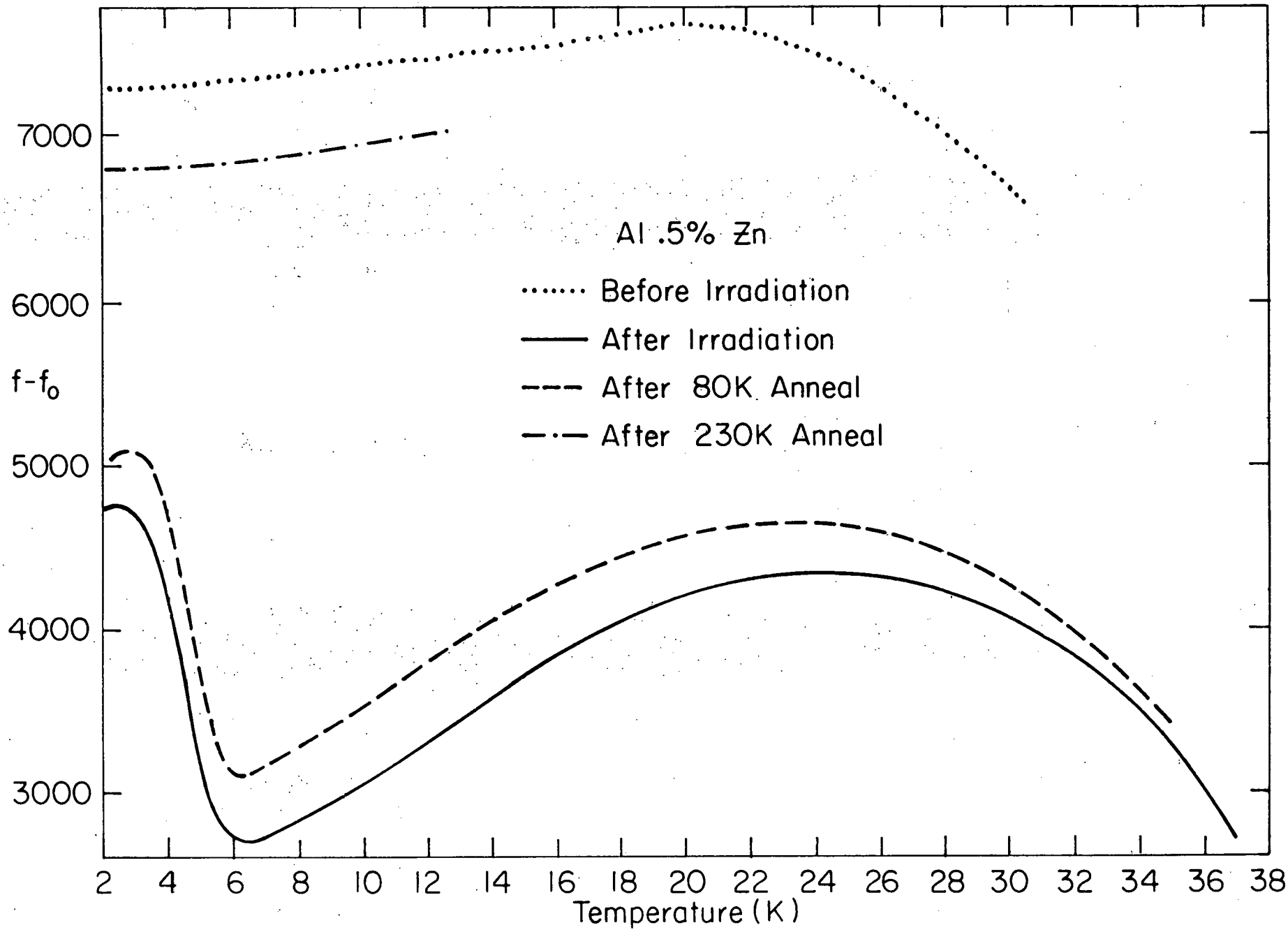
Al .5% Zn
Before Irradiation
After Irradiation
After 80K Anneal
After 230K Anneal
7000
6000
5000
4000
3000
f-f0
2
4
6
8
10
12
14
16
18
20
22
24
26
28
30
32
34
36
38
Temperature (K)

measured frequency change.) The frequency change is correlated with the attenuation measurements, also, in Fig. 29. A similar plot for the 0.1% alloy is shown in Fig. 30.

The temperature-independent part of the frequency change with irradiation is shown in Fig. 31 as a function of annealing temperature. Included are measurements for C_{44} and C' acoustic modes for both alloy concentrations. All of the data have been normalized to a defect concentration of 5 ppm F.P. Particularly interesting is the large anisotropy of the effect and the observation of a large change in the C_{44} effect near 140K.

In Fig. 32, the annealing data is summarized for each of the attenuation peaks, for the radiation-induced resistivity, and for the C_{44} diaelastic effect. The simultaneous annealing near 140K of peak 1, most of the C_{44} diaelastic modulus change, and a large part of the resistivity change offers strong evidence for a close correlation of the effects and leads to the interpretation outlined in part IV.

Figure 29. Al-.5% Zn peak 1. Decrement at 10 and 30 MHz and frequency with background subtracted.

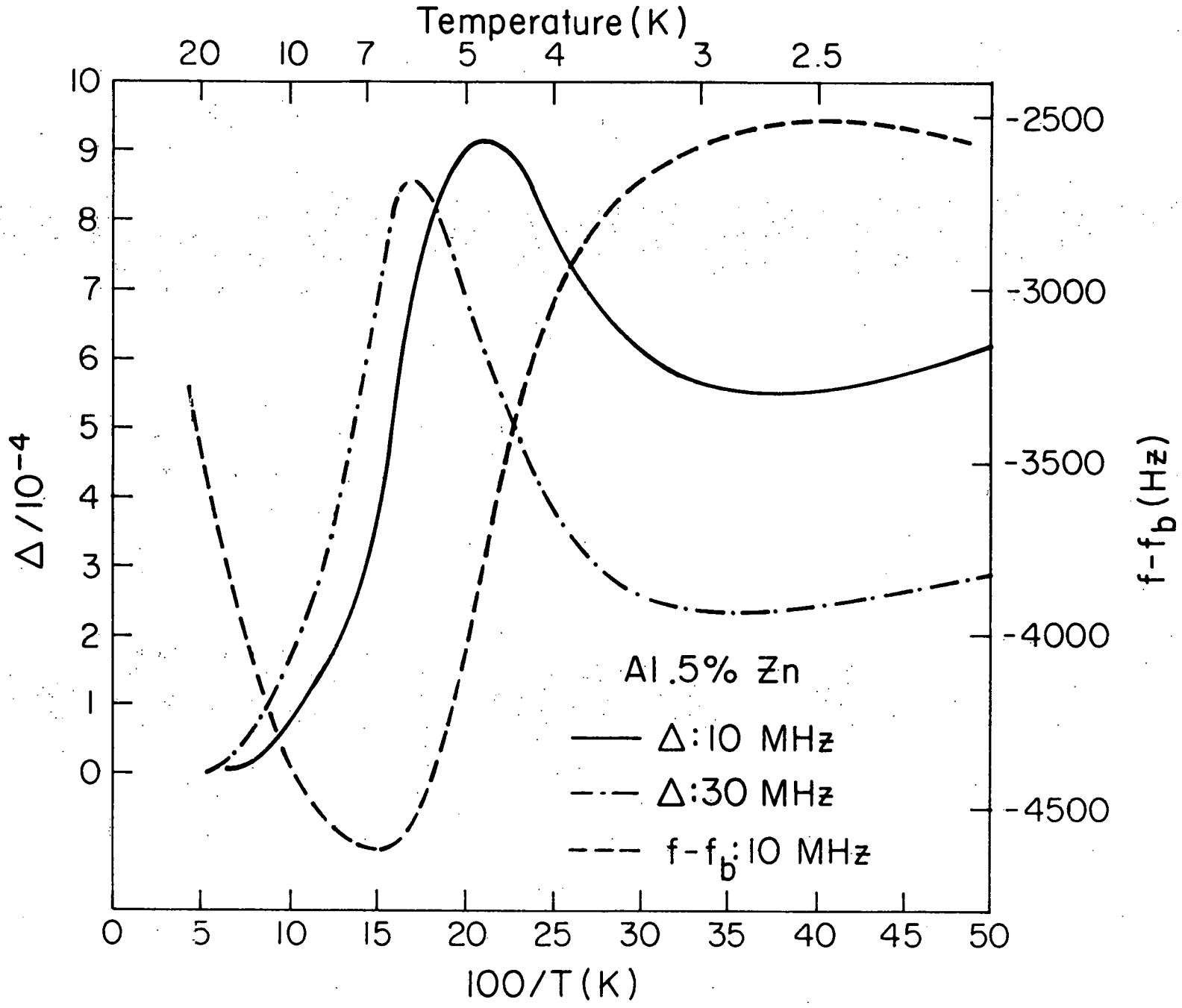
Temperature (K)
20
10
7
5
4
3
2.5
10
9
8
7
6
5
4
3
2
1
0
Δ/10⁻⁴
-2500
-3000
-3500
-4000
-4500
f-f_b (Hz)
Al 5% Zn
Δ: 10 MHz
Δ: 30 MHz
f-f_b: 10 MHz
0
5
10
15
20
25
30
35
40
45
50
100/T (K)

Figure 30. Al-.1% Zn peak 1. Decrement at 10 and 30 MHz and frequency with background subtracted.

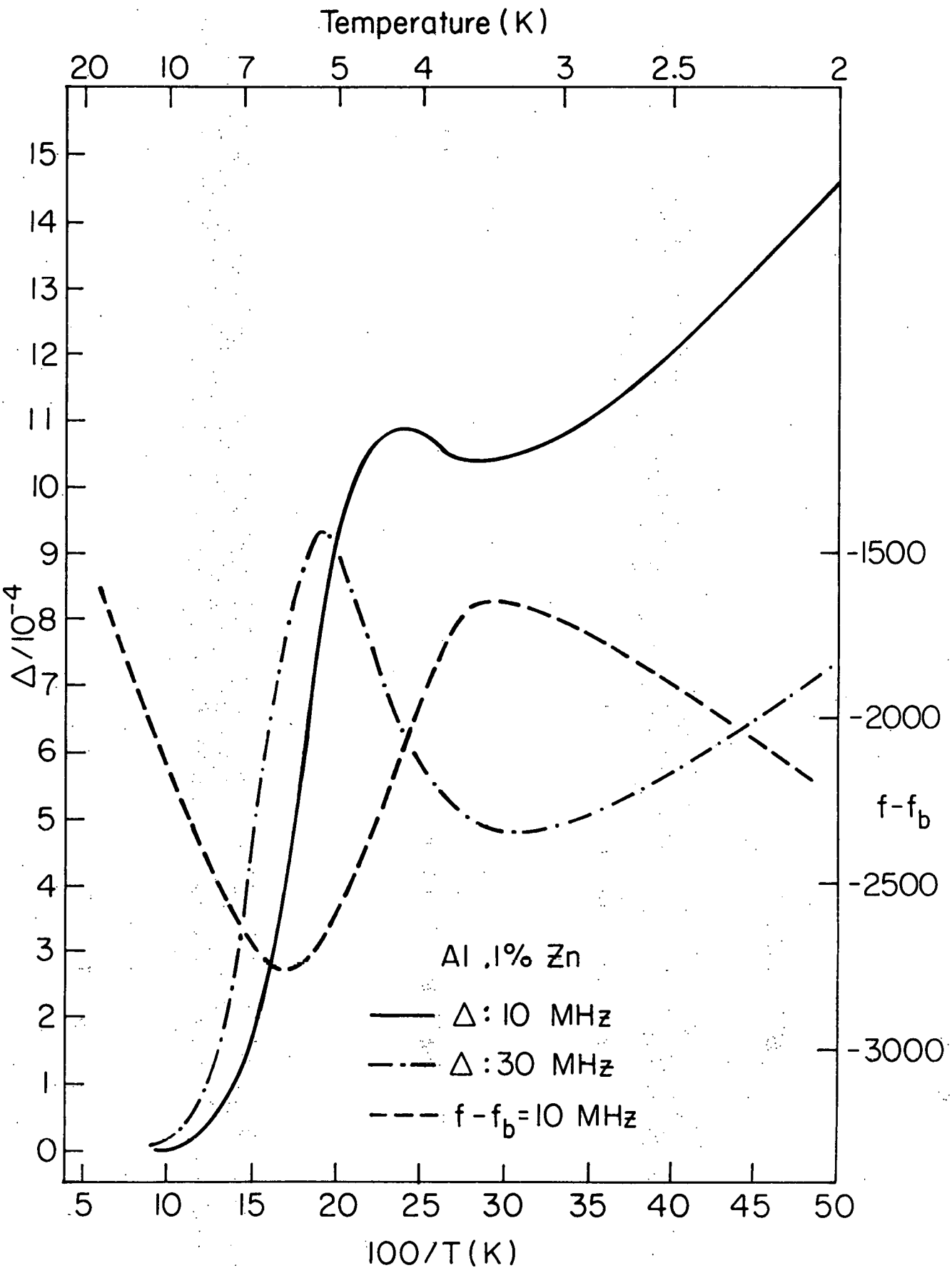
Temperature (K)
20
10
7
5
4
3
2.5
2
15
14
13
12
11
10
9
8
7
6
5
4
3
2
1
0
Δ/10⁻⁴
-1500
-2000
-2500
-3000
f-f_b
Al .1% Zn
Δ: 10 MHz
Δ: 30 MHz
f-f_b=10 MHz
5
10
15
20
25
30
35
40
45
50
100/T (K)

Figure 31. Annealing of the resonant frequency of Al-Zn. The background has been subtracted and the result renormalized to 5 ppm F.P.

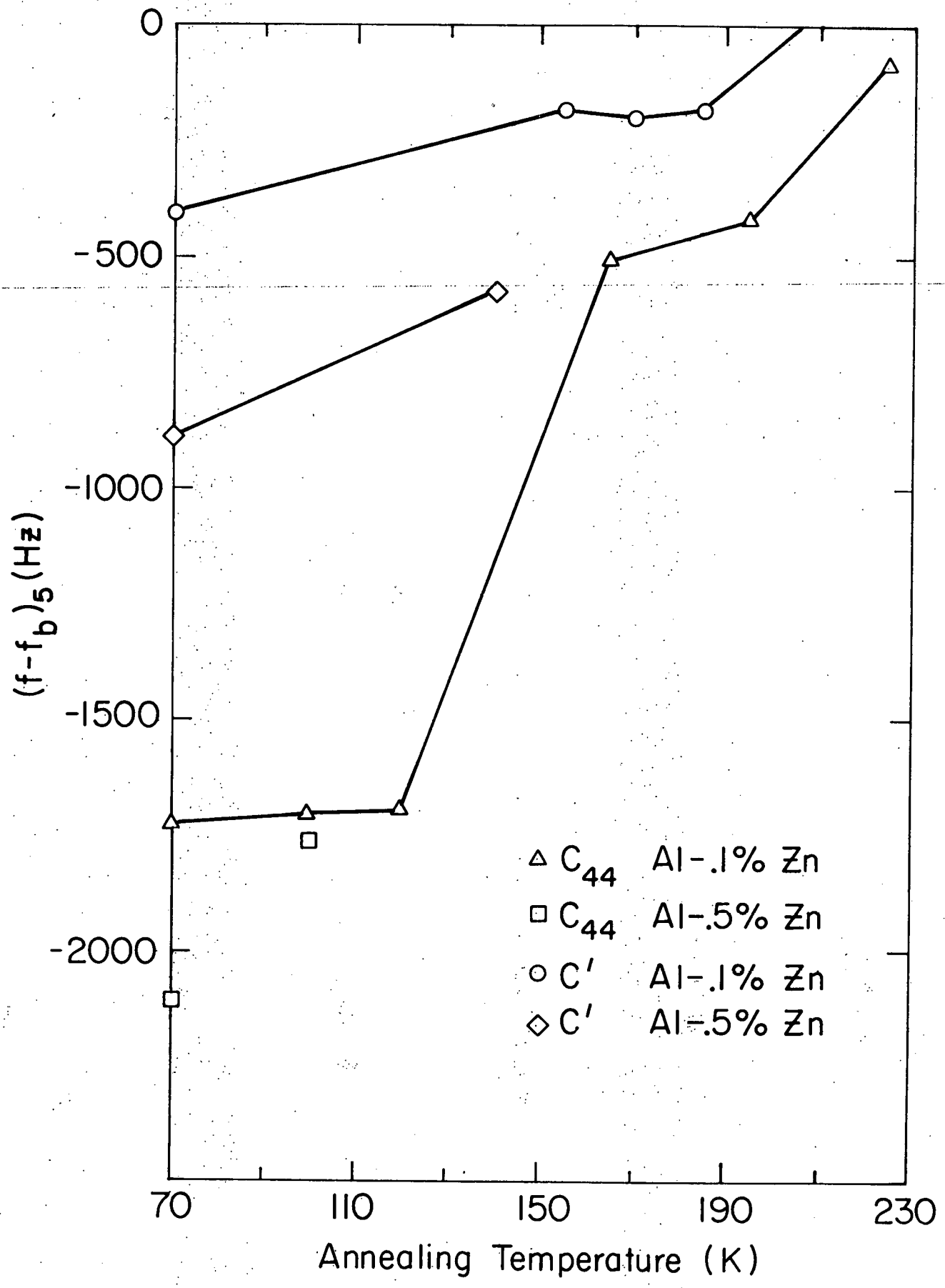
0
-500
-1000
-1500
-2000
$(f-f_b)_5$ (Hz)
70
110
150
190
230
Annealing Temperature (K)
△ C_{44} Al-.1% Zn
□ C_{44} Al-.5% Zn
○ C′ Al-.1% Zn
◇ C′ Al-.5% Zn

Figure 32. Summary of Al-Zn annealing. Peak 3 data is based on isothermal annealing measurements. [Resistivity increment from Snead and Shearin.21/

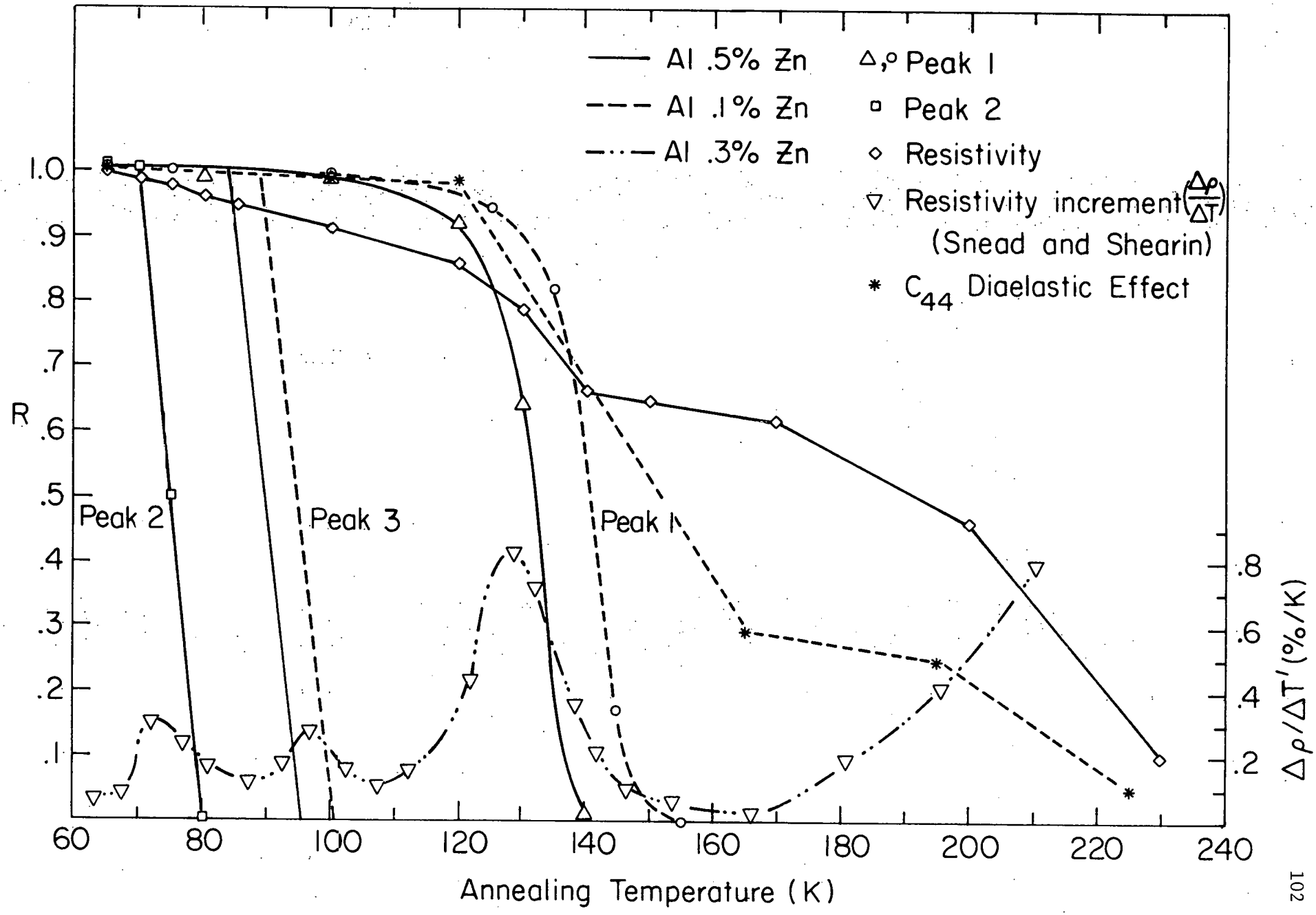
Al .5% Zn
Al .1% Zn
Al .3% Zn
Δ,o Peak 1
□ Peak 2
◇ Resistivity
▽ Resistivity increment (Δρ/ΔT) (Snead and Shearin)
* C44 Diaelastic Effect
R
1.0
.9
.8
.7
.6
.5
.4
.3
.2
.1
Peak 2
Peak 3
Peak 1
60
80
100
120
140
160
180
200
220
240
Annealing Temperature (K)
.8
.6
.4
.2
Δρ/ΔT' (%/K)

III. THEORY

A. Classical Theory of Elastic Dipoles

Before continuing with an interpretation of the experimental results, it is necessary to discuss further the paraelastic and diaelastic effects that arise from point defects. Here, we shall concentrate on particular models for defect configurations, and we will predict effects to be observed in ultrasonic velocity and attenuation measurements.

The theory for paraelastic relaxation effects has been reviewed by Nowick and Berry.[40] Surrounding a point defect in a crystal is a local field of elastic distortions. If the defect has a lower symmetry than that of the crystal, then the strain field produced by the defect will have a "dipolar" character. Depending on the symmetry class of the defect and that of the crystal, there will then exist a number of equivalent possible orientations for the dipole to assume.

An externally applied strain can interact with the dipole through the strain field. For certain externally applied strains, some of the possible dipole orientations may become energetically favored over the others, and thermally activated transitions to the favored orientations will occur. When the externally applied strain is an ultrasonic wave, the reorientation process gives rise to an attenuation and a change in the sound velocity. For a crystal and a defect of given symmetry classes, Nowick and Berry have shown that, on the basis of symmetry arguments, certain externally applied strains can and others cannot

induce transitions. The resulting "selection rules" show, for example, that in a cubic crystal with tetragonal defects, relaxations may occur in the C' acoustic modes but not in the C_{44} acoustic modes. In particular, for an FCC crystal with <100>-mixed dumbbell defects, relaxations may occur in C' modes but not in C_{44} modes. For an FCC crystal with <111> split defects, relaxations may occur in C_{44} modes but not in C' modes.

The strength of the possible relaxation processes can be calculated if the strain field produced by the defect is known. It is convenient to describe the strain field with the so-called "λ-tensor". Then, the general form for relaxation strength is as given in Eq. 11. A different but equivalent treatment of elastic dipole theory describes the defect strain field with a "dipole-tensor" that is simply related to the λ-tensor through elastic constants.

The calculation of the λ-tensor for specific defect configurations is a difficult problem which is best handled numerically. Dederichs, et al.[14] have used a computer simulation technique to calculate the dipole-tensor for various configurations of self-interstitials in copper. Their calculations are based on three different models for the interatomic potential. Whether or not their results can be extended to the aluminum lattice is in question. However, this is often done, and in fact, radiation damage results in aluminum are very similar to those found in copper.

Their results show that the <100>-split-dumbbell is a nearly isotropic configuration, and should, therefore, give rise to a relatively

small relaxation peak. On the other hand, the <110>-split, the crowdion, and the <111>-split configurations all produce large distortions along certain <110> directions. The result is that for these configurations, the dipole-tensor is highly anisotropic and strong relaxation peaks are to be expected. The prediction of this calculation for the strength of a <100>-split-dumbbell relaxation process is in quantitative agreement with the strength of the process observed by Spirić et al.[12] in pure Al.

No calculated values of the dipole-tensor have been published for interstitials trapped at impurities. However, certain qualitative predictions can be made. For interstitials trapped at highly undersized impurity atoms, Dederichs' trapping model predicts that the impurity will occupy the octahedral site. Thus, the dipole-tensor is isotropic and no relaxations are expected. For interstitials trapped at slightly undersized impurities, the possible trapping configurations are small perturbations of the isolated interstitial configurations. Thus, the qualitative arguments based on geometrical coupling to <110> chains of atoms carry over to the trapped configurations as well. The <100>-mixed dumbbell should give rise to weak relaxation peaks in the C' acoustic modes, while the <111>-mixed defect should give rise to strong peaks in the C_{44} acoustic mode.

An externally applied strain field may also interact with a crystal defect by inducing a polarization of the defect. The interaction may be characterized by the "diaelastic polarizability" of the defect. The interaction leads to a reduction of the elastic constants and, hence, to a reduction of the sound velocities. Dederichs, et al.[14] have shown

that vacancies and substitutional defects are expected to produce only very small changes in the elastic constants. However, large and negative changes are expected for interstitials.

Dederichs, et al. have also shown that the expected magnitudes of the changes in the elastic constants are governed to a large extent by a set of "selection rules" based on symmetry. The <100>-dumbbell, for instance, is expected to lead to large changes in the C_{44} elastic constant. A simple qualitative argument demonstrates that this result is reasonable. First, using standard results[40] from elasticity theory, it is easy to show that in a cubic crystal, the elastic modulus for a longitudinal wave propagating in a <100> direction is $C_{11} = B + (4/3)C'$ where B is the bulk modulus. Also, for a longitudinal wave propagating along a <111> direction, the modulus is $B + (4/3)C_{44}$. Thus, since hydrostatic stress cannot induce a polarization of defects, the affect of a C' strain on polarization will be similar to that of a compression along a <100> direction. Likewise, a C_{44} strain will be similar to a <111> compression.

Now, for a <100> dumbbell, the effect of a C' strain is to compress the dumbbell along its axis. For such a strain, very small lattice distortions result. On the other hand, a C_{44} strain will tend to rotate a <100> dumbbell towards a close packed <110> direction. Thus, large, long-range distortions are expected along certain <110> directions, and therefore, a large induced polarization results.

For a <111> defect, a C_{44} strain will tend to compress the defect, and a C' strain will tend to rotate it towards a <110> direction. The

interesting result, then, is that the anisotropy of the changes of the elastic constants can be used to distinguish the presence of <100> and <111>-type defects.

A calculation of the diaelastic polarizability of specific defect configurations is also best done with computer simulation methods. Dederichs, et al.[14] have calculated the change in the elastic constants for vacancies and <100>-split dumbbells. Their numerical results are in agreement with the qualitative description just outlined.

In summary, if <100> defects are introduced into a crystal, then relatively weak paraelastic relaxation processes are expected in the C' acoustic mode, and a large diaelastic drop of the modulus is expected in the C_{44} mode. On the other hand, if <111> defects are introduced, then strong paraelastic relaxations are expected in C_{44}, and a large diaelastic modulus drop is expected in C'.

B. Tunneling Effects

The observation of a strange, non-classically shaped peak at low temperatures in Al-Zn prompted an investigation into the possible effects of defect tunneling on elastic measurements. A basis from which to build has been provided by the extensive work in recent years on the tunneling of off-center impurities in alkali halides. However, the available theory has been developed mainly for electrical and magnetic effects, and does not deal with diaelastic effects, nor does it yield useful relations for the paraelastic acoustic attenuation and velocity changes.

Before continuing with a dicussion of possible tunneling effects, it is instructive to consider a simple, purely classical model for a particle in a one-dimensional crystal. The potential in which the particle is assumed to move is a double harmonic well potential

$$\begin{aligned} V = V_A &= \tfrac{1}{2}k\ (x+x_0)^2 \text{ for } x < 0 \\ V_B &= \tfrac{1}{2}k\ (x-x_0)^2 \text{ for } x > 0. \end{aligned} \tag{13}$$

Classically, the particle may sit in either well and the permanent dipole moment for the defect is just x_0. For a large crystal with many such defects, the average dipole moment, M is given by

$$M = c_A(-x_0) + c_B(x_0) \tag{14}$$

where c_A and c_B are the concentrations of defects in which the impurity is sitting in well A (negative x) and in well B (positive x), respectively.

If an external force of magnitude F is applied in the negative x direction, then the potential will be changed to

$$\begin{aligned} V &= \tfrac{1}{2}k(x+x_0)^2 - Fx \text{ for } x < 0 \\ &= \tfrac{1}{2}k(x-x_0)^2 - Fx \text{ for } x > 0. \end{aligned} \tag{15}$$

The application of the force has two effects on the potential. First, the position of the energy minimum of each well is shifted in the +x direction by F/k. And second, the energy minimum of well A is raised to

$$E_A = Fx_0 - F^2/2k \tag{16}$$

while the energy minimum of well B is reduced to

$$E_B = -Fx_0 - F^2/2k. \tag{17}$$

The dipole moment is now given by

$$M = c_A(-x_0+F/k) + c_B(x_0+F/k) \tag{18}$$

and the thermal equilibrium defect concentrations are related by the Boltzman factor

$$c_A = c_B \exp[(E_B-E_A)/k_BT]. \tag{19}$$

If the total defect concentration is $c = c_A + c_B$, then the dipole moment can be rewritten as

$$M = cx_0 \tanh (Fx_0/k_BT) + cF/k. \tag{20}$$

The origin of the two terms in Eq. (20) is clear. The last term is an induced dipole moment that results from the displacement of the two wells by an amount F/k. This term is temperature independent. The first term is strongly temperature dependent and arises from the thermally activated repopulation of the wells upon application of the force. The first term will give rise to paraelastic effects, while the second term will give rise to diaelastic effects.

The double well potential of Eq. 13 can also be used as a defect model in a full quantum mechanical treatment. Gomez et al.[41] have

calculated the energy levels of this system in the absence of external strain, and they have shown that for a sufficiently weak overlap of the harmonic oscillator states, the lowest energy states form a two-state system with energies given by

$$E_+ = 1/2\ \hbar\omega + \Delta_0,$$
$$E_- = 1/2\ \hbar\omega - \Delta_0 \tag{21}$$

where $\omega = \sqrt{k/m}$, m is the mass of the particle, and Δ_0 is a small overlap integral.

In an externally applied strain field ε, the energy levels will be changed to

$$E_+ = (\Delta_0^2+\alpha^2\varepsilon^2)^{1/2}$$
$$E_- = -(\Delta_0^2+\alpha^2\varepsilon^2)^{1/2} \tag{22}$$

where now the zero point energy has been suppressed, since only energy differences matter in what follows.

We turn now to a more general discussion of the relationship between paraelastic ultrasonic effects and the strain dependence of the energy levels. Later, we will return to the two-state model and make specific predictions of velocity and attenuation effects.

The change in elastic constant for a crystal containing defects is given by

$$\delta C = (\partial^2 F/\partial\varepsilon^2) \tag{23}$$

where F is the Helmholtz free energy and ε is an externally applied strain. F is given by the partition function, Z, and the defect concentration, c, as

$$F = (-kTc)\ell nZ \tag{24}$$

where

$$Z = \sum_i \exp(-E_i/kT), \tag{25}$$

and the sum is carried out over all the system energy states, of energy E_i.

The differentiation of Eq. 24 can be carried out formally. The first derivative with ε is just

$$\partial F/\partial \varepsilon = \sum_i c_i(\partial E_i/\partial \varepsilon) \tag{26}$$

where c_i, the concentration of defects in state i, has been substituted for $c \exp(-E_i/kT)/Z$. Then, the change in the elastic constant is given by

$$\delta C = \sum_i c_i(\partial^2 E_i/\partial \varepsilon^2) + (\partial c_i/\partial \varepsilon)(\partial E_i/\partial \varepsilon). \tag{27}$$

This is the elastic constant change for thermal equilibrium, i.e., assuming that there is sufficient time for the concentration c_i to adjust to its thermal equilibrium value for each strain ε. The first term represents the elastic constant change when no concentration redistribution occurs. The second term then represents the change resulting from the repopulation and can therefore be identified as the

relaxation strength for a Debye relaxation process. For an ultrasonic strain, the second term gives rise to an attenuation peak and a dispersion in the velocity as described by the Debye equations. The first term in the sum leads to a change in the modulus which, except at very high frequencies, follows the applied strain. For an ultrasonic wave, the first term leads to a temperature dependent reduction of the modulus with no associated attenuation in the ultrasonic frequency range.

Now, for a specific example, we return to the two state system with energy levels given by Eq. 22. The relaxing and non-relaxing parts of the modulus change can be evaluated separately. First, the result for the relaxing part is

$$\delta C_R = (-\alpha^2/kT)\,\frac{\alpha^2\varepsilon^2}{\Delta_0^2 + \alpha^2\varepsilon^2}\,\mathrm{Sech}^2\,\frac{(\Delta_0^2+\alpha^2\varepsilon^2)^{1/2}}{kT} \tag{28}$$

and second, the result for the non-relaxing part is

$$\delta C_{NR} = (-\alpha^2/kT)\,\frac{\Delta_0^2 kT}{(\Delta_0^2+\alpha^2\varepsilon^2)^{3/2}}\,\tanh\,\frac{(\Delta_0^2 + \alpha^2\varepsilon^2)^{1/2}}{kT}. \tag{29}$$

Finally, $R = \delta C/C$ is renormalized and plotted against the normalized inverse temperature, Δ_0/kT for various values of the normalized strain, $\beta = \alpha\varepsilon/\Delta_0$. Figs. 33 and 34 show the results for the relaxing and non-relaxing parts separately, while Fig. 35 shows the result for the total modulus change. Both parts of the modulus change show the characteristic T^{-1} dependence at high temperatures. At very low temperatures, the population freezes into the ground state of the system, and the relaxing part must go to zero. The non-relaxing part, however, remains large.

Figure 33. Relaxing part of normalized relative modulus change as a function of normalized inverse temperature for various values of normalized strain.

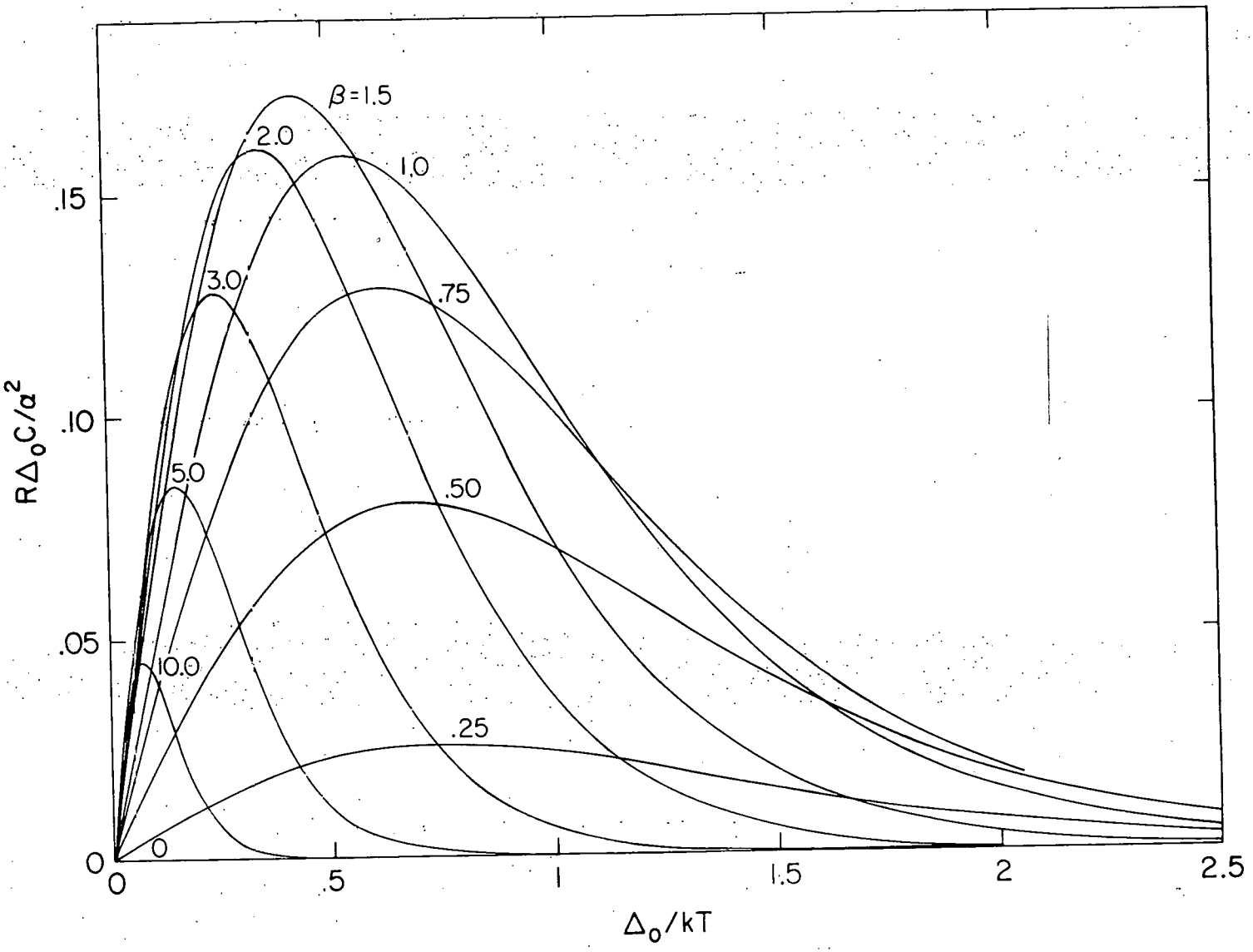
β=1.5
2.0
1.0
3.0
.75
5.0
.50
10.0
.25
0
.15
.10
.05
0
0
.5
1
1.5
2
2.5
RΔ₀C/a²
Δ₀/kT

Figure 34. Non-relaxing part of normalized relative modulus change and normalized time constant as a function of normalized inverse temperature for various values of normalized strain.

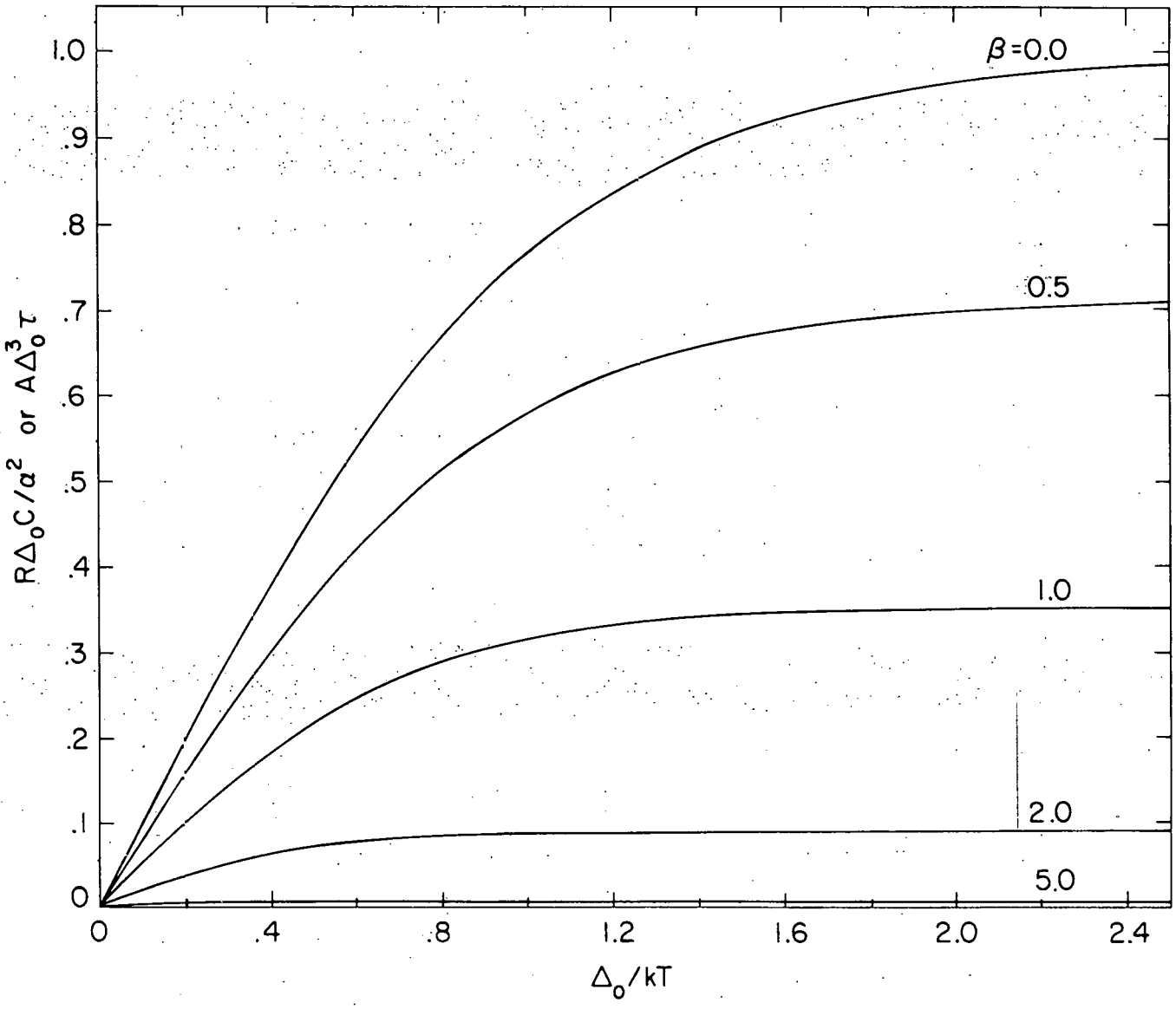
1.0
.9
.8
.7
.6
.5
.4
.3
.2
.1
0
$R\Delta_0 C/a^2$ or $A\Delta_0^3\tau$
β=0.0
0.5
1.0
2.0
5.0
0
.4
.8
1.2
1.6
2.0
2.4
Δ_0/kT

Figure 35. Relative modulus change as a function of normalized inverse temperature for various values of normalized strain.

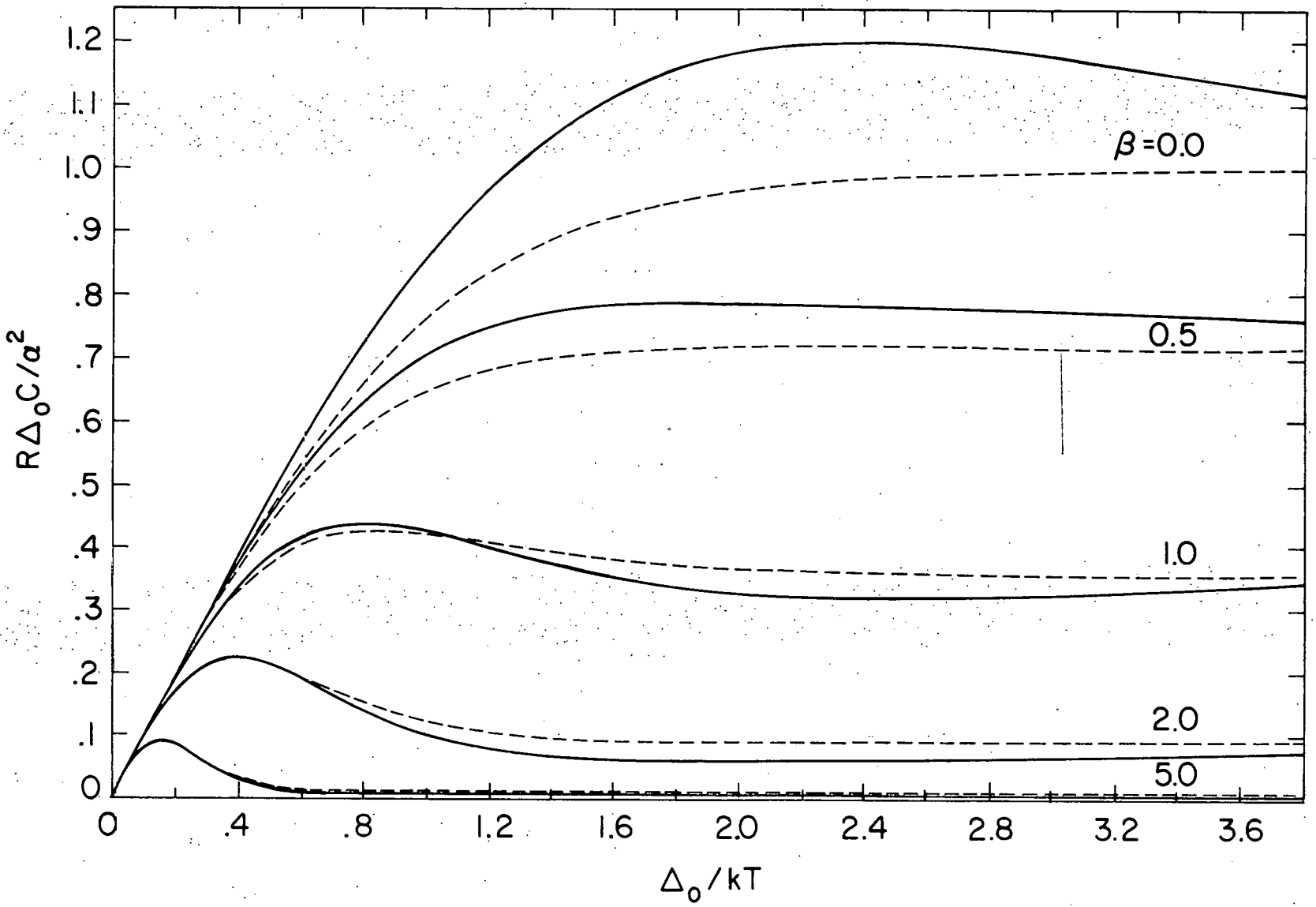
1.2
1.1
1.0
.9
.8
.7
.6
.5
.4
.3
.2
.1
0
$R\Delta_0 C/a^2$
β=0.0
0.5
1.0
2.0
5.0
0
.4
.8
1.2
1.6
2.0
2.4
2.8
3.2
3.6
Δ_0/kT

The time constant τ, for single phonon aided and direct transitions in the two state system has been shown[42] to satisfy a relation of the form

$$\tau^{-1} = A\,\Delta^3 \coth(\Delta/kT) \tag{30}$$

where 2Δ is the energy gap, and A is a constant involving lattice constants. In this two-state system, $\Delta = \sqrt{\Delta_0^2 + \alpha^2\varepsilon^2}$, so τ is given by the relation

$$A\Delta_0^3\tau = \frac{1}{(\Delta_0^2+\alpha^2\varepsilon^2)^{3/2}} \tanh \frac{(\Delta_0^2+\alpha^2\varepsilon^2)^{1/2}}{kT}. \tag{31}$$

The time constant has also been appropriately normalized and plotted against T^{-1} in Fig. 34. The curves display the interesting freezing of τ to a constant value at low temperatures. Such a freezing of the time constant leads to a possible explanation for the strange shape of the C' peak in Al-Zn.

The possibility of extending the ideas presented here to more realistic defect models has been investigated. One interesting observation is that the more complex models seem, in the long run, to lead back to the two-state model as an appropriate approximation. For example, a four-state model with energies given by

$$\begin{aligned} E_1 &= -\sqrt{\Delta_0^2 + \alpha^2\varepsilon^2} \\ E_2 &= -\alpha\varepsilon \\ E_3 &= +\alpha\varepsilon \\ E_4 &= +\sqrt{\Delta_0^2 + \alpha^2\varepsilon^2} \end{aligned} \tag{32}$$

has been investigated. The total modulus change is plotted in Fig. 35 along with the similar result for the two-state system. The similarity of the results is to be expected since the high temperature limit is given by the classical result which is the same for both systems, and the low temperature limit is determined by the ground state, which also has the same form for both systems.

The formalism has been set up by Gomez, et al.[41] for analyzing three dimensional models. They have calculated the energy levels but not the elastic constants for 6-, 8-, and 12-state tunneling models including externally applied strain. Further work in this area needs to be done. However, we have now developed a sufficient qualitative picture of tunneling effects to return to a discussion of the experimental results.

IV. INTERPRETATION AND SUMMARY

A. Interpretation

The experimental measurements reveal an ultrasonic attenuation "spectrum" that is rich in relaxation peaks for each of the irradiated aluminum alloys. The complexity of the spectra and the unique annealing behavior of each of the relaxation peaks indicates that in each alloy there exists a multiplicity of interstitial trapping configurations. Although the measurements provide a characterization of each peak, it has not proved possible to identify the defect geometry involved for each of the relaxation processes. Furthermore, in the cases of Al-Fe and Al-Mn, it has not been possible to estimate the relative concentration of each defect species, nor has it been possible to separate out the diaelastic contribution of each defect. In the case of Al-Zn, however, the observation of simultaneous annealing of paraelastic, diaelastic, and resistivity effects in distinct stages allows for a more complete characterization of each peak, and leads the way to a model for each defect configuration. Many of the observations, though, remain unexplained.

In this section, we shall first discuss an interpretation of the effects observed in Al-Zn. Then, we shall show how the interpretation of Al-Zn leads to a possible interpretation of Al-Fe that is consistent with the channelling results of Swanson, et al. and the Mössbauer measurements of Vogl an Mansel.[15]

The attenuation measurements made on Al-Zn immediately following irradiation, Fig. 22, show that there are two peaks to be dealt with. One peak appears in the C' acoustic mode near 5K. The other peak appears in C_{44} near 100K, and has almost completely annealed out following a 10-minute anneal at 100K. Since Nowick and Berry[40] have pointed out that a single defect can give rise to multiple relaxation peaks, it is important to establish whether or not there are distinct defects in Al-Zn.

The measurements in Fig. 24 of the annealing of the C' peak show that the peak remains nearly unchanged in strength as the C_{44} peak anneals out, and that the peak does not anneal out until about 140K. Therefore, each peak must be related to a distinct defect. Furthermore, the annealing behavior also reveals that the entire radiation-induced attenuation change from 2K to 10K anneals out uniformly, and so demonstrates that a single defect species is involved even though the shape of the peak is highly non-classical.

With two defect types to deal with, we must answer the question of which defect, if either, is present in predominant concentration. From Table VII, we notice that although the size of the attenuation peak in C_{44} is smaller than that of the peak in C', the C_{44} peak is nearly an order of magnitude larger than the C' peak when compensation is made for the T^{-1} dependence of the relaxation strength (Eq. 11). Also, according to Eq. 11 the defects that give rise to the C_{44} peak are, therefore, either present in predominant concentration, or they have a much larger permanent dipole moment than those defects that give rise to the C' peak.

The annealing of the diaelastic part of the resonant frequency change, Fig. 31, provides evidence that the C' defect is in predominant concentration. First, immediately after irradiation, the change in the C_{44} modulus is much larger than the change in the C' modulus. This is the behavior expected for a defect which leads to an attenuation peak in C'. Furthermore, only small changes in the diaelastic measurements occur during the annealing of the C_{44} peak, while only a small part of the diaelastic effect remains following the annealing of the C' peak.

Further evidence that the C' peak defect is predominant is obtained from an examination of the resistivity annealing data shown together with the peak annealing data in Fig. 32. Only a small change in resistivity is associated with the annealing of the C_{44} peak, while a large change is associated with the annealing of the C' peak.

If most of the trapped interstials are present in the configuration that gives rise to the C' peak, then their concentration is approximately that determined from the resistivity change. Then, using Eq. 11 and the experimentally measured relaxation strength, the defect shape-factor can be calculated, and the result is $|\delta\lambda| = 0.07 \pm .01$ where the error comes mainly from the concentration estimation. For comparison with other measurements, the result may be converted to an "anisotropy of the dipole force tensor", δP, using

$$P_{ij} = \sum_{k\ell} C_{ijk\ell}\lambda_{k\ell}. \qquad (33)$$

The result is $|\delta P| = .40 \pm .05$eV. An isotropic defect has $|\delta P| = 0$, and the value cited by Spiríc et al.[12] for carbon in iron is 6.0 eV. The

corresponding results from the computer calculations of Dederichs, et al.[14] are $|\delta P| = 0.9 \pm .4$eV for a <100>-split dumbbell, and $|\delta P| = 10 \pm 4$eV for a <111>-split configuration.

In summary, the evidence is strong for identifying the predominant trapping configuration below 140K as a <100>-mixed dumbbell. The diaelastic modulus has the expected anistropy, and there is a paraelastic relaxation peak associated with the diaelastic effect which appears in the proper acoustic mode and has the expected strength for a <100> dumbbell. The experimental results are consistent, also, with interpreting the C_{44} peak as arising from a small concentration of <111>-mixed defects. Although their concentration is small, their dipole moment is large, and hence, they give rise to a peak in the attenuation which is almost ten times stronger than the <100>-mixed dumbbell peak. If one uses the Dederichs estimate for the dipole strength, then the concentration of the <111>-mixed defect is at least an order of magnitude smaller than that of the <100>-mixed dumbbell.

Now, we turn to a discussion of the curious shape of the C' attenuation peak. Fig. 30 shows the velocity and attenuation measurements from 2K to 20K as a function of T^{-1}. At temperatures about 4K, the peak has the expected shape and the velocity has the expected dispersion and a T^{-1} region. The continued increase of attenuation at low temperatures after passing through a maximum is, however, unexpected.

One possible interpretation of the increase at low temperature is that there is a second relaxation peak at very low temperature. However, that attempt fails on two counts: first, the rate of increase at low

temperature is too slow to be the edge of a second peak, and second, the change in the shape of the peak on going from 10 MHz to 30 MHz cannot be explained in this way.

We are left with the interpretation that the peak is a single Debye relaxation process. Now however, we no longer assume that the time constant, τ, is given by a classical thermal activation process, Eq. 10, or that the relaxation strength, R, is given by the classical result, Eq. 11. Instead, the two parameters are determined experimentally by using the Debye equations, Eqs. 6 and 7, and measuring the attenuation and velocity at a fixed frequency or the attenuation at two different frequencies.

The resulting values of τ and R using both methods and both alloy concentrations are shown in Figs. 36 and 37. For temperatures above 5K, τ approaches an exponential form as in the classical result. Using the classical form, the activation energy is 5.4 meV and the frequency factor is $5 \times 10^{12} \text{sec}^{-1}$. However, at low temperatures, τ freezes out to a constant value of 2×10^{-8} sec. This behavior is similar to the freezing out of τ in the two-state tunneling model discussed in part III. It represents the temperature independent direct transition rate.

The relaxation strength shown in Fig. 37 displays a sensitivity to alloy concentration. The result of higher impurity concentration is expected to be an increase in internal strain. The observed change in R with concentration can then be qualitatively understood with the aid of the results for the two-state tunneling model given in Fig. 33.

The qualitative features of the relaxation strength and the time constant can be understood with the tunneling model. However, one

Figure 36. Time constant derived from velocity and decrement measurements of Al-Zn peak 1.

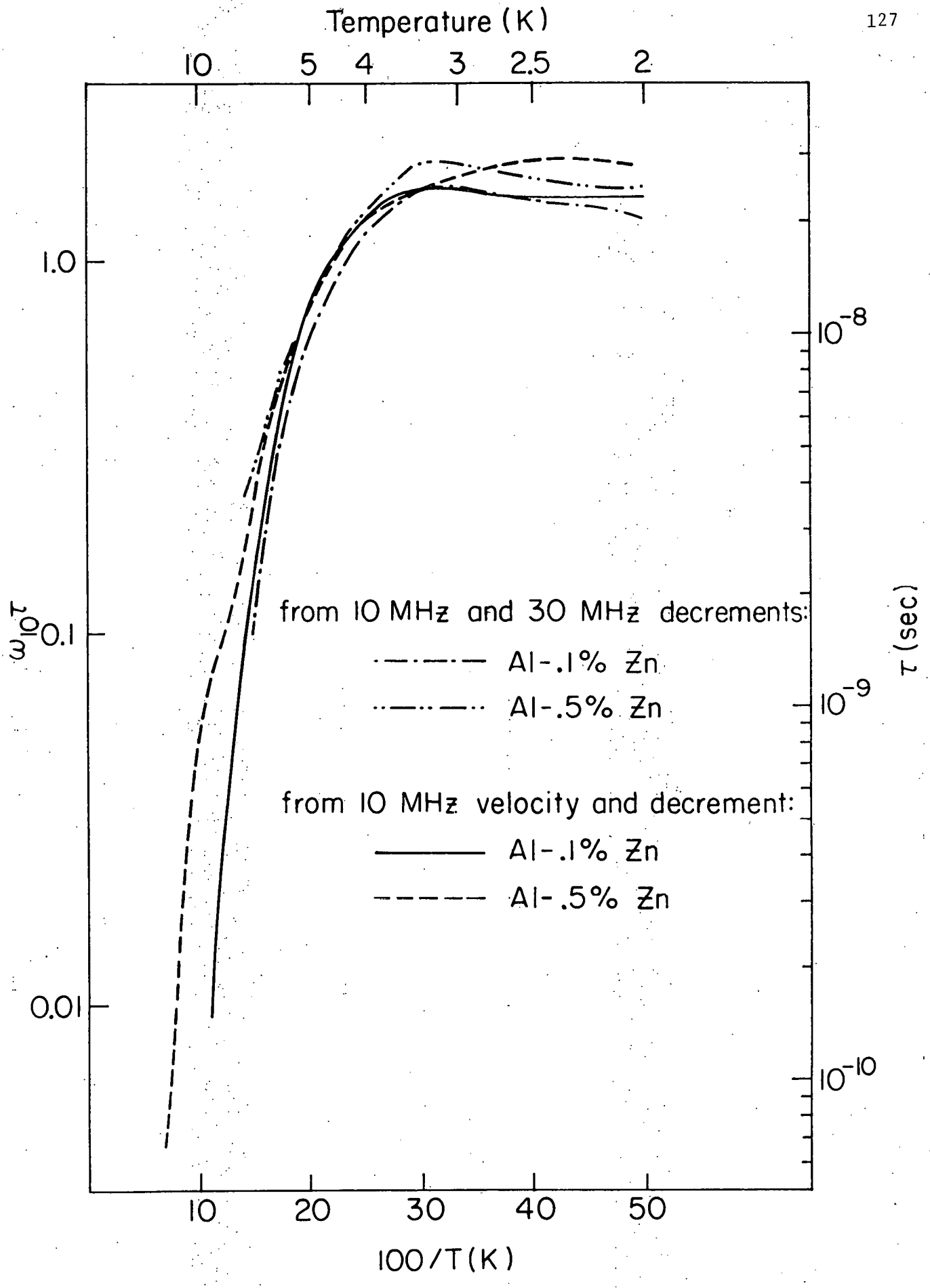
Temperature (K)
10
5
4
3
2.5
2
1.0
0.1
0.01
$\omega_{10}\tau$
10^{-8}
10^{-9}
10^{-10}
τ (sec)
from 10 MHz and 30 MHz decrements:
Al-.1% Zn
Al-.5% Zn
from 10 MHz velocity and decrement:
Al-.1% Zn
Al-.5% Zn
10
20
30
40
50
100/T(K)

Figure 37. Relaxation strength normalized to 5 ppm F.P. Derived from velocity and decrement measurements of Al-Zn peak 1.

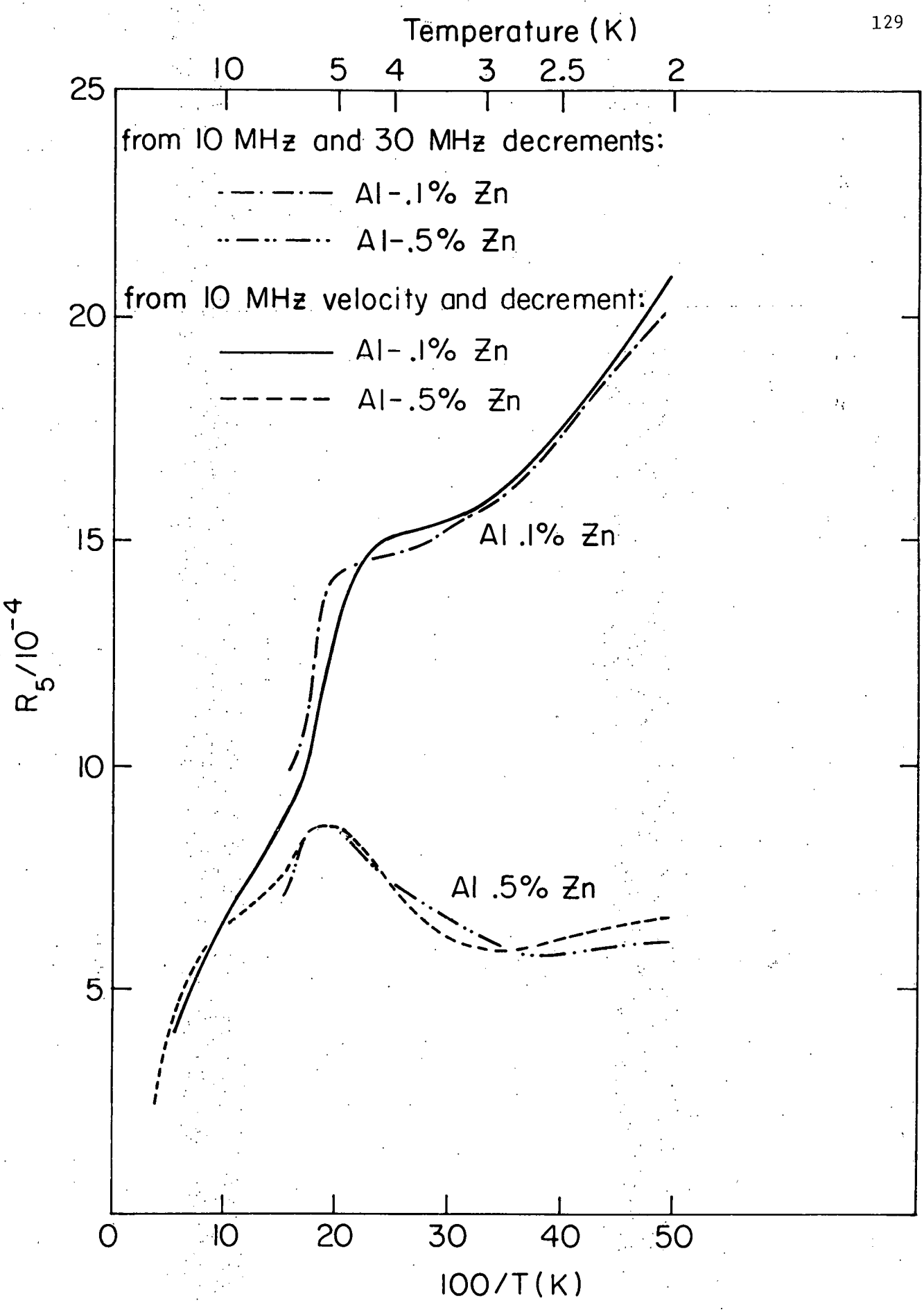
Temperature (K)
10
5
4
3
2.5
2
25
20
15
10
5
0
10
20
30
40
50
100/T(K)
$R_5/10^{-4}$
from 10 MHz and 30 MHz decrements:
Al-.1% Zn
Al-.5% Zn
from 10 MHz velocity and decrement:
Al-.1% Zn
Al-.5% Zn
Al .1% Zn
Al .5% Zn

difficult problem arises when trying to explain the alloy concentration effect: the two-state model predicts that for the observed sensitivity of R to concentration, τ must also be sensitive to concentration contrary to the observations. In summary, a classical model is incapable of explaining the experimental results. The two-state tunneling model does, however, qualitatively display the observed behavior, and it encourages the development of a more complete quantum-mechanical model for an impurity in a three-dimensional, six-well potential as well as more systematic studies of the strain dependence of the effect.

The key to understanding the attenuation peaks in Al-Zn was the observation of a large diaelastic modulus change in C_{44} and a much smaller change in C'. In this respect, the results for Al-Fe are not so different from those for Al-Zn. Fig. 38, which is a summary of all of the observed paraelastic and diaelastic measurements, clearly shows the radically different relaxation effects observed in the two alloys. However, despite the fact that there are a number of very strong peaks in the C_{44} mode, the anisotropy of the diaelastic effect indicates that the predominant defect species should lead to relaxation effects in the C' mode. In fact, there is a strong peak in C'. A possible interpretation, then, is that as in Al-Zn, the <100>-mixed dumbbell is the predominant defect. The peak in C' results from relaxation of the dumbbell. The C_{44} peaks result from defects that are low in concentration, and ones that have strong permanent dipole moments.

The earlier measurements by Rehn, et al.[19] were paraelastic measurements on polycrystalline samples and one single crystal oriented for a

Figure 38. Summary of peaks, modulus change, and annealing for Al-Mn, Al-Fe, and Al-Zn. Decrement at 10 MHz with background subtracted and normalized to 5 ppm F.P.

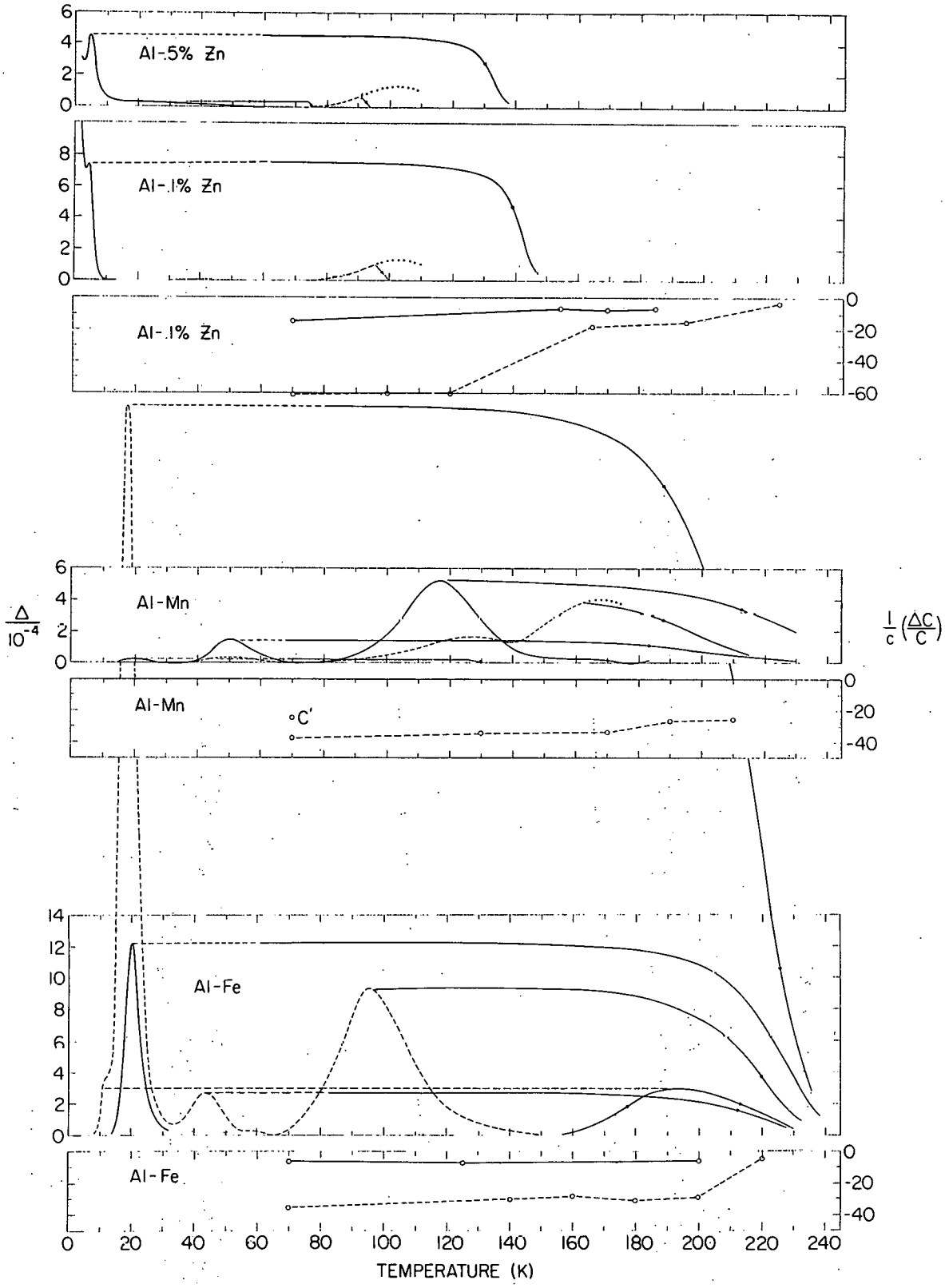
Al-.5% Zn
Al-.1% Zn
Al-.1% Zn
Al-Mn
Al-Mn
°C'
Al-Fe
Al-Fe
Δ / 10⁻⁴
1/c (ΔC/C)
TEMPERATURE (K)

C_{44} mode. They obtained evidence for <111> symmetry defects, but had insufficient sensitivity to resolve the smaller <100> peak. Their results therefore appeared to be in conflict with existing theory and channelling and Mössbauer measurements. The above interpretation of the ultrasonic measurements, which identifies the smaller peak with the predominant defect species, then resolves the apparent contradiction and restores the simple picture of the <100>-mixed dumbbell as the major defect.

This interpretation cannot be extended to the Al-Mn measurements for two reasons: first, the diaelastic effects are only slightly anisotropic, and second, there is no satisfactory candidate for a relaxation peak associated with the caging motion of a <100>-mixed dumbbell. The Al-Mn interpretation remains a mystery and poses a problem for interstitial trapping models that are based solely on impurity size effects.

B. Summary

1) The ultrasonic technique has proved to be a sensitive probe of the properties of defects in irradiated aluminum alloys. The ability to make simultaneous measurements of resistivity and ultrasonic velocity and attenuation has allowed the characterization of individual defects, even when multiple defects are present.

2) Strong evidence is provided showing that the predominant interstitial trapping configuration in Al-Zn below 130K is the <100>-mixed dumbbell configuration. The defect gives rise to an attenuation peak in the C' acoustic mode near 4.9K at 10 MHz with a shape factor

$|\delta\lambda|$ = 0.12. Additionally a peak occurs in C_{44} near 100K that arises from a smaller concentration of, probably, <111>-mixed configurations. The shape of the 4.9K attenuation peak and velocity dispersion provide evidence of defect tunneling.

3) The observation of an attenuation peak in C' in Al-Fe that was not previously detected by Rehn, et al.[19] and the measurement of relative diaelastic modulus changes per unit concentration F.P. of -36 for C_{44} and -5 for C' resolves the apparent contradiction between the internal friction and channelling symmetry evidence, and allows for an interpretation in terms of a <100>-mixed dumbbell which is consistent with previous theory and channelling and Mössbauer measurements.

4) The results for Al-Mn and Al-Fe are very different from each other. Since Fe and Mn have similar mass and size differences in the aluminum lattice; this result is inconsistent with trapping models based solely on size differences.

REFERENCES

1. D. L. Johnson, Ph.D. Thesis, University of Illinois (1978).

2. Proceedings of the Fifth International Conf. on Internal Friction and Ultrasonic Attenuation in Crystalline Solids edited by, D. Lenz and K. Lücke, Aug., 1973, Aachen, Germany.

3. Fundamental Aspects of Radiation Damage in Metals, edited by, M. T. Robinson and F. W. Young, Jr., October, 1975, Gattlinburg, Tennessee, USA.

4. Proceedings of the International Conference on the Properties of Atomic Defects in Metals, edited by, N. L. Peterson, R. W. Siegel, Oct., 1976, Argonne, Illinois, USA.

5. G. D. Magnuson, W. Palmer, and J. S. Kochler, Phys. Rev. 109, 1990 (1958).

6. J. W. Corbett, R. B. Smith, and R. M. Walker, Phys. Rev. 114, 1452 (1959); J. W. Corbett, R. B. Smith, and R. M. Walker, Phys. Rev. 114, 1460 (1959).

7. H. B. Huntington and F. Seitz, Phys. Rev. 61, 315 (1942).

8. J. B. Gibson, A. N. Goland, M. Milgram, and G. H. Vineyard, Phys. Rev. 120, 1229 (1960).

9. R. A. Johnson, Phys. Rev. 145, 423 (1966).

10. J. Holder, A. V. Granato, L. E. Rehn, Phys. Rev. B10, 363 (1974).

11. P. H. Dederichs, C. Lehmann, and A. Scholz, Phys. Rev. Lett. 31, 1130 (1973).

12. V. Spirić, L. E. Rehn, K.-H. Robrock, and W. Schilling, Phys. Rev. B15, 672 (1977).

13. H. G. Haubold, in: Proc. Conf. on Fundamental Aspects of Radiation Damage in Metals, Oct., 1975, Gattlinburg, Tennessee, USA.

14. P. H. Dederichs, C. Lehmann, H. R. Schober, A. Scholz, and R. Zeller, J. Nuc. Matr. 69 and 70, 176 (1978).

15. G. Vogl, W. Mansel, P. H. Dederichs, Phys. Rev. Lett. 36, 1497 (1976).

16. G. Vogl, W. Mansel, W. Petry, V. Gröger, Hyperfine Int. 4, 681 (1978).

17. M. L. Swanson and F. Maury, Can. J. Phys., 53, 1117 (1975).

18. H. Wollenberger, in: Proceedings of the International Conference on the Properties of Atomic Defects in Metals, Oct., 1976, Argonne, Illinois, USA.

19. L. E. Rehn, K-H Robrock, H. Jacques, J. Phys. F: Metal Phys. 8, 1835 (1978).

20. F. Dworschak, Th Monsau, H. Wollenberger, J. Phys. F: Metal Phys. 6, 2207 (1976).

21. C. L. Snead, Jr. and P. E. Shearin, Phys. Rev. 140, A1781 (1965).

22. K. R. Garr and A. Sosin, Phys. Rev. 137, A1250 (1965).

23. A. Sosin and L. H. Rachal, Phys. Rev. 130, 2238 (1963).

24. T. Ochs, J. Phys. E: Sci. Instrum. 1, 1122 (1968).

25. C. G. M. Kirby, Temperature: Its Measurement and Control in Science and Industry, Vol. 4, Pt. 2, Instrument Society of America, Pittsburgh (1972) p. 1511.

26. F. R. Fickett, Cryogenics 11, 349 (1971).

27. W. Schilling, Proc. of the International Conference on the Properties of Defects in Metals, Argonne, Illinois, 18-22, Oct., 1976.

28. J. A. Rayne, in Proceedings of the Fifth International Conference on Internal Friction and Ultrasonic Attenuation in Crystalline Solids, Aug., 1973, Aachen, Germany.

29. H. E. Bömmel, Phys. Rev. 96, 200 (1954).

30. W. P. Mason, Phys. Rev. 97, 555 (1955).

31. R. W. Morse, Phys. Rev. 97, 1716 (1955).

32. A. B. Pippard, Rep. Prog. Phys. 23, 176 (1960).

33. E. Lax, Phys. Rev., 115, 1591 (1959).

34. M. S. Steinberg, Phys. Rev. 111, 425 (1958).

35. R. Truell, C. Elbaum, B. Chick, Ultrasonic Methods in Solid State Physics, Academic Press, New York and London (1969).

36. A. S. Nowick and W. R. Heller, Adv. Phys. 12, 251 (1963).

37. N. H. March, in: Proceedings of the International Conference on the Properties of Atomic Defects in Metals, Oct., 1976, Argonne, Illinois, USA.

38. O. Takai, T. Fukusako, R. Yamamoto, M. Doyama, J. Phys. F: Metal Phys. 2, L80 (1972).

39. S. Ceresara, T. Federighi, and F. Pieragostini, Phys. Lett. 6, 152 (1963).

40. A. S. Nowick and B. S. Berry, Anelastic Relaxations in Crystalline Solids, Academic Press, New York and London (1972).

41. M. Gomez, S. P. Bowen, and J. A. Krumhansl, Phys. Rev. 153, 1009 (1967).

42. M. D. Kemple, Ph.D. Thesis, Physics Department, University of Illinois at Urbana-Champaign, 1971.

VITA

Kenneth Lowell Hultman was born on [redacted], [redacted]. He received his secondary education at Omaha Central High School, Omaha, Nebraska. He attended the California Institute of Technology and received a Bachelor of Science degree in physics with honors in June, 1970. He has been a graduate student at the University of Illinois since September, 1970, receiving a Master of Science degree in May, 1972.